FORMATION OF METALLIC GLASSES NEAR INTERMETALLICS IN ZR-CU AND ZR-CU-TI SYSTEMS

WANG YINXIAO

(B.Eng., BUAA)

A THESIS SUBMITTED

FOR THE DEGREE OF DOCTOR OF PHILOSOPHY

DEPARTMENT OF MATERIALS SCIENCE & ENGINERING

NATIONAL UNIVERSITY OF SINGAPORE

2012

DECLARATION

I hereby declare that the thesis is my original work and it has been written by me in its entirety. I have duly acknowledged all the sources of information which have been used in the thesis.

This thesis has also not been submitted for any degree in any university previously.

Wang Yinxiao

6 August, 2012

Acknowledgements

First of all, I would like to express my sincere thanks to my supervisor Professor Li Yi. I appreciate that he offered me the opportunity to further my study in NUS in 2008. Professor Li Yi is an excellent advisor, successful scientist and passionate person. I have received invaluable guidance and encouragement from him during my entire Ph.D. candidature. His patient teaching guides me to think logically, critically and professionally, and I have benefited tremendously from it. More importantly, his motivated and dedicated attitude in researching sets a real model for me. It is honored to work with him and I am sure that the experience will influence me continuously in my entire life. I would like to give my sincerest gratitude to him.

To both former and present group members in the Non-equilibrium Materials Lab: Dr. Zhang Jie, Dr. Wu Wenfei, Dr. Han Zheng, Dr. Grace Lim, Dr. Guo Qiang, Dr. Yang Hai, Dr. Pan Jie, Ms. Li Xiang, Mr. Wang Zhitao, Mr. Wang Dongjiang, Mr. Zuo Lianyong and Mr. Aaron Ong, I would like to express my very special and sincere thanks. Their help, support and encouragement are invaluable. It is wonderful to work with all these people.

I would like to thank all the Laboratory Technologists of the Department of Materials Science and Engineering: Mr. Chan Yew Weng, Mr. Chen Qun, Mr. Henche Kuan, Ms Agnes Lim and Mr. Roger Lee for the help in using the equipments. A special thank is given to Dr. Kong Huizi for her help in documentary work in the past four years. I would like to thank National University of Singapore for the financial support.

I also want to acknowledge my friends: Wang Hongyu, Fu Yabo, Zhang Jian, Sun Jian, Liu Zhengyi, Li Dan, Yang Yang, Yuan Du, Ran Min, Bao Nina, Sheng Yang, Yuan Jiaquan, Li Weimin, Sun Yajuan, Tang Xiaosheng, Ji Wei and Zhao Xin. It is wonderful to have you guys in my life.

Last but not least, I am deeply indebted to my family (my parents and my wife) for their great love and unconditional support. Without them, I would not have the faith to make it this far.

August 2012 in Singapore WANG Yinxiao

Table of Contents

Summary

Two typical methods have been used to form metallic glass since 1960s: liquid quenching and solid-state reaction. The glass formation range obtained by liquid quenching method is believed near eutectic points, especially deep eutectic points. Metallic glass is formed in the centre of phase diagram by solid-state reaction. However, the discovery of so called "intermetallic glass" provides a wider perspective of formation of metallic glass.

Intermetallic glass is a pair of optimum glass formers, which is formed near but separated by the intermetallic composition. This dissertation is to investigate the underlying mechanism of the formation of the intermetallic glass. Two alloy systems are selected: Zr-Cu binary system and Zr-Cu-Ti ternary system.

In Zr-Cu system, there are six intermetallic phases (i.e. Cu_9Zr_2, $Cu_{51}Zr_{14}$, Cu_8Zr_3, $Cu_{10}Zr_7$, CuZr and $CuZr_2$), and we have studied the glass formation near $Cu_{51}Zr_{14}$, Cu_8Zr_3, $Cu_{10}Zr_7$ and $CuZr_2$ intermetallics. A pair of intermetallic glass is located near $Cu_{51}Zr_{14}$, $Cu_{10}Zr_7$ and $CuZr_2$ intermetallics respectively. The phenomenon of formation of the intermetallic glass has been confirmed. Based on the assumption that intermetallic has Gibbs free energy in a sharp

profile, we proposed that two thermodynamically favored glass formation ranges are present under quenching. Kinetically, the temperature dependent viscosities of certain alloys were measured and the TTT curves of these alloys were constructed. It is surprisingly found that the intermetallic compound has a higher critical cooling rate than those of the optimum glass formers. Therefore, both the thermodynamic and kinetic perspectives contribute to the formation of intermetallic glass.

In the Zr-Cu-Ti ternary systems, based on the experimental results obtained in binary system, 5 at% Ti was added into compositions $Cu_{52.5}Zr_{47.5}$ to $Cu_{47}Zr_{53}$ to replace Zr to study the glass formation. It is demonstrated that the phenomenon of formation of intermetallic glass still can be observed in the resulting composition range ($Cu_{100-x}(ZrTi)_x$, where Ti=5% and x=47.5-53). The compositions of optimum intermetallic glass formers in ternary are as similar as those in binary system. Ti element is believed to stabilize the $Cu_{10}Zr_7$ phase during the precipitation.

However, in the composition range near Cu_2ZrTi intermetallic phase, the phenomenon of formation of intermetallic glass is not clear enough. Unlike the intermetallic in the previous study, Cu_2ZrTi intermetallic is not a line compound but has a wide homogeneity composition range. Furthermore, in this composition range, it is believed that the Gibbs free energy and liquidus

temperature varies slightly with the changing of composition. This may makes that the changing of critical thickness is insensitive to that of composition.

List of Tables

List of Figures

List of Publications

1. **Wang Y.X.**, Yang H., Lim G., Li Y., Glass formation enhanced by oxygen in binary Zr-Cu system, ***Scripta Materialia***, 2010,62:682-685
2. **Wang Y. X.**, Li Y., Formation of metallic glasses near intermetallics in Cu-Zr binary system (submission in progress)

Chapter 1

Introduction

1.1 Introduction to Bulk Metallic Glasses (BMGs)

1.1.1 The history of the development of BMGs

Metallic glasses (MGs) can be defined as metals or metal alloys without crystalline structure. They can be prepared by rapid solidification from liquid phase. The crystallization can be avoided when the cooling rate is high enough, so the atoms can be frozen in their liquid configuration when the solidification occurs. The first metallic glass, $Au_{75}Si_{25}$, was discovered in 1960

by Duwez by applying a so called 'gun technique' [1].

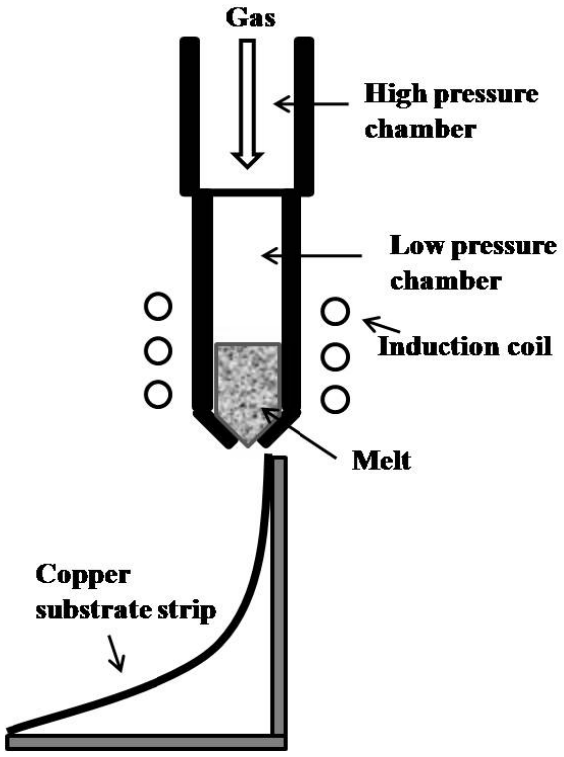

Figure 1.1 Schematic diagram of 'gun' technique of Duwez for rapid cooling (adapted from Ref. [2]).

The $Au_{75}Si_{25}$ alloy was melt and then ejected by high pressure gas on copper substrate strip to obtain a high cooling rate of 10^6K/s, as illustrated in **Figure 1.1** [2]. Since then, metallic glasses have attracted great attention and much research had been carried out to discover new metallic glasses in different alloy systems. However, the critical size of metallic glasses remained in micron-meter scale by the requirement of high cooling rate, which limited their commercial application.

In 1974, Chen discovered metallic glass in Pd-Cu-Si ternary alloy system with critical thickness larger than 1 mm by water quenching, which had an estimated cooling rate less than 10^3K/s [3]. If one arbitrarily defines 1 mm is the minimum thickness of the alloy as "bulk", then these Pd-Cu-Si ternary glasses should be the first bulk metallic glasses (BMGs) reported. After this, in 1984, another well-known $Pd_{40}Ni_{40}P_{20}$ ternary metallic glass was discovered by Kui and other co-workers using boron oxide fluxing method to purify the melt and eliminate heterogeneous nucleation [4]. The cooling rate of this boron oxide fluxing method was significantly lower, which was estimated as 10K/s level. In the late 1980s, Inoue and his collaborators discovered bulk metallic glasses without noble metals in La-Al-Ni ternary alloy system for the first time [5]. Since then, a new era of the research of bulk metallic glasses has begun. Building on this work, a family of glasses with rare earth elements was discovered, for example, in the La-Al-Cu, La-Al-Cu-Ni and La-Al-Cu-Ni-Co systems [6-8]. Subsequently, more and more bulk metallic glasses have been discovered in other multi-component systems such as Zr-, Mg-, Y-, Ca-, Au-, Fe-, Ni-, Co-, Ti- and Cu-based alloy systems [9-29].

Table 1.1 Summary of BMG compositions with their critical sizes

	Alloy system	Critical size (mm)	Year	Ref.
Zr-based	$Zr_{41.2}Ti_{13.8}Cu_{12.5}Ni_{10}Be_{22.5}$	25	1993	[17]
	$Zr_{65}Al_{17.5}Ni_{10}Cu_{17.5}$	16	1993	[18]
	$Zr_{55}Al_{10}Ni_{5}Cu_{30}$	30	1996	[30]
Ni-based	$Ni_{40}Cu_{5}Ti_{16.5}Zr_{28.5}Al_{10}$	5	2004	[31]
Pd-based	$Pd_{40}Cu_{30}Ni_{10}P_{20}$	72	1997	[32]
Cu-based	$Cu_{46}Zr_{42}Al_{7}Y_{5}$	10	2004	[33]
	$Cu_{44.25}Ag_{14.75}Zr_{36}Ti_{5}$	10	2006	[15]
Fe-based	$Fe_{48}Cr_{15}Mo_{14}Er_{2}C_{15}B_{6}$	12	2004	[34]
	$Fe_{41}Co_{7}Cr_{15}Mo_{14}C_{15}B_{6}Y_{2}$	16	2005	[16]
Mg-based	$Mg_{54}Cu_{26.5}Ag_{8.5}Gd_{11}$	25	2005	[35]
RE-based	$Nd_{70}Al_{10}Fe_{20}$	15	1997	[24]
	$Y_{36}Sc_{20}Al_{24}Co_{20}$	25	2003	[10]
Ca-based	$Ca_{60}Mg_{25}Ni_{15}$	13	2005	[11]
Au-based	$Au_{49}Ag_{5.5}Pd_{2.3}Cu_{26.9}Si_{16.3}$	5	2005	[12]
Al-based	$Al_{85.5}Ni_{9.5}La_{5}$	1	2009	[36]
	$Al_{86}Si_{0.5}Ni_{4.06}Co_{2.94}Y_{6}Sc_{0.5}$	1	2009	[37]

Table 1.1 summarizes some BMG compositions in different alloy systems with their critical sizes and their discovery years. Among all these BMGs, alloy $Zr_{41.2}Ti_{13.8}Cu_{12.5}Ni_{10}Be_{22.5}$ was the first commercial alloy, which was called Vitreloy 1(Vit 1) [17]. And $Pd_{40}Cu_{30}Ni_{10}P_{20}$ alloy still holds the record of the largest critical size, which reaches 72 mm [32].

Table 1.2 Relationship between properties of BMGs and the potential applications.

Properties	**Application field**
High strength	Engineering structural materials
High hardness	Cutting materials
High fracture toughness	Die materials
High impact fracture energy	Tool materials
High elastic energy	Sporting goods materials
High corrosion resistance	Corrosion resistance materials
Good soft magnetism	Soft magnetic materials
Self-sharpening	Penetrator

1.1.2 Properties and applications of BMGs

Unlike conventional metallic materials, metallic glasses have no long-range atomic order, which provides some unique and interesting properties, such as high strength, high elastic limit, high toughness, high corrosion resistance and

good soft magnetic properties. To date, BMGs have been used as hand phone casing, golf club head, scalpel, and also in many other areas [38, 39]. **Table 1.2** listed the relationship between the superior properties of BMGs and the possible variety applications. Furthermore, with the increasing number of BMGs and larger critical sizes of BMGs discovered, the future of BMGs is widely expanded both as potential engineering materials and as advanced research topics.

1.2 Formation of BMGs

Usually, metallic glasses are prepared by rapid quenching to avoid the nucleation and growth of crystalline phase, like shown in **Figure 1.2**. The melt should be quenched along line 2 to avoid "touching" the time-temperature-transformation (TTT) curve. Although a number of BMGs in various alloy systems have been discovered and even been commercially used in the past decades, understanding glass formation is still a basic but long-stand question, which is far from being solved. Generally, both thermodynamic and kinetic consideration are contributed to the glass formation; so it would be great help to predict glass forming ability (GFA) and glass forming range (GFR) by understanding how these two perspectives influence the glass formation.

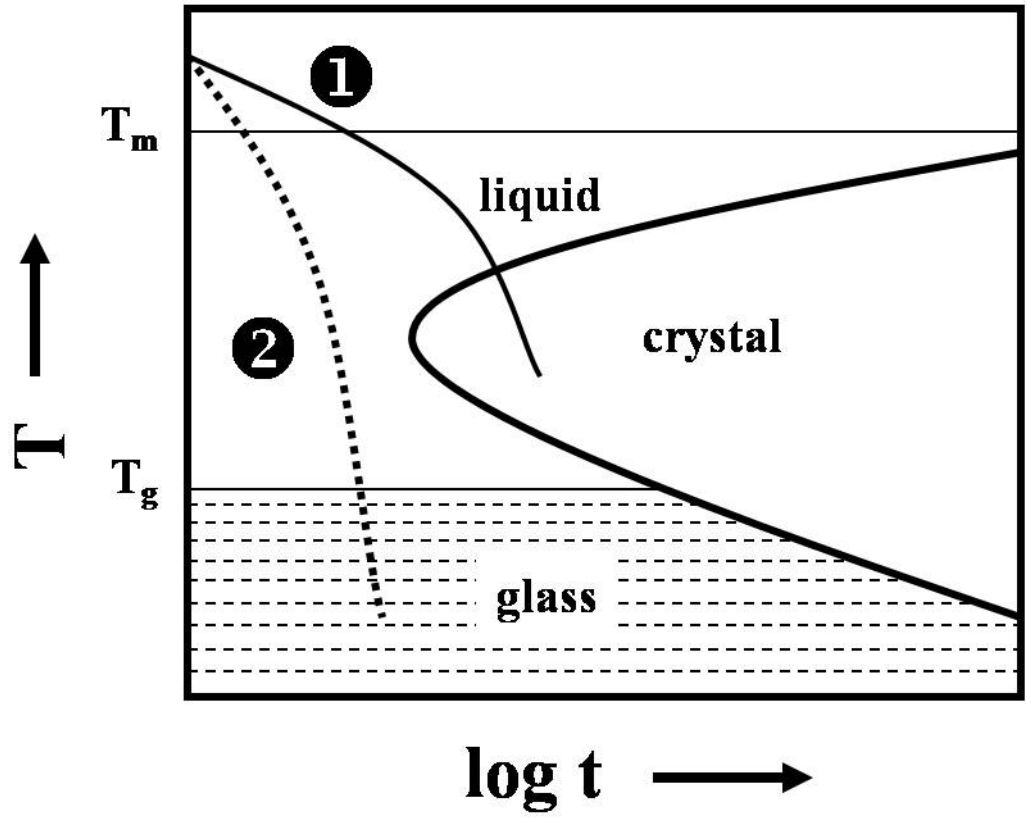

Figure 1.2 Schematic plot shows glass will be formed (as shown in dash line 2) from liquid by avoiding crystallization (as shown in solid line 1).

1.2.1 Thermodynamic consideration on glass formation

Basically, glass formation is a process of competition between crystallization and vitrification. It is commonly believed that a low driving force for crystallization lead to low nucleation rate, which results in a high GFA. The crystallization driving force or the Gibbs free energy difference between the liquid phase and the crystalline phase $\Delta G_{l\text{-}s}$ can be calculated as [40]:

$$\Delta G_{l\text{-}s}(T) = \Delta H_f - \Delta S_f T_0 - \int_T^{T_0} \Delta C_p^{l\text{-}s}(T) dT + \int_T^{T_0} \frac{\Delta C_p^{l\text{-}s}(T)}{T} dT \qquad (1.1)$$

where ΔH_f and ΔS_f are the enthalpy and entropy of fusion, respectively and T_0 is the temperature which Gibbs free energy of liquid phase and crystal phase equals to each other; ΔC_p is the specific heat capacity. A low $\Delta G_{l\text{-}s}$ can be obtained by low ΔH_f value, high ΔS_f value and low ΔC_p value. According to the "confusion theory" [41] and "three empirical rules" [9], the increasing alloy components leads to a higher ΔS_f value, which causes the increasing degree of dense random packing. That is favorable for the decreasing ΔH_f value [42].

Figure 1.3 shows the driving force for crystallization as a function of supercooling of some glass forming systems [40, 43, 44]. The temperature is normalized to the melting temperatures of the corresponding alloys. It shows clearly that the glass forming ability decreases with the increasing critical cooling rate changes from 1K/s for $Zr_{41.2}Ti_{13.8}Cu_{12.5}Ni_{10}Be_{22.5}$ alloy to 10^4K/s for $Zr_{62}Ni_{38}$ alloy, which is directly related to the increasing crystallization driving forces.

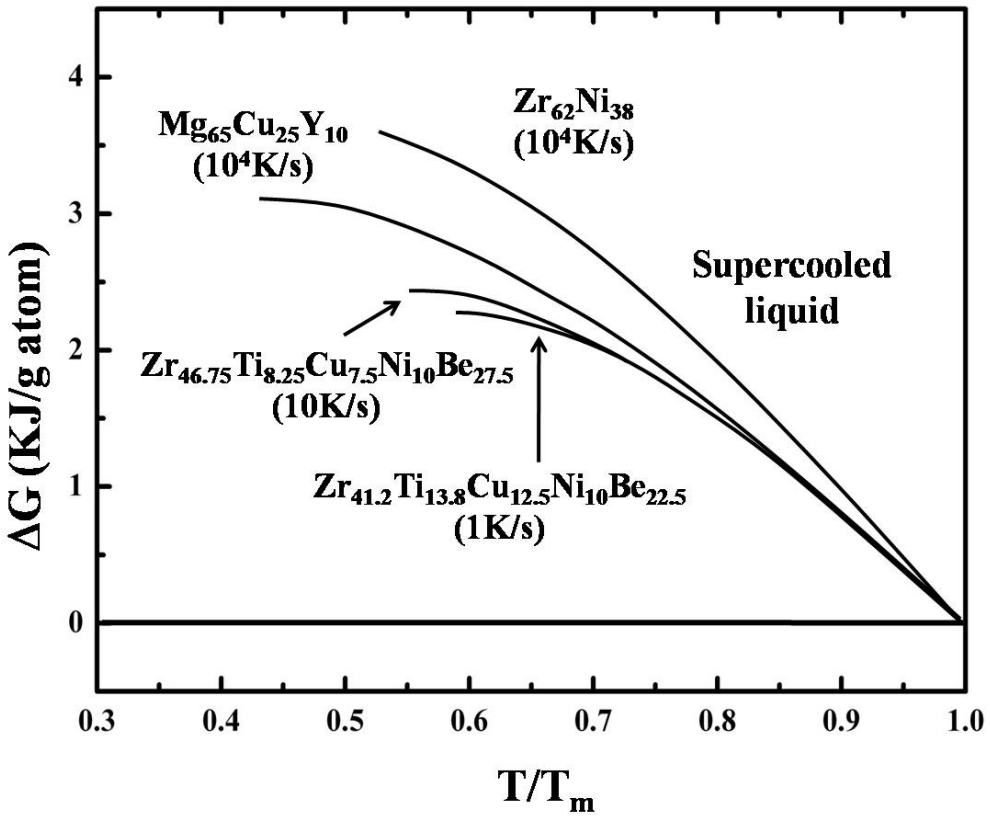

Figure 1.3 The crystallization driving forces and the corresponding critical cooling rate for selected glass forming alloys (reproduced from Ref. [43]).

1.2.2 Kinetics consideration on glass formation

Besides thermodynamic considerations, kinetic considerations about the undercooled liquid and the nucleation and growth of crystals also play important roles to glass formation of BMGs, which are determined by viscosity of undercooled liquid. A lot of effort has been done to measure the viscosity of a liquid from the temperature above the melting point down to the temperature near the glass transition temperature T_g [43, 45-49]. The viscosity can be expressed in the form of Vogel-Fulcher-Tamman (VFT)

equation:

$$\eta(T) = \eta_0 exp\left(\frac{D^* \cdot T_0}{T - T_0}\right) \quad (1.2)$$

where D^* is the fragility parameter, η_0 is a constant and T_0 is the VFT temperature, where the barrier to flow would go to infinity.

The value of D^* can be considered as the degree of how the system obey the Arrhenius law; the value of T_0 is related to T_g and changes with the value of D^* [50]. The bigger the value of D^* is, the stronger glass former the system should be. **Figure 1.4** compares the viscosities of some selected different glass formers, which include BMGs and non-metallic glass formers [51]. According to **Figure 1.4**, SiO_2 has a D^* value of about 100, and it is the strongest glass former; O-terphenyl is a fragile glass former with a D^* value of 5. The viscosities of BMGs lie between these two strongest and the most fragile glass formers, but are closer to strong glasses. A strong liquid can help glass formation in the undercooled liquid. Liquid with high viscosity can impede the formation of nuclei, which makes the nucleation and growth of crystal much more difficult and thus the glass formation would be easier [52, 53].

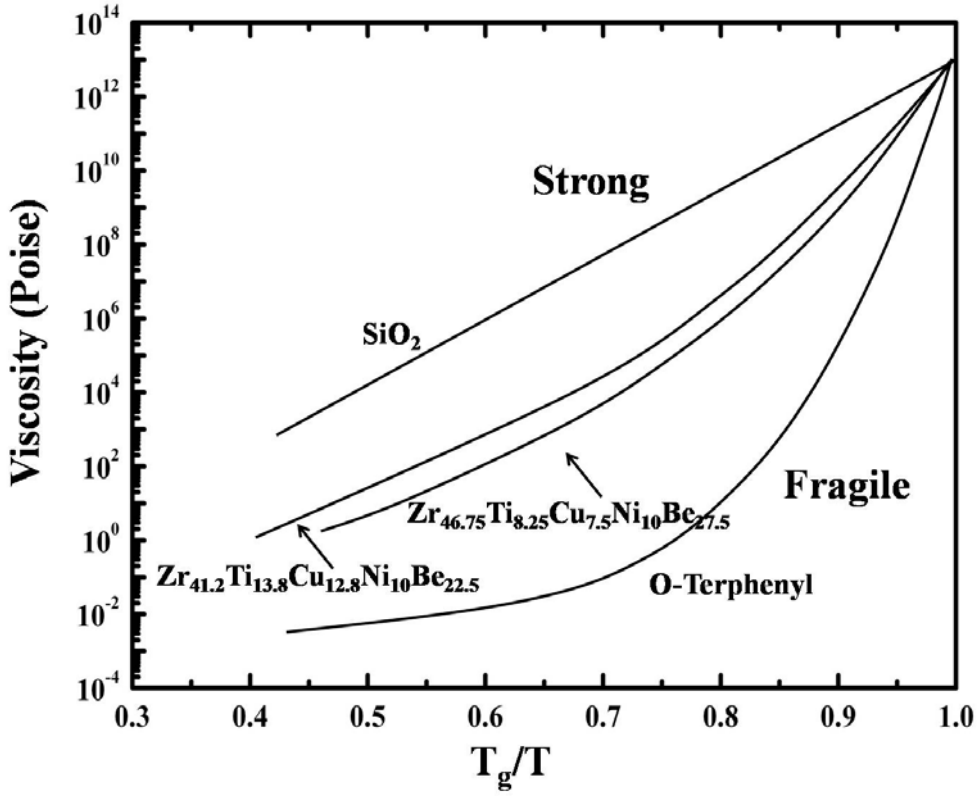

Figure 1.4 Angell plot comparing viscosities of some selected glass forming liquids (adapted from Ref. [51]).

1.3 Evaluation of glass forming ability

Scientific efforts have been made to look for a parameter or criterion to evaluate or predict glass forming ability of metallic glasses since the first metallic glasses in Au-Si system was discovered [1]. To date, several parameters or criteria have been provided to explain why some composition ranges, such as compositions near eutectic points, may be easier to form glasses.

1.3.1 T_{rg} criterion

Among all the criteria, the reduced glass transition temperature criterion is the most famous one, it was first proposed by Turnbull [54], which is based on classic nucleation theory. When a liquid is cooled down below to a certain temperature, the melt can solidification bypass the crystallization but into glass; then this temperature can be defined as glass transition temperature T_g. The reduced glass transition temperature or T_{rg} is the ratio of the glass transition temperature T_g and the melting temperature T_m. Turnbull suggested that when $T_{rg} \geq 2/3$, the homogeneous nucleation of the crystalline phase in the melt should be suppressed to a low level that glass can be formed (as shown in **Figure 1.5**). This criterion was further modified by Lu et al. in 2000 [55]. They suggested using the liquidus temperature T_l to replace the melting temperature.

This criterion implies that compositions near eutectic points may be good glass formers, especially near "deep" eutectic. It is understandable because the glass transition temperature does not change too much with the changing of composition; however, the liquidus temperature usually changes more steeply. Furthermore, in the case of "deep" eutectic, the liqudius temperature may change sharply with the composition, which makes the value of T_{rg} strongly depends on the composition. Thus the value of T_{rg} should reach the highest point at the eutectic point (as shown in **Figure 1.6**), therefore the

formation of glass is easier at the eutectic composition. Although Turnbull's theory explains eutectic glasses very well, it still fails in many systems which glass formers are observed at off-eutectic compositions [34, 56]. For example, in Zr-Cu binary alloy system, the best glass former $Cu_{64.5}Zr_{35.5}$ in the Cu_8Zr_3-$Cu_{10}Zr_7$ eutectic composition range did not correspond to the highest T_{rg} value [57].

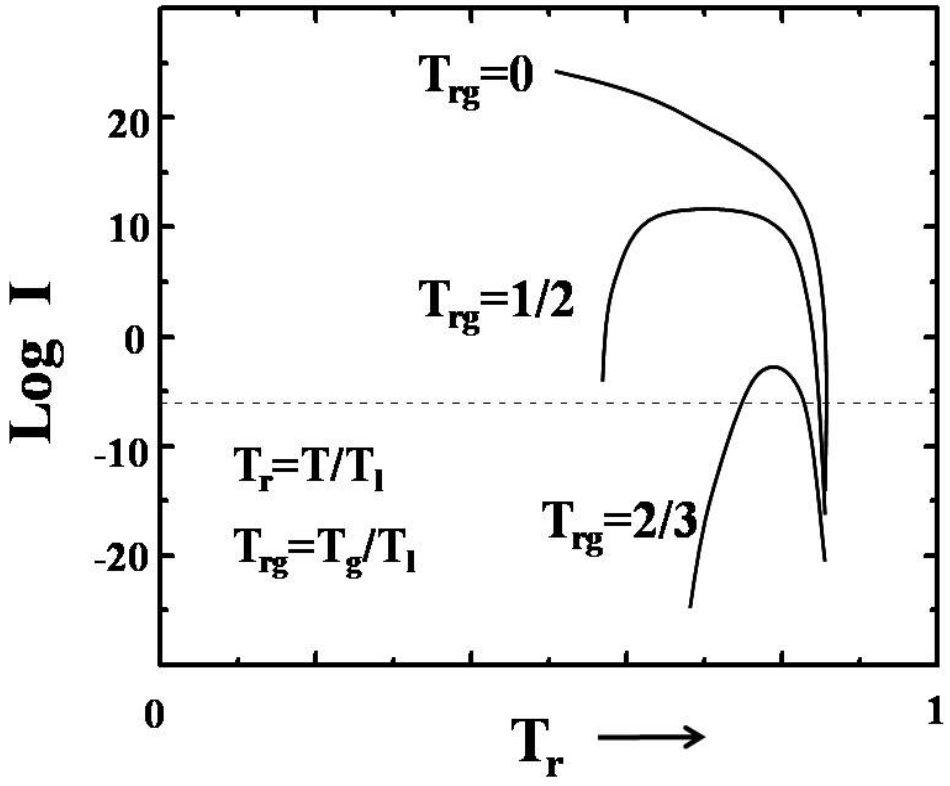

Figure 1.5 Relationship between homogeneous nucleation rate *I* and the reduced temperature T_r (adapted from Ref. [54]).

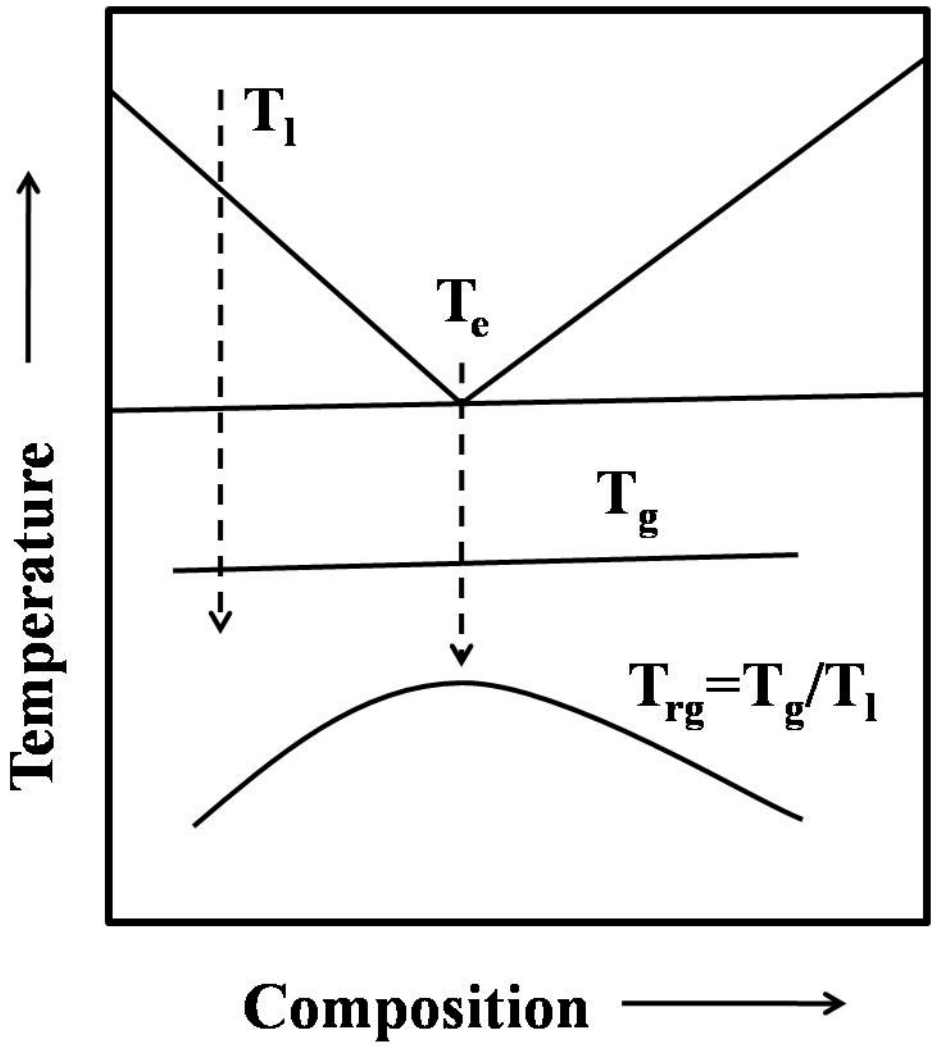

Figure 1.6 Schematic variation of the T_g, T_l and T_{rg} in a typical binary eutectic system, which indicates T_{rg} reaches the highest value at the eutectic composition.

1.3.2 Three empirical rules proposed by Inoue

Based on the significant work of the synthesis of BMGs in various alloy systems [5, 18, 30, 58-62], Inoue summarized three basic empirical rules which may make the system favored to glass formation [9, 63]:

(1) The system should be a multi-component system which contains at least

three components. The formation of metallic glasses should become easier with the increasing number of the components. It can be easily understood because multi-components can increase the degree of the random packing of the atoms in the system, which leads to the increasing entropy of fusion thus the decreasing Gibbs free energy. This criterion is also consistent with the "confuse principle" proposed by Greer [41].

(2) The atomic sizes of the components should be different. It is proposed that the atomic size difference should be at least 12%. This criterion is based on the structure and packing of atoms. The elements in the periodic table were divided into three groups by different atoms sizes [64]. By combination of atoms with significant differences in atom sizes could increase the density of random packing atoms, which increase the viscosity of the alloy liquid and makes the atomic diffusion sluggish in the undercooled liquid therefore the glass formation should be enhanced.

(3) The heat of mixing of the components should be negative. The negative mixing heat could help to stabilize of the undercooled liquid and form a homogeneous glass state. This criterion also contributes to glass formation as efficient of random packing of atoms.

1.4 Pinpoint strategy to locate the best glass forming range

All the criteria mentioned above are all about how to find an alloy system that can form glass. But none of them provide an effective way to find the best glass former or the best glass forming range in a given alloy system. Ma et al. proposed a practical strategy to locate the best glass former or the best glass forming range [65] in 2005 and then this strategy was widely used [56, 57, 66-68]. By applying the competitive-growth principle, this strategy treats the glass phase as a competing phase, thus the process of glass formation should be a competition between the formation of glass phase and the crystalline phase, which involves nucleation and growth. It was suggested that the glass phase could form even the heterogeneous nucleation occurs, as long as the temperature of the glass transition is higher than the temperatures of all the other crystalline phases, due to the phase with the highest growth temperature is kinetically favored. During the cooling, the growth of all the crystalline phases are suppressed as the glass transition temperature is higher than the temperatures of all the crystalline phases, and this can be observed by investigation of the microstructure of alloys with continuous changing compositions.

Figure 1.7 summarizes the changing of microstructure of two different

eutectic systems with the changing of cooling rate and composition. With the glass formation, the microstructure of alloys with continuous changing compositions would change from a composite structure (a primary phase label as α plus amorphous phase) to fully amorphous to another composite structure (another primary phase label as β plus amorphous phase). The difference is, in a regular eutectic system, the best glass forming range includes the eutectic composition; but in an irregular eutectic system, the best glass forming range would be away from the eutectic composition.

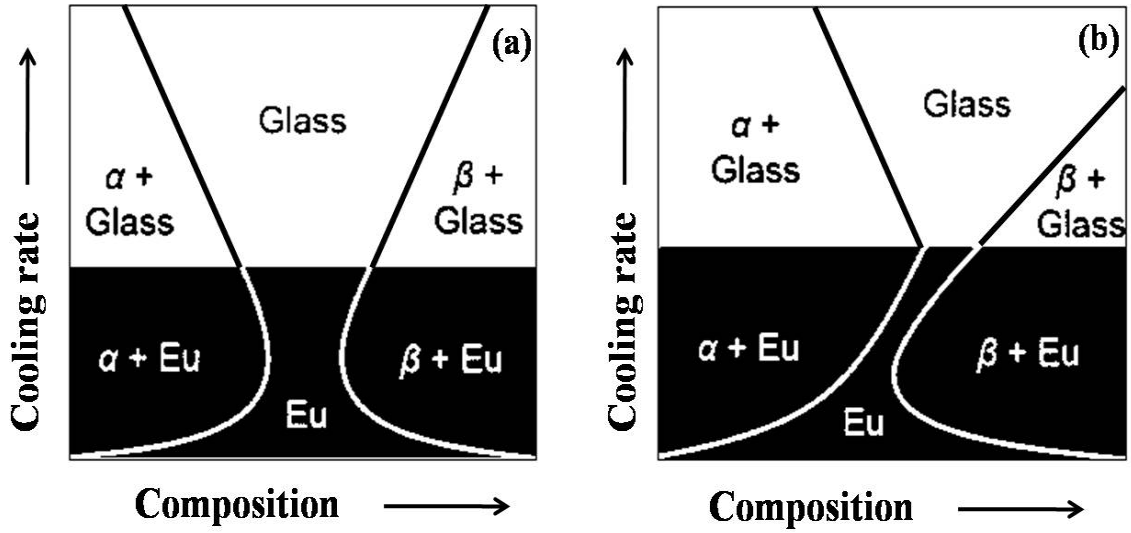

Figure 1.7 Phase-formation diagrams which show the glass and composite forming range of (a) a regular eutectic system and (b) an irregular eutectic system.

1.5 Glass formation in Zr-Cu and Zr-Cu-Ti alloy systems

Zr- based BMGs have been attracted much attention because their high glass forming ability and the superior mechanical properties such as high strength, high ductility and high elastic limit [69]. Until now, many BMG alloy systems have been developed in Zr- based alloys, for instance, Zr-Ti-Cu-Ni-Be [17], Zr-Al-Ni-Cu [18, 30, 70], Zr-Cu-Al [67, 71, 72]. In this section, a brief introduction will be given to the glass formation of Zr-Cu binary alloy system and Zr-Cu-Ti ternary alloy system.

1.5.1 Glass formation in Zr-Cu binary alloy system

Among all the metal-metal binary system, the Zr-Cu binary system has an outstanding glass forming ability. The studies about Zr-Cu system have been carried out for almost 30 years, including the calculation of phase diagram, glass formation, mechanical property [73-75], modeling and so on.

Zr-Cu system is an easy glass formation system; the glass formation range is wide and can be formed by different methods. In 1984, Atzmon et al. formed amorphous in Zr-Cu system by solid-state reaction [76], the amorphous had a composition of $Cu_{60}Zr_{40}$. In 2004, Wang et al. reported that $Cu_{64.5}Zr_{35.5}$ alloy can

be formed 2 mm amorphous rod by liquid quenching [57], which was the off-eutectic composition in Cu_8Zr_3-$Cu_{10}Zr_7$ eutectic range. At the meanwhile, Xu et al. also discovered a 2 mm metallic glass with a similar composition of $Cu_{64}Zr_{36}$ [77], this 0.5% atomic difference of composition can be contributed to the composition accuracy. Inoue reported that alloy $Cu_{45}Zr_{55}$, located near the eutectic point of $Cu_{10}Zr_7$-CuZr eutectic range, had a 1.5 mm glass forming ability [78]. Tang et al. reported $Cu_{50}Zr_{50}$ alloy also had a 2 mm glass forming ability [79], unusually, this composition is a line compound.

In 2008, by combining the sputter-deposited technique and micro-cantilever, Li et al. discovered three localized best glass formers by studying the density change of continuously changing compositions [80]. The critical sizes of these three compositions were: 1.14±0.04 mm for $Cu_{64}Zr_{36}$, 1.14±0.04 mm for $Cu_{50}Zr_{50}$ and 1.02±0.04 mm for $Cu_{56}Zr_{44}$, respectively. The first two compositions were consistent with that in Ref. [57, 77] and that Ref. [79]; and the difference in the critical size should be understandable due to the wedge-casting method used in Ref. [80] had a lower cooling rate. However, the third composition, $Cu_{56}Zr_{44}$ was the first time reported.

In 2009, a new family of metallic glass, so called “intermetallic glass”, was first reported by Wu and Li [81]. In their work, two optimized compositions, $Cu_{51.5}Zr_{48.5}$ and $Cu_{49}Zr_{51}$, with 2 mm glass forming ability were obtained

through liquid quenching, meanwhile, the 2 mm rod of alloy $Cu_{51}Zr_{49}$ showed fully crystalline structure. In another word, two glass forming ranges near but separated by the CuZr intermetallic compound have been demonstrated. This phenomenon was quite different from all the research results mentioned above: these two glass forming ranges cannot be contributed to the T_{rg} theory as the compositions were far from eutectic points and their corresponding eutectic glasses ($Cu_{56}Zr_{44}$ [80]and $Cu_{45}Zr_{55}$ [78]) but near intermetallic phase; in addition, unlike amorphous obtained through solid-state reaction, the glass forming ranges did not cover the whole center part of the phase diagram [82-85]. The different glass forming ranges by apply different theories and methods are summarized in **Figure 1.8**.

The formation of the intemetallic glass was interpreted by the hypothetic free energy curves of liquid and intermetallic phases. Generally, the free energy of the liquid (amorphous) phase varies gradually along with the composition, while that of the CuZr intermetallic phase varies sharply around the stoichiometric composition. Since the amorphous phase has a lower free energy in the vicinity of the CuZr intermetallic, it is favored thermodynamically to form glass if the kinetic constraint can suppress the solidification of the primary crystalline phases. It is believed that this work provides a new perspective to find new metallic glasses.

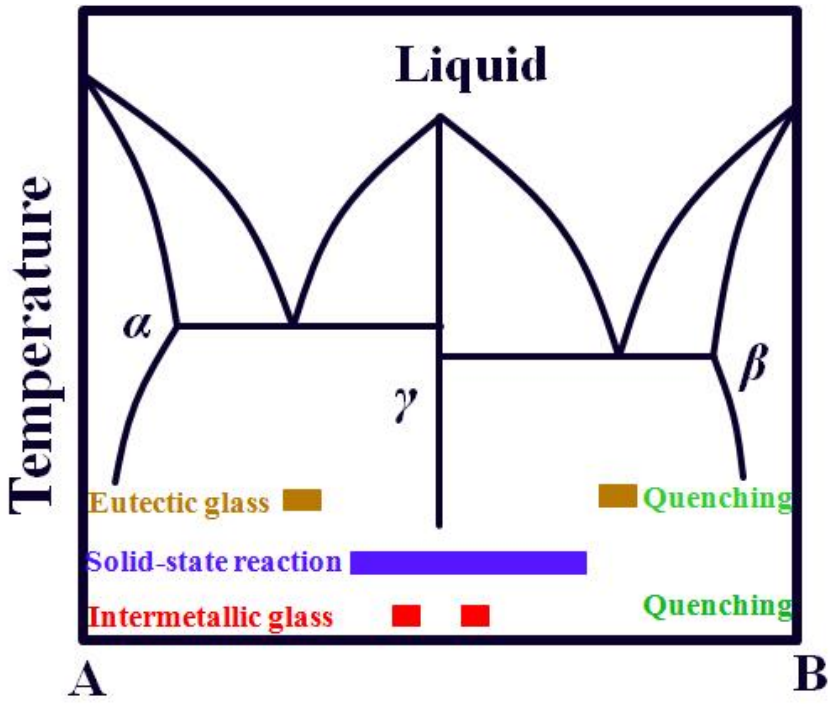

Figure 1.8 An schematic illustration of the glass forming ranges of the general metallic glass obtained by applying different theories and methods.

To summarize the glass forming ability in Zr-Cu binary system, **Table 1.3** lists the glass forming compositions with their corresponding critical sizes and the method used. It is clearly that Zr-Cu binary system is easy for glass formation through both liquid quenching and solid-state reaction. The glass forming range of Zr-Cu system is wide and also being studied carefully, which will be introduced in the following section.

Table 1.3 Summary of glass forming ability in Zr-Cu binary system.

Composition	Critical size (mm)	Method	Ref.
$Cu_{60}Zr_{40}$	<1	Solid-State reaction	[76]
$Cu_{64.5}Zr_{35.5}$	2	Copper mold casting (rod)	[57]
$Cu_{64}Zr_{36}$	2	Copper mold casting (rod)	[77]
$Cu_{45}Zr_{55}$	1.5	Copper mold casting (rod)	[78]
$Cu_{50}Zr_{50}$	2	Copper mold casting (rod)	[79]
$Cu_{50}Zr_{50}$	1.14±0.04		
$Cu_{56}Zr_{44}$	1.02±0.04	Wedge casting (wedge shape)	[80]
$Cu_{64}Zr_{36}$	1.14±0.04		
$Cu_{49}Zr_{51}$	2	Copper mold casting (rod)	[81]
$Cu_{51.5}Zr_{48.5}$			

Furthermore, there are also a plenty of work to calculate the phase diagram and the free energy curves of liquid, solid solution and intermetallic phases of Zr- Cu binary system, in order to predict glass forming range in this system [86-90]. **Figure 1.9** shows the calculated phase diagram of Zu- Cu binary system. In 1988, Saunders calculated the TTT curve of Zr- Cu system [91], and then the critical cooling rate was also calculated as 5×10^7 K/s. An assumption

was made that the glass can be formed when the value of critical cooling rate for a certain composition is less than 5×10^7 K/s. Due to the fact that the melt-spinning usually has a maximum cooling rate of ~1×10^7 K/s, the calculated glass forming range should be comparable to the experimental results by melt-spinning . The glass forming range was predicted as from ~25 to ~70 atomic percent of Zr. Actually, this prediction was in good agreement to the experimental results. Altounian indicated a glass forming range from composition $Cu_{70}Zr_{30}$ to $Cu_{25}Zr_{75}$ by studying the crystallization behavior of alloys in this range [92]. Kneller also reported a similar glass forming range from composition $Cu_{70}Zr_{30}$ to $Cu_{26}Zr_{74}$ [93]. A wider glass forming range was reported by Buschow, which covered from composition $Cu_{90}Zr_{10}$ to $Cu_{25}Zr_{75}$ [94, 95]. It was noticed that all these results were produced by melt-spinning method, so the glass forming range should be wider than the results listed in **Table 1.3**.

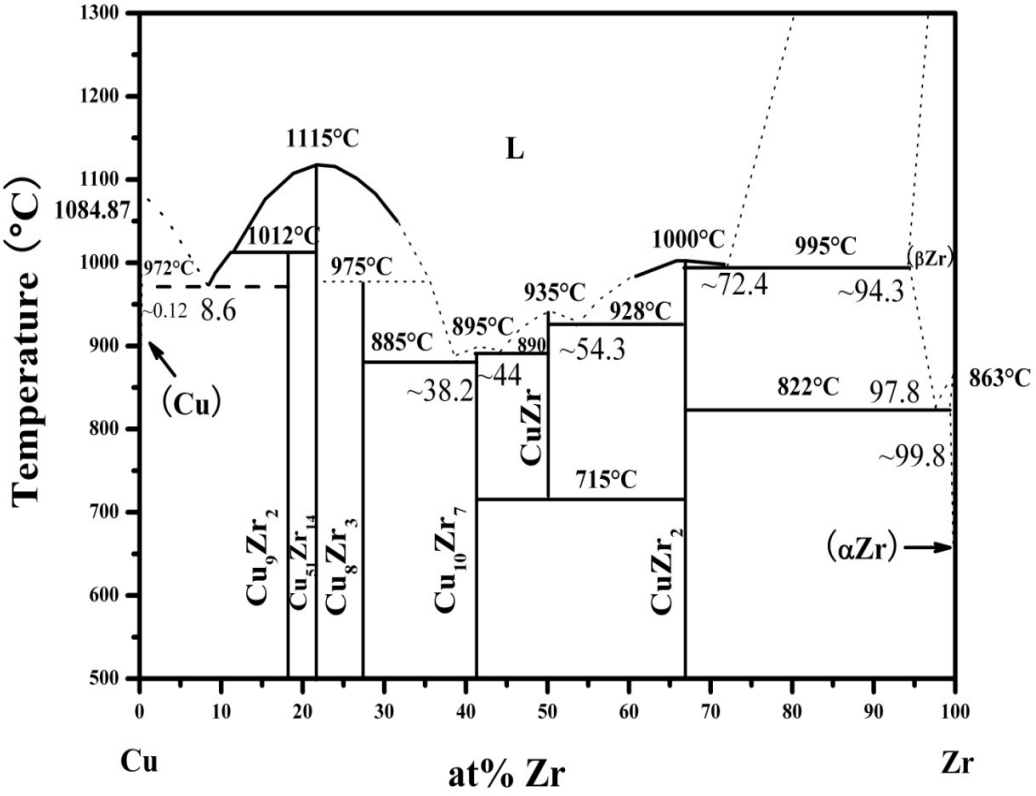

Figure 1.9 Calculated phase diagram of Zr-Cu binary system.

Li et al. calculated the driving force of the crystallization in Zr- Cu system [96]. By the consideration that glass formation is the competition between the crystalline phase and the amorphous phase during the solidification, the optimized glass formers should locate at the compositions with the localize minima crystallization driving forces. As shown in **Figure 1.10**, there were four compositions had the localize minima crystallization driving forces; they all showed agreement in the reported glass formers listed above except composition with 0.068 mole fraction of Zr. This may be caused by the lack of consideration of kinetic point of view.

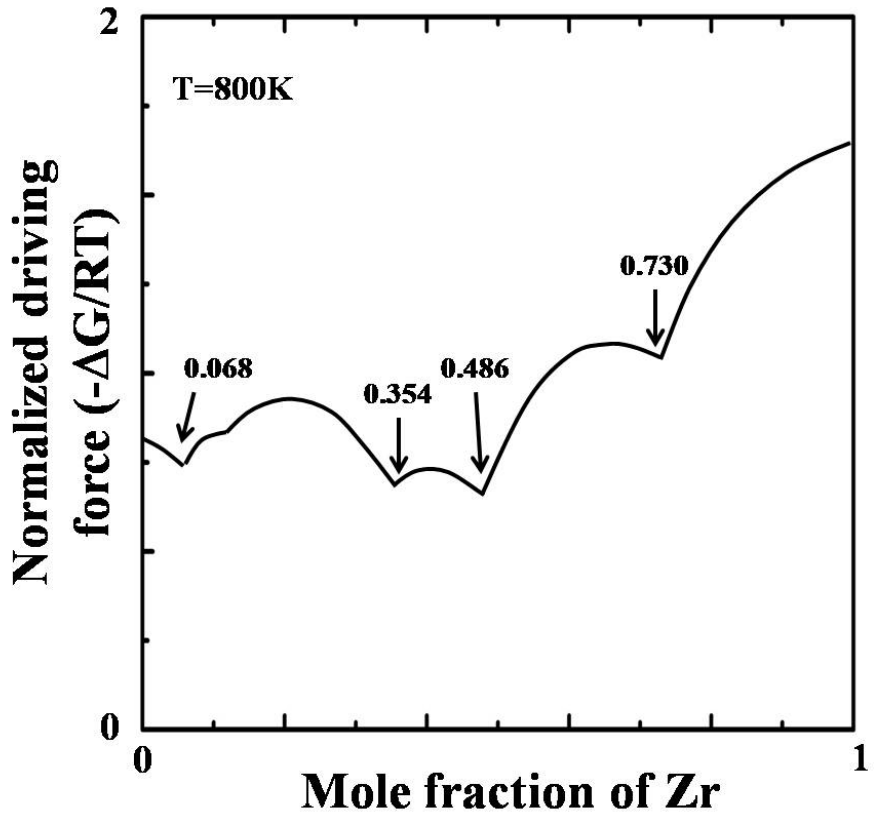

Figure 1.10 The calculated surface of the crystallization driving force for Zr- Cu system at 800K as well as the optimum glass formers (adapted from Ref. [96]).

In a word, the Zr-Cu system can form metallic glasses by both liquid quenching and solid-state reaction. It was reported that Zr-Cu showed a large negative heat of mixing [64], which may further help the glass formation [9]. Glass forming ranges are wide, which covers eutectic, off-eutectic and intermetallic compositions.

1.5.2 Glass formation in Zr-Cu-Ti tenary alloy system

According to Inoue [9, 64], the Zr-Cu-Ti ternary alloy system can be classified into glass forming group with elements from ETM and LTM, which represents early transition metal (elements belong to group IIIA-VIIA in the periodic table) and late transition metal (elements belong to group VIIIA-IIB in the periodic table) respectively. The glass forming ability of this ternary will be briefly introduced in the following.

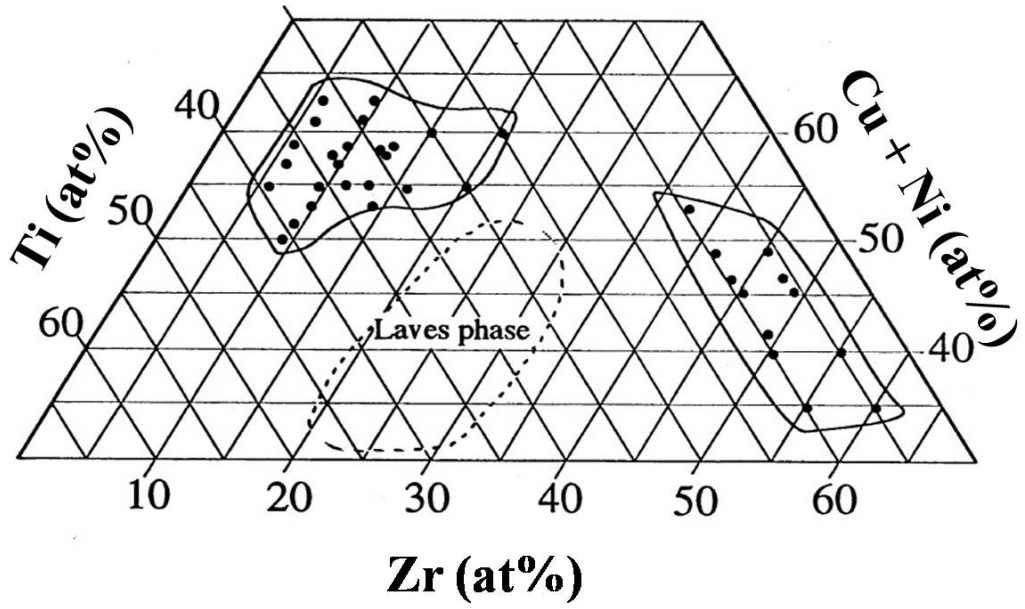

Figure 1.11 Pseudo-ternary phase diagram of Ti-Zr-Cu-Ni system with two glass forming ranges (adapted from Ref. [97]).

In 1988, Massalski et al. reported a wide glass forming range in Zr-Cu-Ti system through melt-spinning method [98]. The resulting ribbons had a thickness about 50 μm. The widest range reported was across the whole region of the phase diagram at about 50 atomic percent of Cu. In 1995, Lin et

al. discovered $Ti_{35}Zr_{10}Cu_{55}$ metallic glass with critical thickness of 500 μm; the critical cooling rate was estimated at a level of 2×10^4K/s [97]. Meanwhile, a pseudo-ternary alloy system Ti-Zr-Cu-Ni was also reported. Two glass forming ranges, both Ti- rich region and Zr- rich region, were located with a maximum 4mm glass forming ability (as shown in **Figure 1.11)** [97]**.**

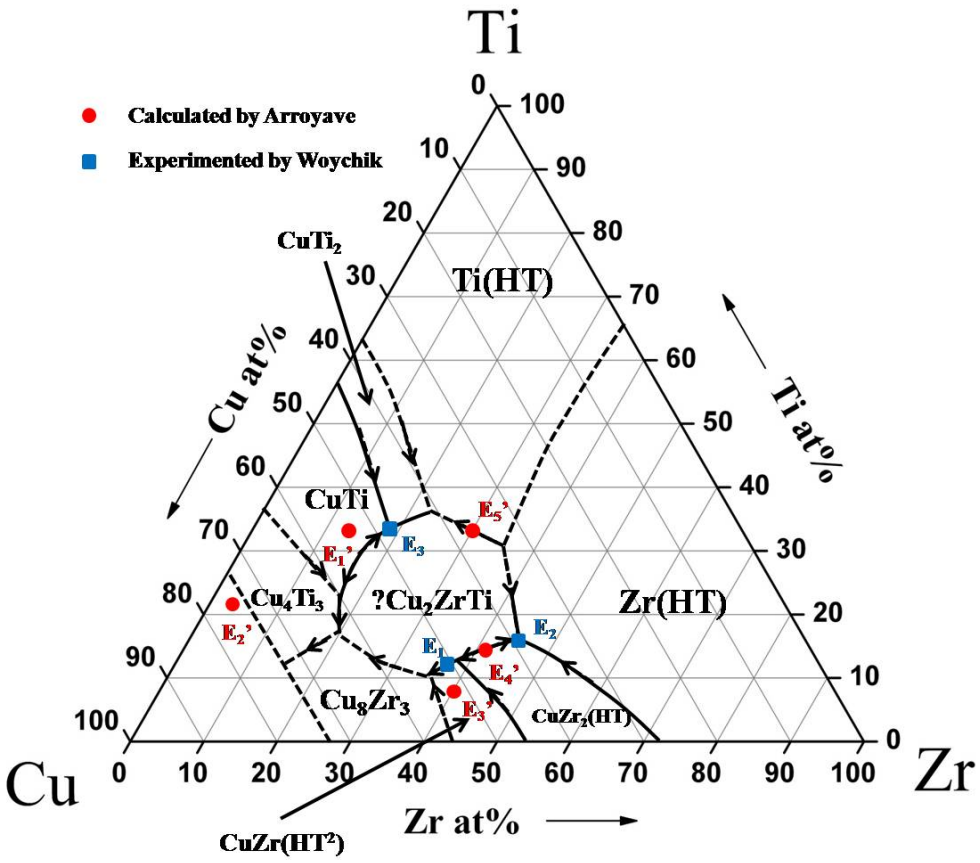

Figure 1.12 The liquid projection of the ternary phase diagram of Cu-Zr-Ti system. Three eutectic points marked as blue square were given by Woychik [99]; and five eutectic points marked as red circles were given by Arroyave [100] (adapted from Ref. [51]).

Later, Inoue et al. studied the glass formation of compositions $Cu_{60}Zr_{40-x}Ti_x$, where x=0-40 at% [101, 102]. $Cu_{60}Zr_{30}Ti_{10}$ was the best glass former with 4mm

glass forming ability. More recently, a series of metallic glasses were reported around the eutectic point E_3' with the composition of $Cu_{52}Zr_{40}Ti_8$ (as shown in **Figure 1.12**) with also have 4mm glass forming ability [103]. There were five compositions in this new glass forming range can form 4mm glass: $Cu_{52}Zr_{42}Ti_6$, $Cu_{51}Zr_{42}Ti_7$, $Cu_{51}Zr_{41}Ti_8$, $Cu_{52}Zr_{40}Ti_8$ and $Cu_{51}Zr_{40}Ti_9$. **Figure 1.13** summarizes the independent glass forming ranges from different references.

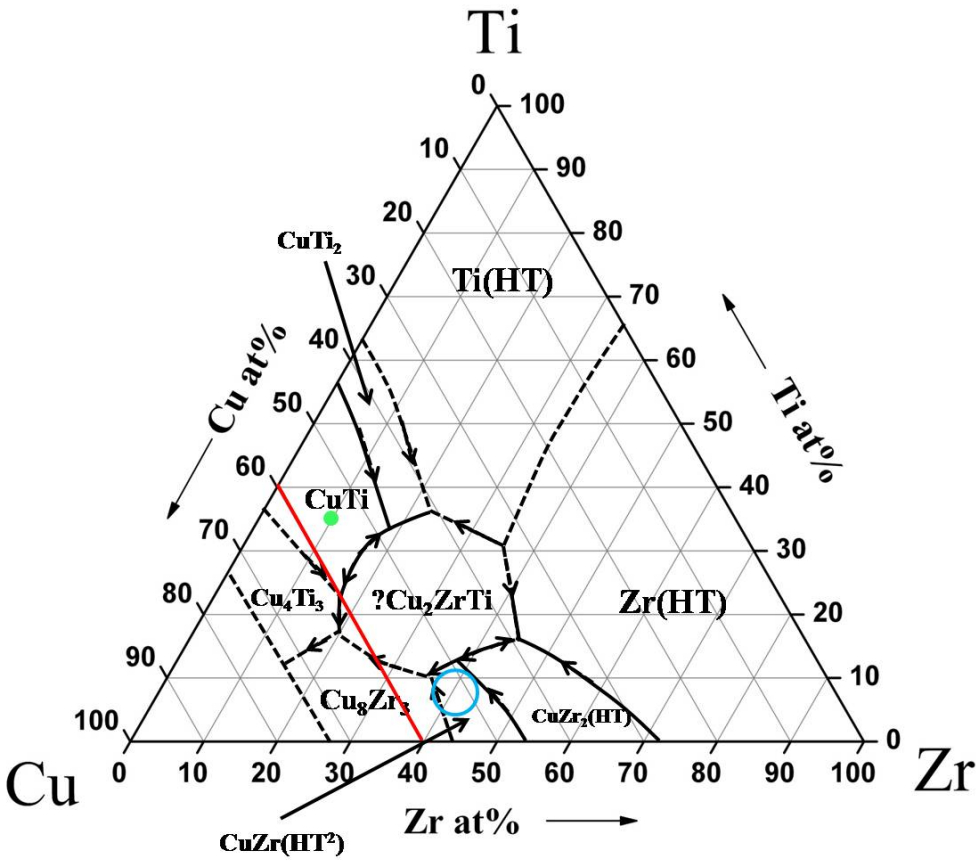

Figure 1.13 Summary of different glass forming ranges in Zr-Cu-Ti system. The red line, blue circle and the green dot represent glass formers from different references [97, 101-103].

1.6 Motivation and outline of this thesis

The underlying of the formation of intermetallic glass is still an unsolved question. The purpose of this thesis is to further investigate the mechanism of formation of intermetallic glass from both thermodynamic and kinetic points of view. Two alloy systems (Zr-Cu binary system and Zr-Cu-Ti ternary system) are selected to systematically study the glass forming ability first and then an interpretation is provided. There are five chapters in this thesis.

In Chapter 1 (this chapter), the development and general knowledge of BMGs was introduced. The glass formation of Zr-Cu and Zr-Cu-Ti systems was reviewed, followed by the motivation and the outline of this study.

In Chapter 2, schematic pictures of all equipments used in this thesis are provided. Furthermore, the experimental procedures and details are also provided.

In Chapter 3, the glass formation near intermetallic phases of Zr-Cu system is carefully studied. The underlying mechanism is provided in both thermodynamic and kinetic perspectives by studying the crystallization driving force, the viscosity of the liquid and the TTT curves of the selected compositions.

In Chapter 4, the glass formation of two different composition zones in Zr-Cu-Ti ternary system is studied. And the glass forming range of Zr-Cu-Ti system was calculated by Miedema method.

Finally, the results of this thesis are summarized and topics for future research were suggested in Chapter 5.

Chapter 2 Experimental procedures

2.1 Preparation of master alloys

The ingots of master alloy were prepared by arc melting a mixture of Zr with a purity of 99.98%, Cu with a purity of 99.9998% and Ti with a purity of 99.99%. The melting process was carried out under a high purity argon atmosphere in the Edmund Buhler LSG-400 arc melting system. Every ingot was re-melted at least six times to obtain chemical homogeneity. The weight loss during the melting was controlled within 0.3% to maintain the composition accuracy. The ingots were cut into pieces to cast into different

shape.

2.2 Casting procedures

Different casting methods were used depending on the thickness or the shape required.

2.2.1 Melt-spinning

The melt-spinning method was used to produce ribbons; the cooling rate of melt-spinning can reach 10^6K/s. The melt-spinning was carried out in the Edmund Buhler D-7400 single roller system, the diameter of the copper wheel is 20cm. The alloy was get from the master alloy and then placed into a quartz tube with a nozzle of ~0.4 mm in diameter. The quartz tube was placed into the center of the induction coil. The chamber was vacuumed first followed by backfilling argon gas to a certain pressure. The alloy was melted by the inducted current, and then the valve located at the top of the quartz tube was opened to let the high purity argon (with a higher pressure than the pressure in the chamber) gas in. The melt was ejected out by the input high pressure argon gas from the nozzle to cool down on the surface of a fast rolling copper wheel into a ribbon shape. **Figure 2.1** is a schematic diagram of the melt-spinning equipment and the procedure. The thickness of the ribbon can

be modified by changing the rolling speed of the copper wheel: the faster the rolling speed was, the thinner the ribbon would be. In this thesis, the rolling speed of the copper wheel changes from 35m/s to 45m/s.

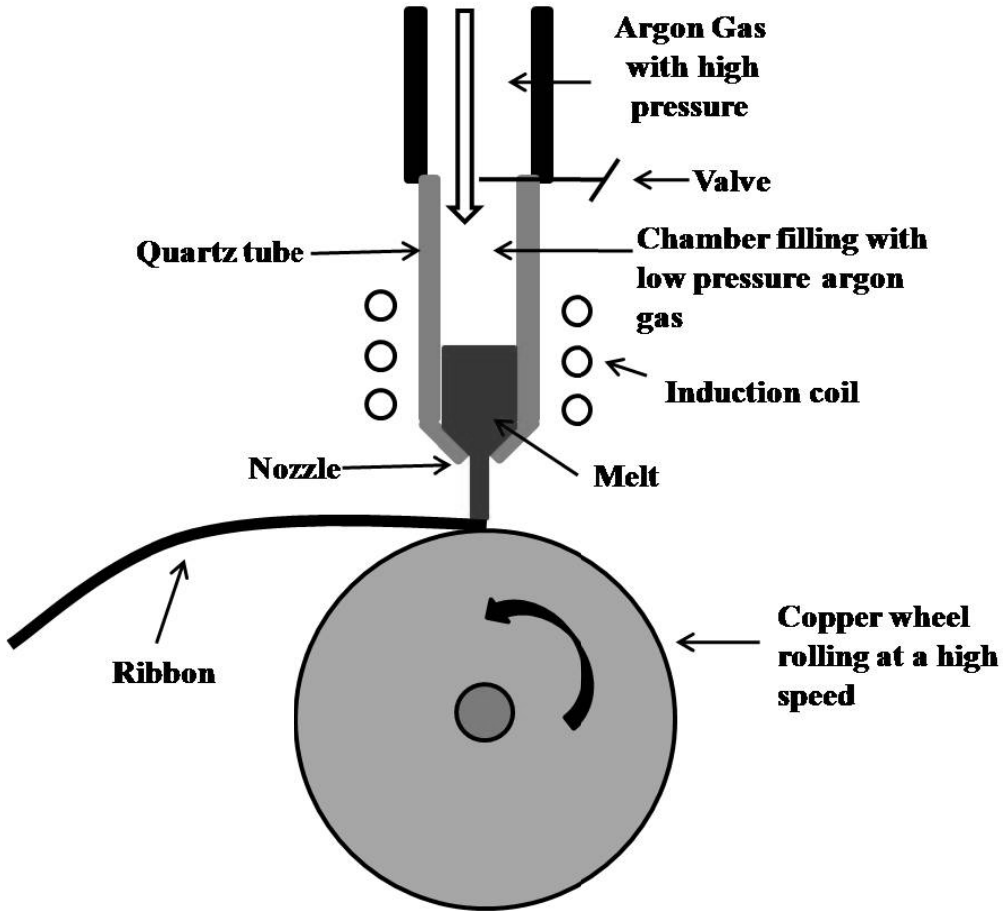

Figure 2.1 A schematic diagram of the melt-spinning equipment.

2.2.2 Wedge casting method

The wedge casting method was widely used to study the critical thicknesses of the metallic glasses. The accurate critical size can be easily determined due to the wedge shape with gradually changed thickness. The experimental condition of wedge casting method was as similar as the melt-spinning

method, except the melt was injected into copper mold with wedge shape instead of being ejected on the surface of a fast rolling copper wheel. **Figure 2.2** is a schematic diagram of the wedge casting method.

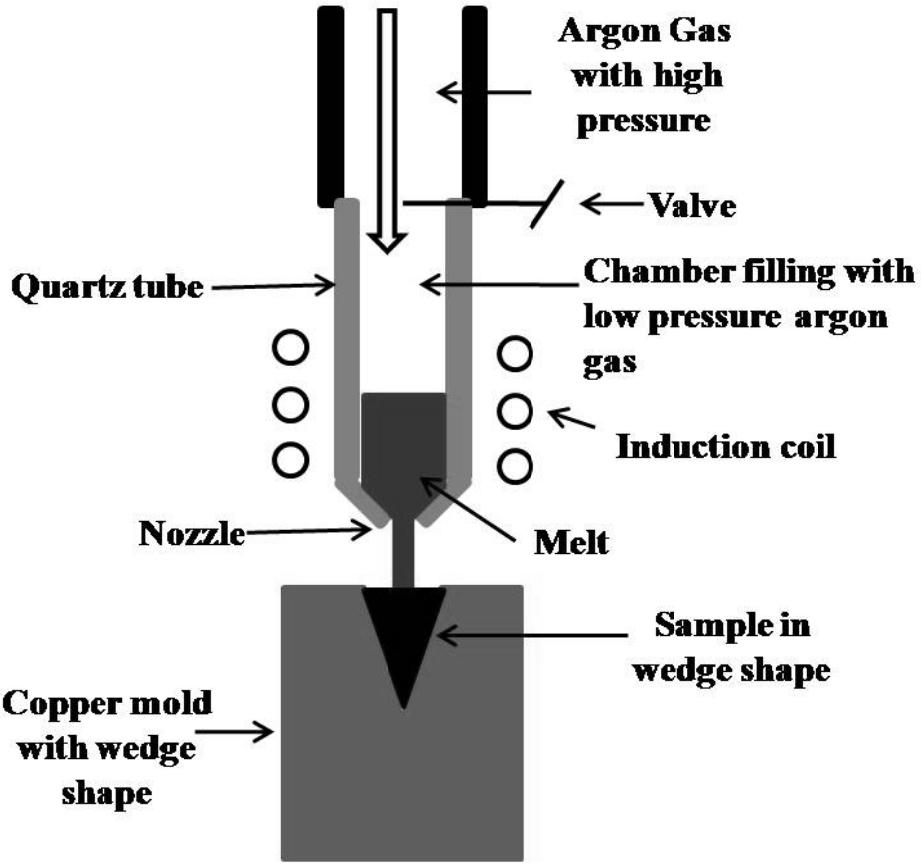

Figure 2.2 A schematic diagram of the wedge casting method.

2.2.3 Suction casting method

The suction casting method was used to produce rods with diameter of 3 mm or less. The equipment was modified from the Edmund Buhler D-7400 MAM-1 mini arc melting system: a cylindrical copper mold connecting to a

container replaced the original copper crucible. The container was used to introduce a pressure difference between the chamber and the container so the melt can be sucked into the copper mold during the casting.

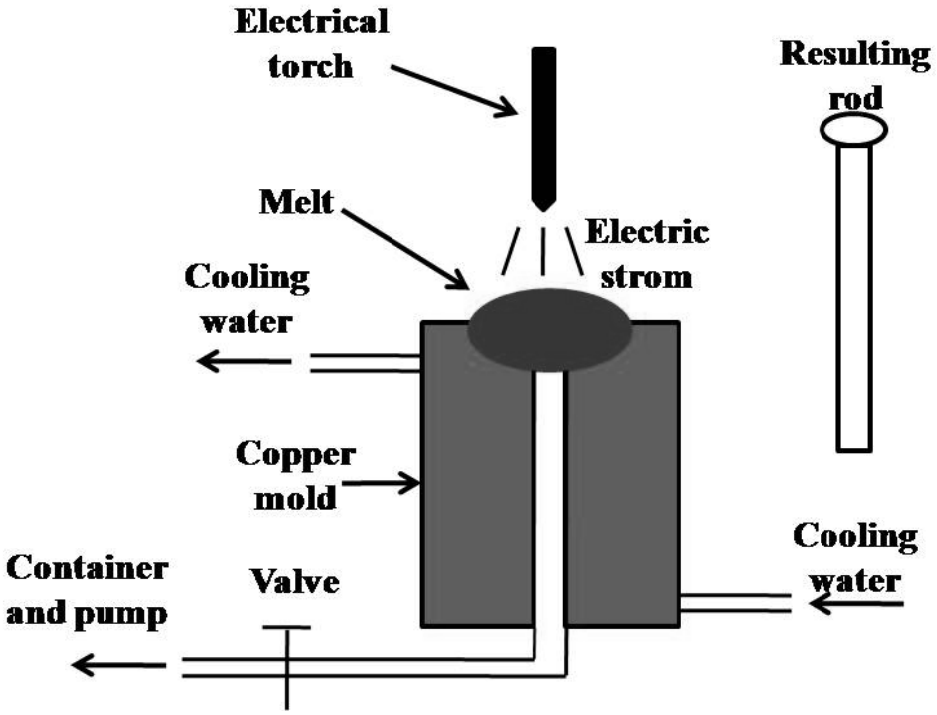

Figure 2.3 A schematic diagram of the suction casting equipment.

Figure 2.3 is a schematic diagram of this suction casting equipment. The container was pre-vacuumed to a certain pressure followed by the closing of the valve. After this, the chamber was backfilled with argon gas (to a higher pressure than that of container). The alloy was melt on the top of the copper mold and then the valve was opened so the pressure difference between the container and the chamber can suck the melt into the copper mold immediately. The diameter of the rod was 3 mm; the length of the rod was 30

mm, as long as the copper mold.

2.2.4 Copper mold casting

Copper mold casting was used to cast rods with diameter larger than 3 mm in this thesis. The casting procedure was carried out in the chamber of the Edmund Buhler LSG-400 arc melting system, the same system as the preparation of the master alloys. The master alloy was re-melted for several times to get the chemical homogeneity; and then the melt would be poured into the copper mold before the solidification occurred by rotating the copper crucible, with the electric storm on. Rods with different diameters were obtained by using different molds. **Figure 2.4** is an interior photo of the arc melting system with copper mold in it.

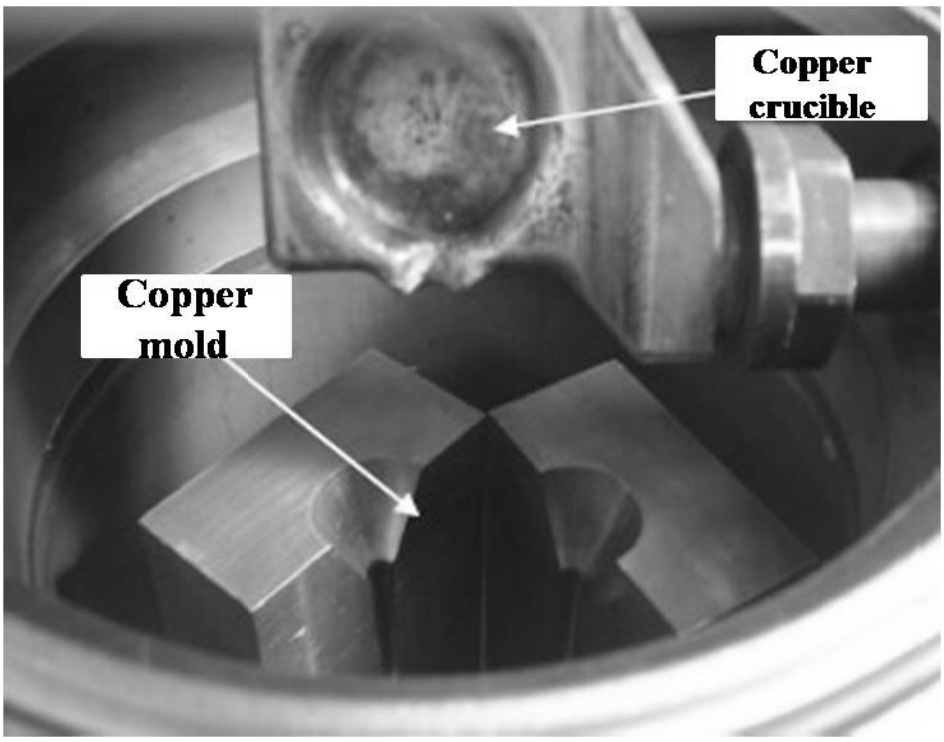

Figure 2.4 A photo of the LSG-400 arc melting system with copper mold in it.

2.3 Microstructure characterization

X-ray diffraction (XRD), optical microscopy (OM) and scanning election microscopy (SEM) were the general methods to characterize the samples.

2.3.1 X-ray diffraction (XRD)

The X-ray diffraction (XRD) was used to identify the amorphous phase or the crystalline phases if existed. The scanning was carried out in the Bruker D8 Advanced XRD machine with Cu-Kα radiation (λ = 1.5402 Å). The current and the voltage were set as 40 mA and 40 kV, respectively. The step size is 0.005° and the time step is 0.25s. For the ribbon samples, the ribbons were fixed on a glass plate with double-side tape with the chill-side faced up. For the rod samples, they were mounted and then were polished to the central part of the rod longitudinally (the detail of the mounting and polishing would be mentioned in the next section).

2.3.2 Optical microscopy (OM) and scanning election microscopy (SEM)

The samples for OM and SEM were mounted into resin first, and then they were carefully grinded with 80 to 1200 grit silicon carbide papers to the

central part of the rods or wedge samples longitudinally. Finally they were polished by 1 μm powder Al suspension. The samples were etched by a solution mixed by 65% HNO_3 and 50%HF at ratio 9:1. The etching time would be different for different alloy systems: for Zr-Cu system, it should be about 3 seconds and the time was about 60 seconds for the Zr-Cu-Ti system.

Optical microscopy was carried out by using an Olympus PME 3 optical microscope. The critical sizes of wedge sample were measure under OM by using a lens with ruler. The critical size of wedge sample was defined as the width of the wedge at the boundary between the crystalline phase and the amorphous phase, as shown in **Figure 2.5**. Scanning election microscopy (SEM) was carried out by using Philips XL30 FEG SEM.

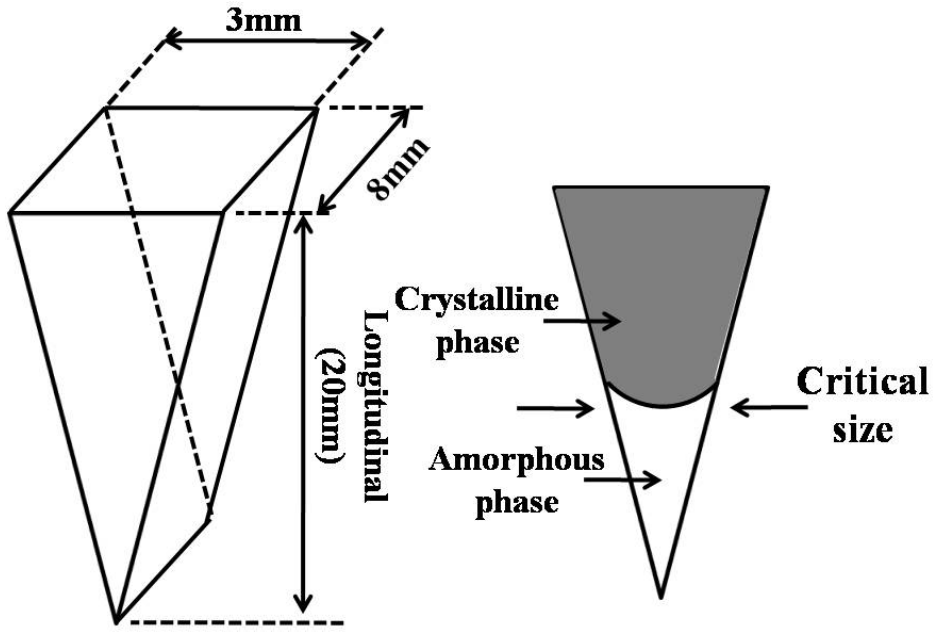

Figure 2.5 A schematic diagram of the measurement of critical size of wedge sample.

2.4 Thermal analysis

The differential scanning calorimetry (DSC) was carried out by using TA instruments DSC 2920 machine. The DSC was calibrated by pure In and Zn first, and then the samples were heated with different heating rates in argon atmosphere. The glass transition temperature T_g, the onset crystallization temperature T_x and the enthalpy of crystallization, which is the area covered by the crystallization peak, can be obtained by analyzing the resulting DSC curves. The Universal Analysis program is used to do the analyzing.

The measurements of the melting temperature T_m and the liquidus temperature T_l were carried out in the Netzsch 404 Pegasus DSC machine. The heating rate was set as 0.17 K/s. The resulting traces were analyzed by the Proteus Analysis program.

Chapter 3

The formation of intermetallic glasses in Zr–Cu system

3.1 Introduction

Basically, there are two common methods to form metallic glasses, one is thought liquid quenching and the other one is solid-state reaction. (1) Liquid quenching: Turnbull's earlier paper indicated that a larger reduced glass transition temperature T_{rg} value (T_{rg}=T_g/T_l, where T_g and T_l are the glass transition temperature and liquidus temperature, respectively) may lead to a smaller nucleation rate and subsequently a better glass-forming ability [54]. This makes bulk metallic glasses (BMGs) through liquid quenching

commonly to be formed near the eutectic compositions, specifically deep-eutectic compositions [51, 91, 104, 105]. (2) Solid-state reaction method: film or powders of MGs can be formed through isothermal inter-diffusion or mechanical milling below glass transition temperature, respectively [82-84, 106-108]. Usually, the alloy system, which can form metallic glasses through this method, has a large negative heat of mixing. Unlike the glass forming ranges through liquid quenching, the glass forming ranges obtained by solid-state reaction can cover the whole central part of the phase diagrams, including the intermetallic compounds.

However, the recent discovery so called "interemtellic glass" by Wu and Li provided a new perspective for searching new metallic glasses [81]. In their work, a pair of bulk metallic glasses ($Cu_{51.5}Zr_{48.5}$ and $Cu_{49}Zr_{51}$) with 2 mm critical size was obtained by liquid quenching in the Zr-Cu binary alloy system, next to the intermetallic formed fully crystalline phase. This phenomenon is quite different from that of all the BMGs obtained through liquid quenching as the glass formation ranges are around intermetallic phase instead of eutectic point. Also, it is also distinguished from the glass obtained from solid-reaction method as the glass formation range did not cover the whole central part of the phase diagram.

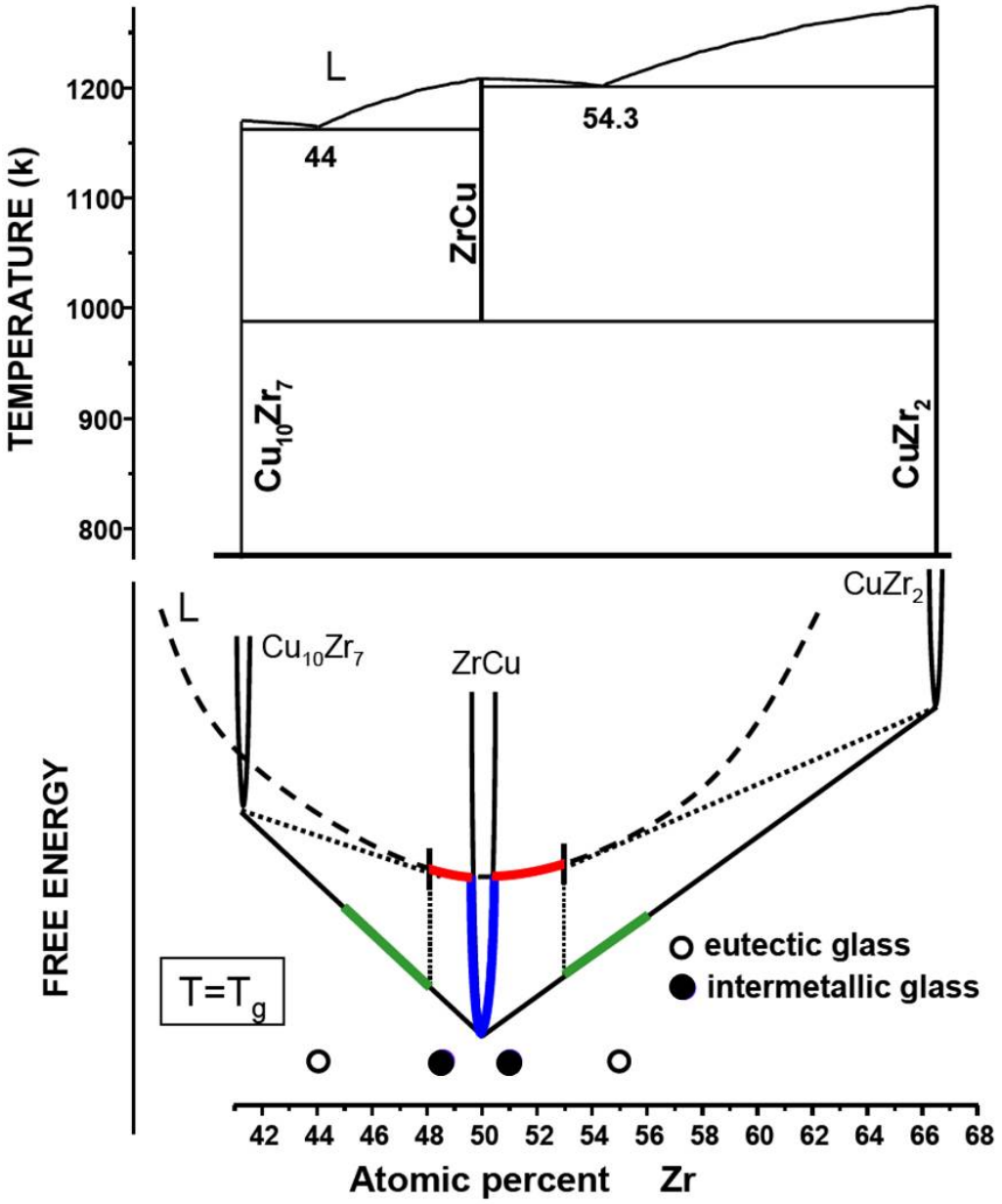

Figure 3.1 Part of Zr-Cu phase diagram and the corresponding hypothetical free energy curves. The red lines represent glass forming regions and two solid circles are two intermetallic glass formers. The eutectic glasses are marked as open circles (adapted from Ref. [81]).

An explanation had been provided as indicated in **Figure 3.1**. In the vicinity of stoichiometric composition, the CuZr intermetallic phase has the lowest Gibbs free energy as marked as blue line. When the composition shifts lightly

away from the CuZr intermetallic phase, the liquid phase (amorphous phase) has the lowest Gibbs free energy due to the different rising rates of the free energy between the liquid phase and the intermetallic phase. This makes two separated thermodynamically favored glasses formed close to the intermetallic phase, when the crystallization of intermetallic phase was suppressed during liquid quenching.

In this chapter, we systematically studied the glass formation near all the intermetallics in the Zr-Cu system. The same phenomenon (the formation of "intermetallic glass") was observed for these intermetallics: $Cu_{51}Zr_{14}$, Cu_8Zr_3, $Cu_{10}Zr_7$, and $CuZr_2$ intermetallics; and interpretation from both thermodynamic and kinetic aspects have also been provided.

3.2 Results

There are six intermetallics in the Cu-Zr system (i.e. Cu_9Zr_2, $Cu_{51}Zr_{14}$, Cu_8Zr_3, $Cu_{10}Zr_7$, CuZr and $CuZr_2$), and the glass formation near $Cu_{51}Zr_{14}$, Cu_8Zr_3, $Cu_{10}Zr_7$ and $CuZr_2$ intermetallics is studued.

3.2.1 Glass formation near $CuZr_2$ intermetallic

For alloys with compositions near $CuZr_2$ intermetallic, the alloys are cast into wedge shape to determine the critical sizes. **Figure 3.2** shows the SEM cross-section photos for wedge cast samples with compositions changing from $Cu_{36.33}Zr_{63.67}$ to $Cu_{30.33}Zr_{69.67}$, and the boundaries between crystallization phase and amorphous phase are pointed by arrows. The critical thicknesses were obtained by measuring the width of these wedges at arrows and summarized in **Figure 3.3**. It clearly shows that alloys $CuZr_2$ ($Cu_{33.33}Zr_{66.67}$), $Cu_{32.83}Zr_{67.17}$ and $Cu_{32.33}Zr_{67.67}$ are almost fully crystalline structure. The critical thickness reaches 470 μm at composition $Cu_{34.33}Zr_{65.67}$ and falls down to 360 μm at composition $Cu_{36.33}Zr_{63.67}$ when Zr content decreases. On the other side, when more Zr is added, the critical thickness reaches maximum 400 μm at composition $Cu_{31.33}Zr_{68.67}$ and goes down to 300 μm at composition $Cu_{30.33}Zr_{69.67}$ by further addition of Zr. So in the studied composition range, there are two peaks in glass forming ability at compositions $Cu_{34.33}Zr_{65.67}$ and $Cu_{31.33}Zr_{68.67}$ respectively, which are located at different sides of $CuZr_2$ intermetallic. To confirm this result, all wedges were cut at the thickness about 500 μm for the DSC (indicated by the red line in **Figure 3.2**). The DSC results are shown in **Figure 3.4**. Enthalpies of crystallization of these wedges are plotted together with critical size in **Figure 3.3**.

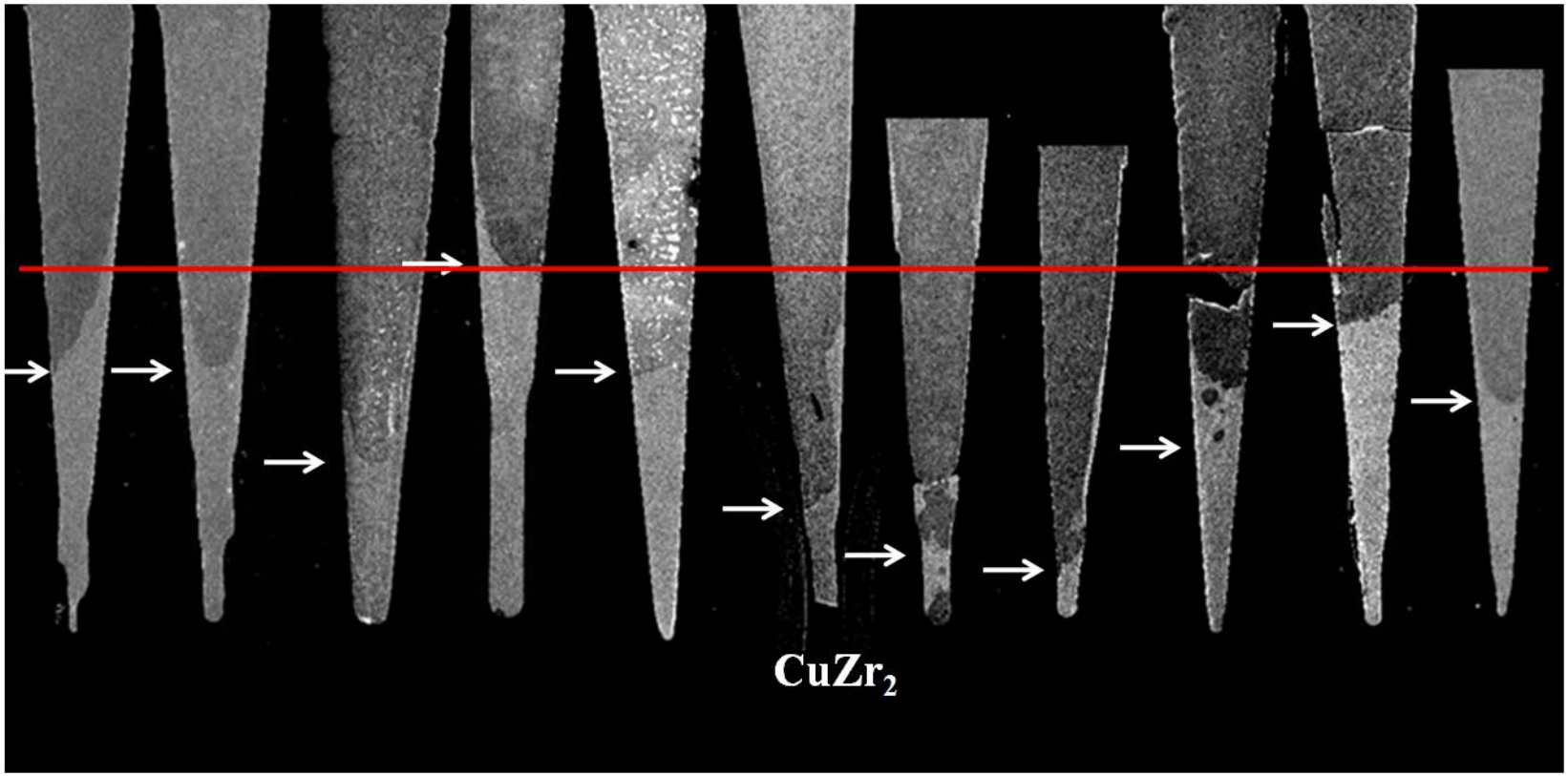

Figure 3.2 SEM photos of wedge cast samples with compositions from $Cu_{36.33}Zr_{63.67}$ to $Cu_{30.33}Zr_{69.67}$. The arrows all point to the critical thicknesses (boundary between crystalline phase and amorphous phase) and the red line represents the cutting edge for the DSC test.

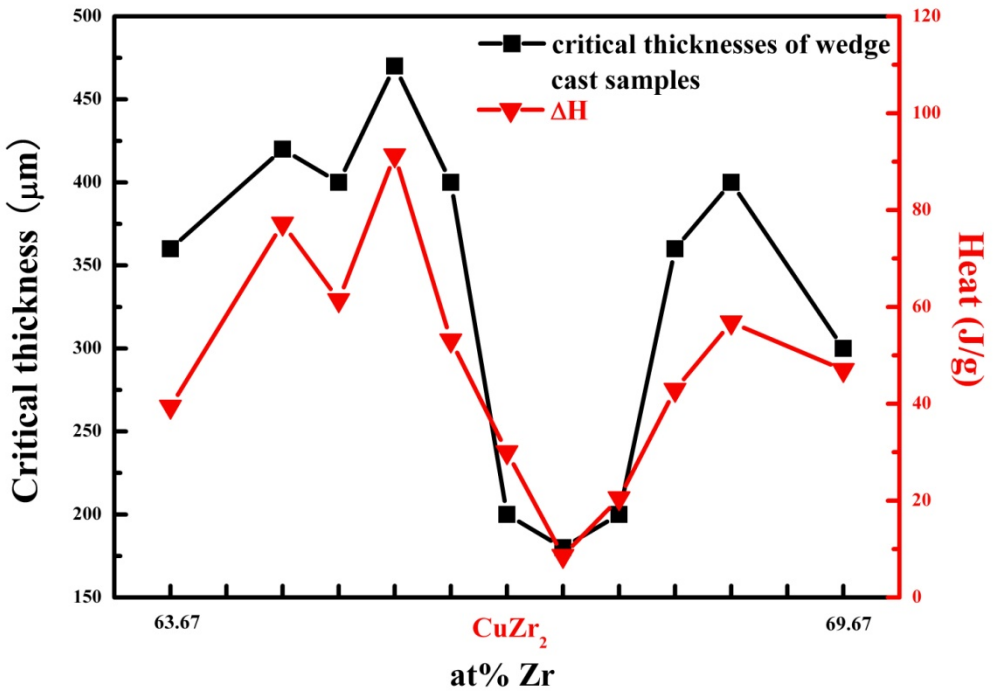

Figure 3.3 Summary of critical sizes and the enthalpy of crystallization of wedge cast samples.

The changing of the values of enthalpy of crystallization is in good agreement with the changing of corresponding critical thicknesses. $CuZr_2$ ($Cu_{33.33}Zr_{66.67}$), $Cu_{32.83}Zr_{67.17}$ and $Cu_{32.33}Zr_{67.67}$ have the lowest enthalpies of crystallization of 30.0 J/g, 8.6 J/g and 20.5 J/g, respectively, as same as they have the smallest critical thicknesses. Enthalpies of crystallization for compositions $Cu_{34.33}Zr_{65.67}$ and $Cu_{31.33}Zr_{68.67}$ (two optimum glass formers) are 91.3 J/g and 56.8 J/g respectively, which are the highest two values among their neighborhood compositions. This further confirms that there is a pair of optimum glass formers formed separated of $CuZr_2$ intermetallic.

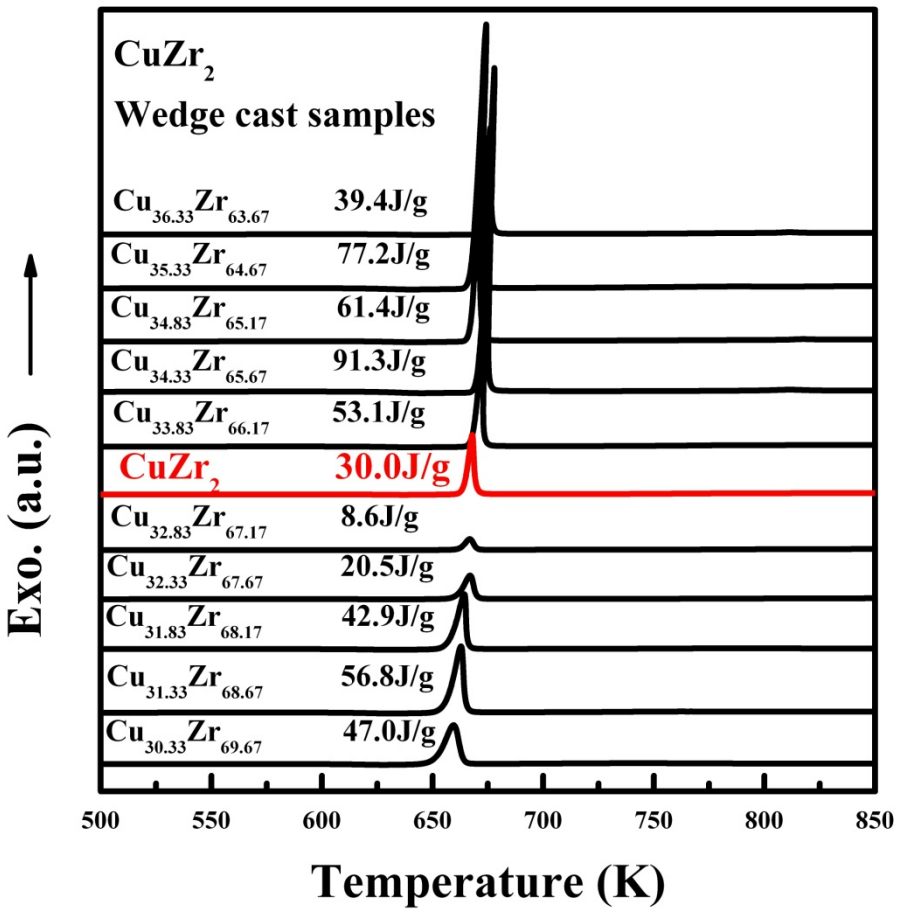

Figure 3.4 DSC curves of the tip parts of wedge cast samples.

3.2.2 Glass formation near $Cu_{10}Zr_7$ intermetallic

For alloys with compositions near $Cu_{10}Zr_7$ intermetallic, the alloys are also cast into wedge shape to determine the critical sizes. **Figure 3.5** shows the cross-section optical photos of these wedge cast samples, with arrows point to the boundaries between crystallization phase and amorphous phase. The critical thicknesses can be obtained by measuring the width of the wedges

where the arrows located, and the changing of critical thicknesses with compositions near $Cu_{10}Zr_7$ intermetallic is summarized in **Figure 3.6**.

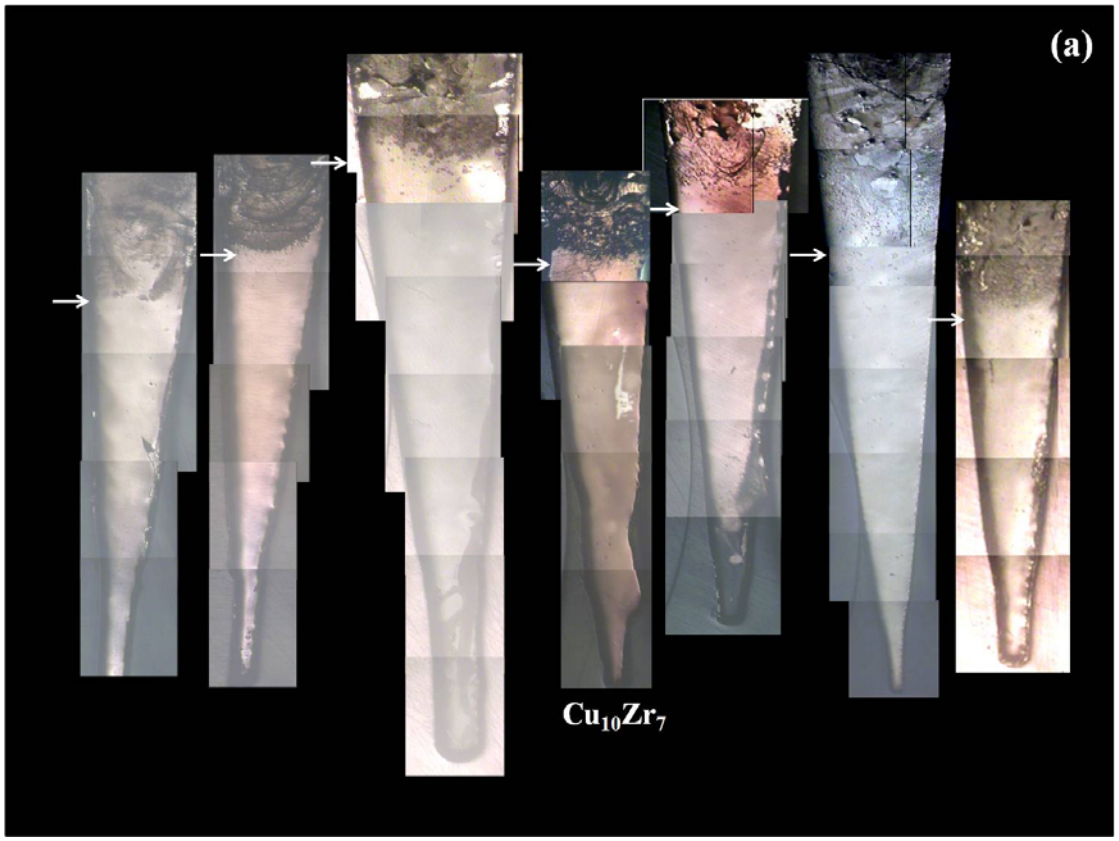

Figure 3.5 OM photos of wedge cast samples with compositions from $Cu_{60.32}Zr_{39.68}$ to $Cu_{57.32}Zr_{42.68}$. The arrows all point to the critical thicknesses.

It shows that the critical thickness increases from 320 μm at $Cu_{60.32}Zr_{39.68}$ to the highest point of 520 μm at $Cu_{59.32}Zr_{40.68}$, and then decreases to 380 μm at $Cu_{10}Zr_7$ ($Cu_{58.82}Zr_{41.18}$). The critical thickness reaches another peak point of 460 μm at $Cu_{58.32}Zr_{41.68}$ when the Zr content keeps increasing and finally falls down to 320 μm again at $Cu_{57.32}Zr_{42.68}$. The minimum critical thicknesses of 320 μm on both ends of this composition ranges and the critical thickness of 380 μm at $Cu_{10}Zr_7$ suggest that there are two peaks in glass forming ability (520 and 460

μm respectively) among these compositions, which are located at different sides of $Cu_{10}Zr_7$ intermetallic. **Figure 3.7** shows all DSC curves for all wedge cast samples at width about 520 μm, and the trend of enthalpy of crystallization is almost consistent with that of critical thicknesses. The enthalpy of crystallization for all samples are calculated and summarized in **Figure 3.2**. Enthalpies of crystallization for compositions $Cu_{59.32}Zr_{40.68}$ and $Cu_{58.32}Zr_{41.68}$ are 53.2 J/g and 44.2 J/g respectively, which are the highest two values of among their neighborhood compositions. This further confirms that there is a pair of optimum glass formers formed separated of $Cu_{10}Zr_7$ intermetallic.

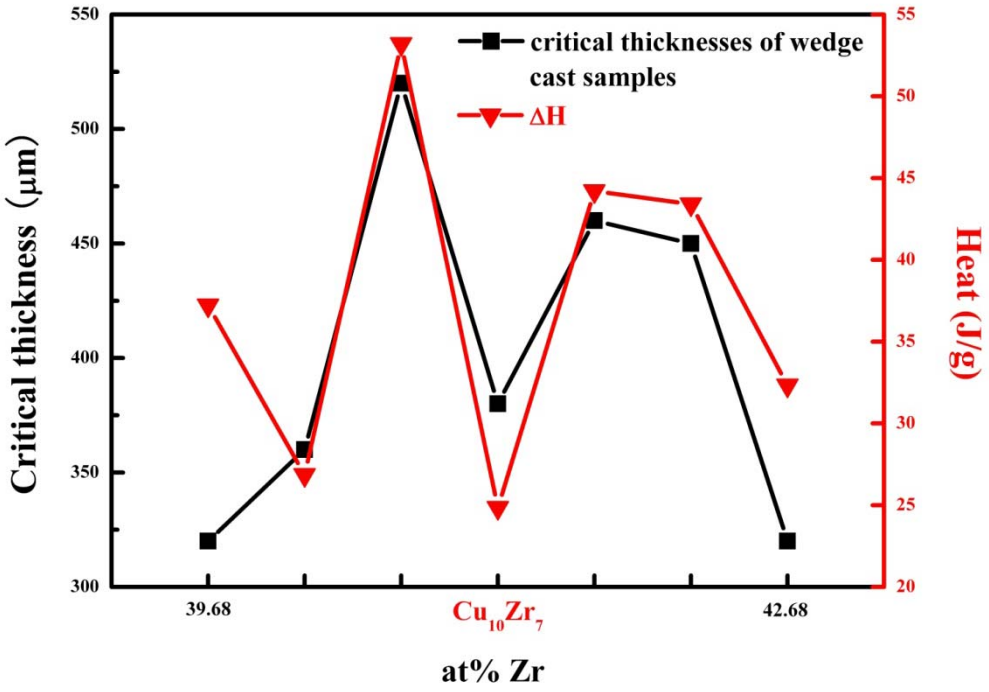

Figure 3.6 Summary of critical sizes and the enthalpy of crystallization of wedge cast samples.

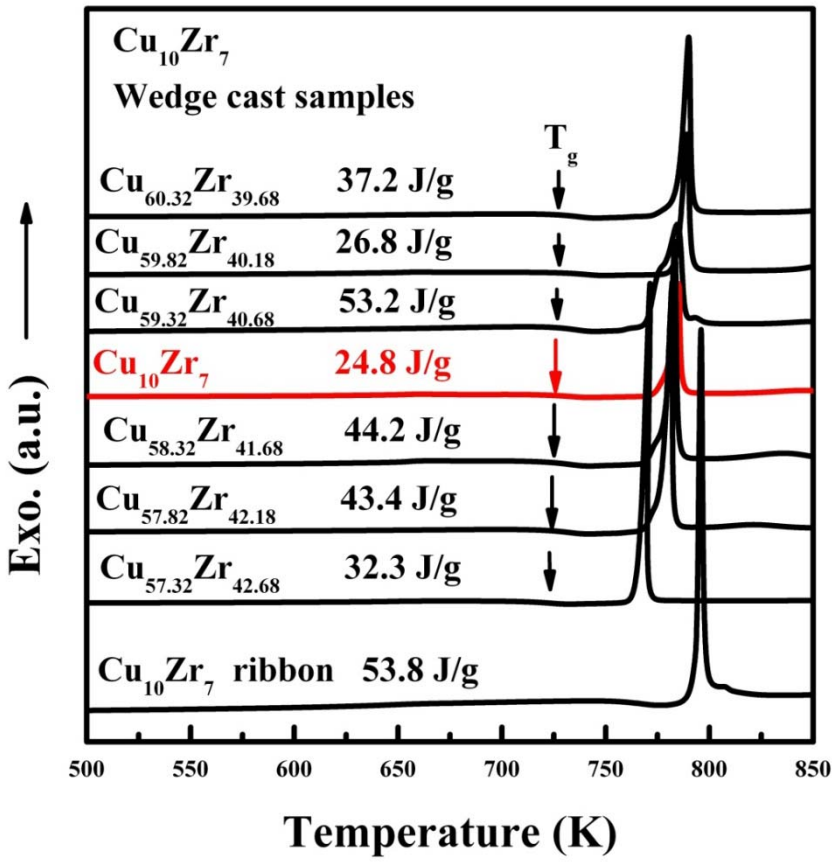

Figure 3.7 DSC curves of the tip parts of wedge cast samples.

3.2.3 Glass formation near $Cu_{51}Zr_{14}$ intermetallic

The glass forming ability near $Cu_{51}Zr_{14}$ phase, which has the highest melting point among the studied intermetallics, is relatively poor. The glass formation of six compositions ($Cu_{79.96}Zr_{20.04}$, $Cu_{79.46}Zr_{20.54}$, $Cu_{78.96}Zr_{21.04}$, $Cu_{78.46}Zr_{21.54}$, $Cu_{77.96}Zr_{22.04}$ and $Cu_{78.46}Zr_{22.54}$) was carefully studied and only ribbons with thickness about 15 μm were obtained. **Figure 3.8** shows the results of DSC studies of these ribbons. Although the enthalpies of crystallization are small, there are three compositions exhibiting the presence of amorphous phase: $Cu_{51}Zr_{14}$ ($Cu_{78.46}Zr_{21.54}$), $Cu_{79.46}Zr_{20.54}$ and $Cu_{79.96}Zr_{20.04}$. In the middle of these

three alloys, the enthalpy of crystallization of $Cu_{78.96}Zr_{21.04}$ is zero, indicating it has a fully crystalline structure. These DSC results are in good agreement with the corresponding XRD patterns of chill-side of these ribbons (as shown in **Figure 3.9**). Due to the small amount of amorphous, only tiny humps of amorphous phase with peaks of $Cu_{51}Zr_{14}$ crystalline phase can be seen in the patterns of $Cu_{78.46}Zr_{21.54}$, $Cu_{79.46}Zr_{20.54}$ and $Cu_{79.96}Zr_{20.04}$. Both DSC and XRD results confirm two peaks of glass forming ability near $Cu_{51}Zr_{14}$ intermetallic.

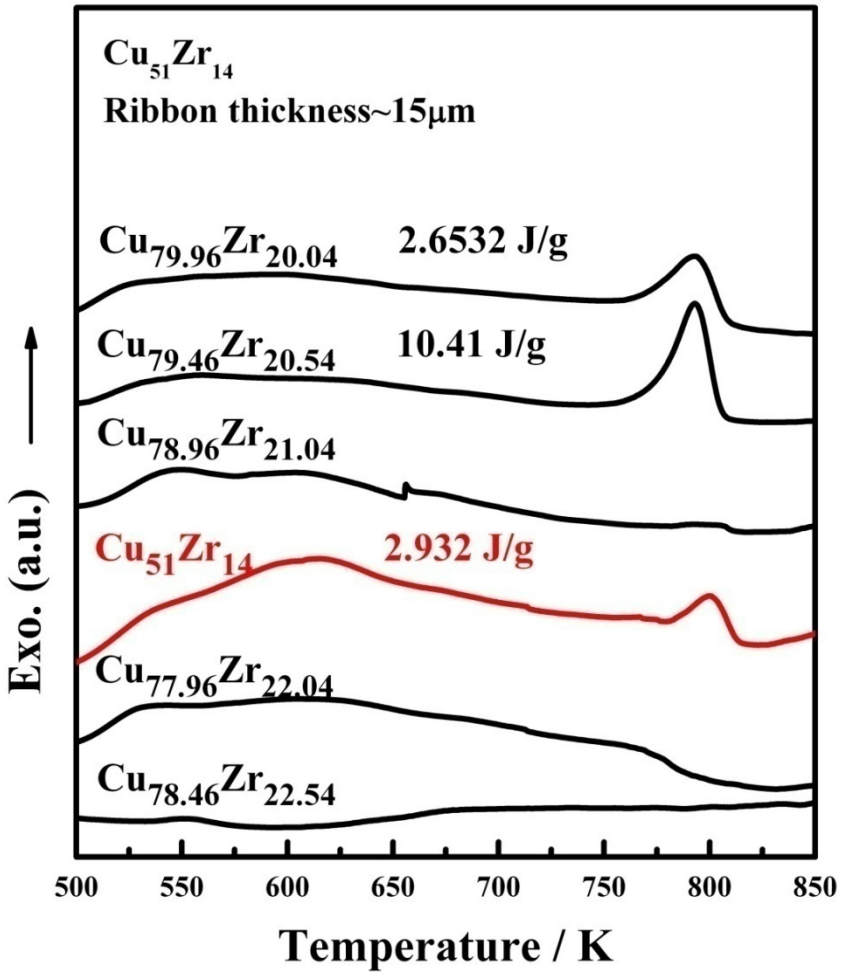

Figure 3.8 DSC curves of 15 μm ribbons of compositions near $Cu_{51}Zr_{14}$ intermetallic.

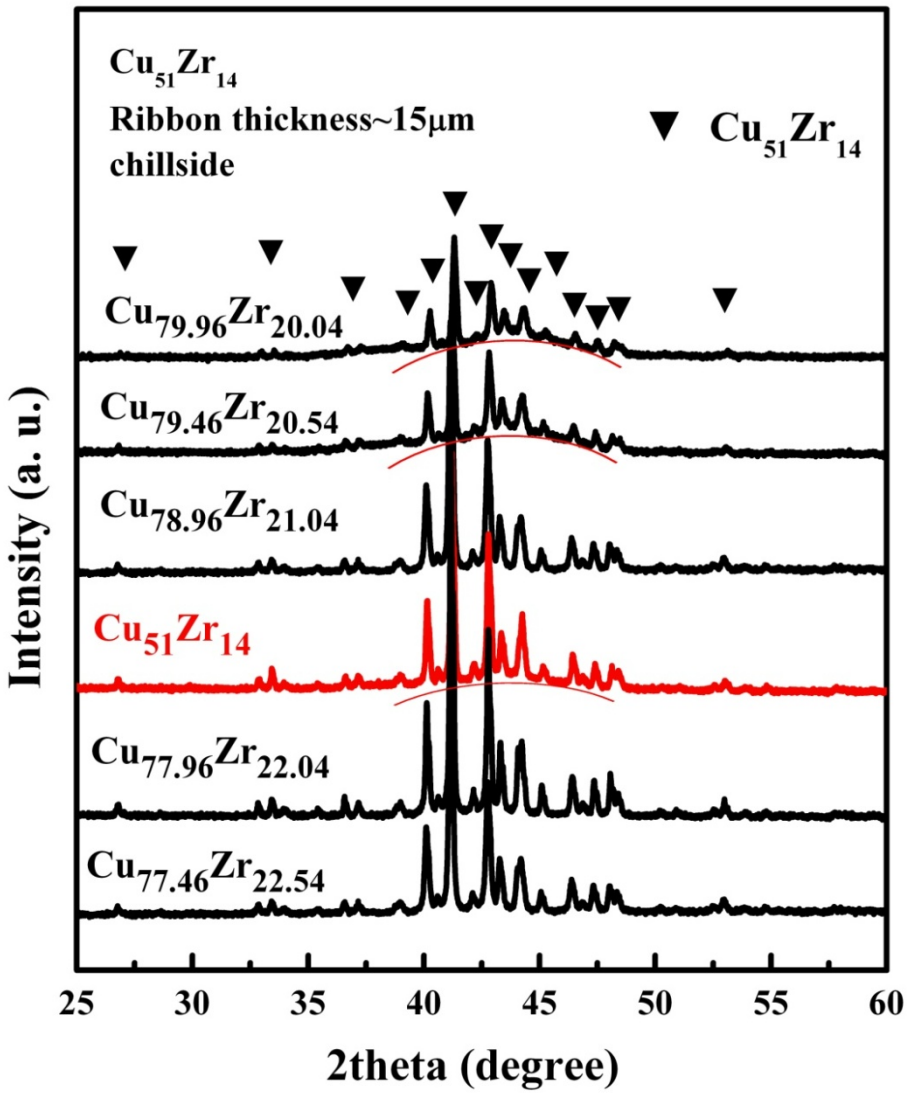

Figure 3.9 XRD patterns of the chill-side of the ribbons with compositions near $Cu_{51}Zr_{14}$ intermetallic.

3.2.4 Glass formation near Cu_8Zr_3 intermetallic

Finally, glass forming ability near Cu_8Zr_3 intermetallic is also studied. **Figure 3.10** shows the DSC curves for ribbons with 20 μm thickness of six compositions (from $Cu_{74.23}Zr_{25.77}$ to $Cu_{71.73}Zr_{28.27}$). The enthalpies of crystallization are listed in **Figure 3.10**. The DSC results show that there are

amorphous phase in compositions Cu_8Zr_3 ($Cu_{72.73}Zr_{27.27}$), $Cu_{72.23}Zr_{27.77}$ and $Cu_{71.73}Zr_{28.27}$. The XRD patterns of the chill-side of these ribbons are shown in **Figure 3.11**. The XRD patterns of compositions Cu_8Zr_3, $Cu_{72.23}Zr_{27.77}$ and $Cu_{71.73}Zr_{28.27}$ clearly show that crystalline diffraction peaks are located on a broad amorphous hump. This is consistent with the DSC results.

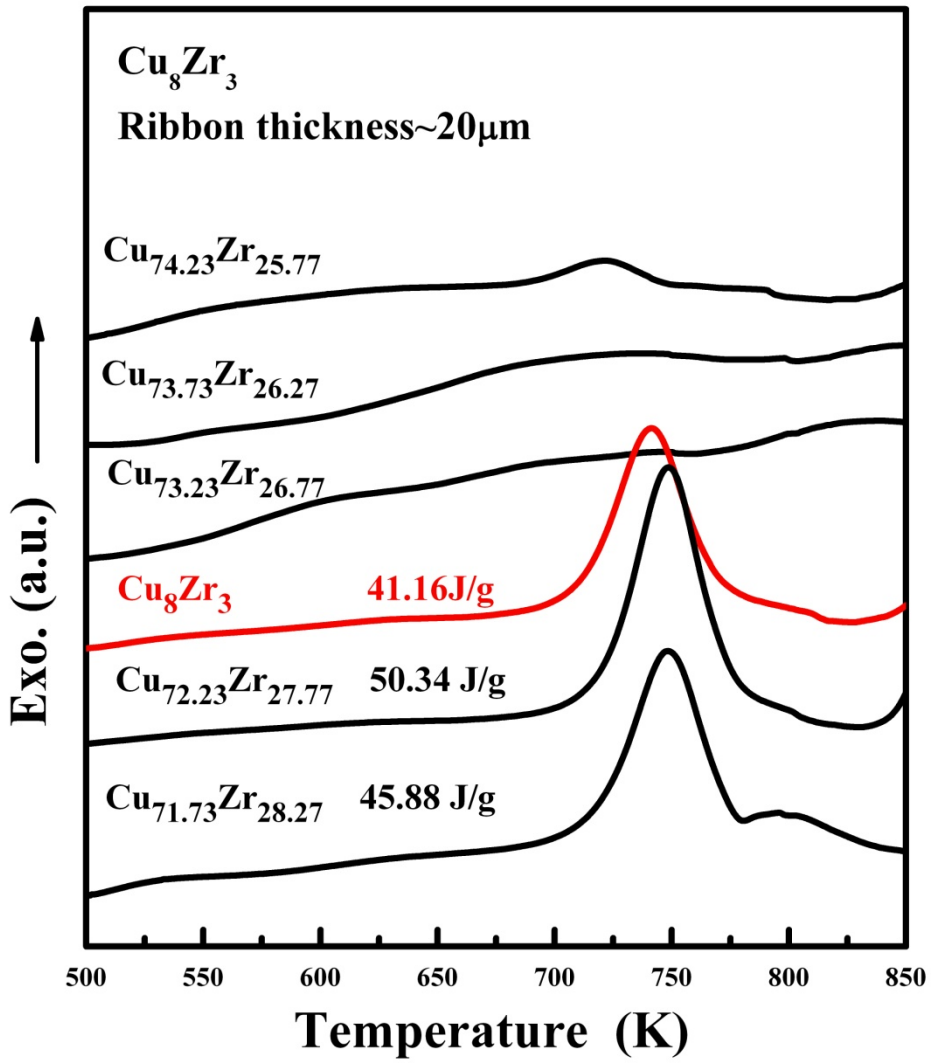

Figure 3.10 DSC curves of 20 μm ribbons of compositions near Cu_8Zr_3 intermetallic.

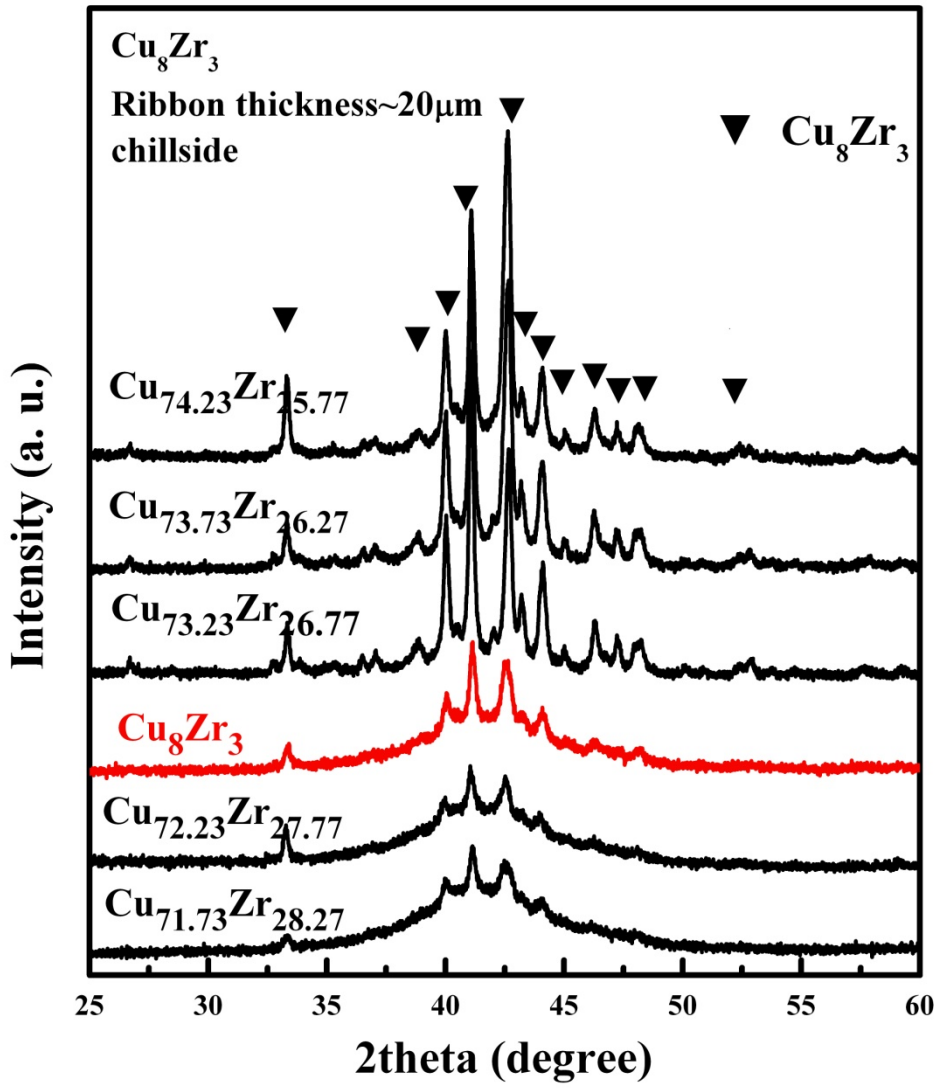

Figure 3.11 XRD patterns of the chill-side of the ribbons with compositions near Cu_8Zr_3 intermetallic.

However, compositions $Cu_{74.23}Zr_{25.77}$, $Cu_{73.73}Zr_{26.27}$ and $Cu_{73.23}Zr_{26.77}$ show no evidence of amorphous phase in both DSC and XRD results. It can be explained that the liquidus line drops with the increasing Zr content (as showed in **Figure 3.12**) near Cu_8Zr_3 intermetallic, and compositions with lower liquidus temperatures can be quenched into amorphous phase much

more easily. This may cause all the compositions with high Zr content (Cu_8Zr_3, $Cu_{72.23}Zr_{27.77}$ and $Cu_{71.73}Zr_{28.27}$) can form amorphous in the ribbons with 20 μm thickness but compositions ($Cu_{74.23}Zr_{25.77}$, $Cu_{73.73}Zr_{26.27}$ and $Cu_{73.23}Zr_{26.77}$) with low Zr content cannot. Therefore, according to the enthalpies of crystallization of the alloys, there is only one peak in glass forming ability near Cu_8Zr_3 intermetallic.

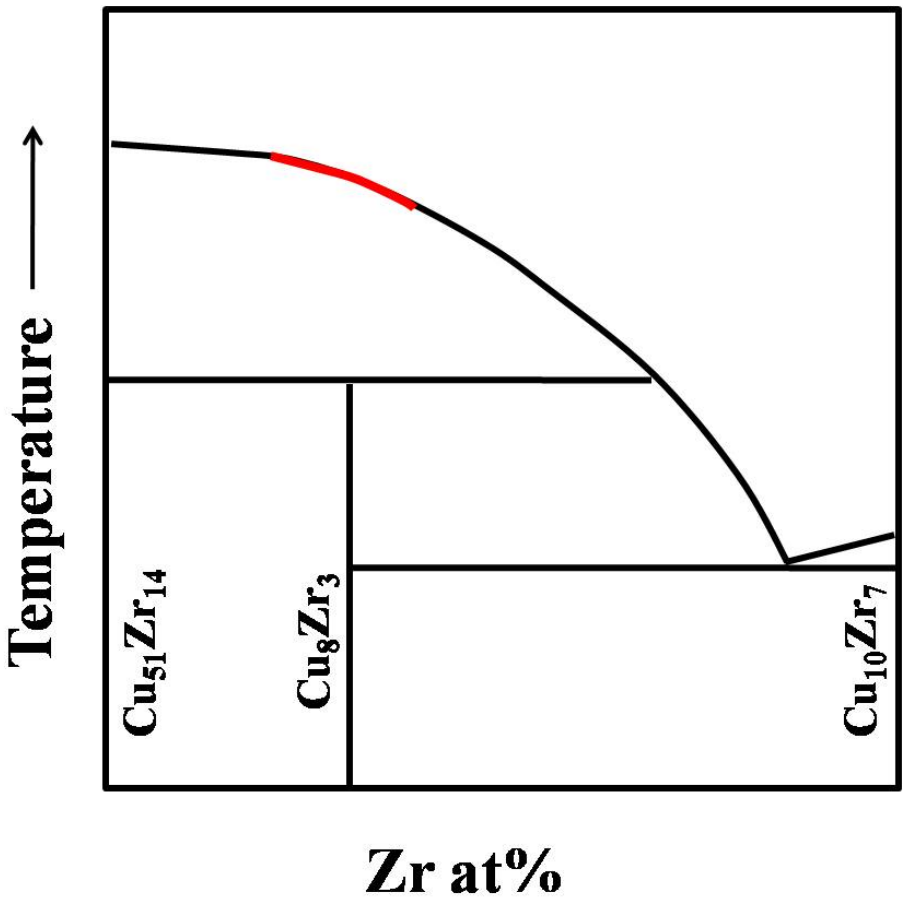

Figure 3.12 Partial Cu-Zr binary phase diagram.

In summary, glass formation near $Cu_{51}Zr_{14}$, Cu_8Zr_3, $Cu_{10}Zr_7$, and $CuZr_2$ intermetallics has been studied. Including the previous results on CuZr intermetallic, the formation of intermetallic glass, i.e. two peaks in glass

forming ability near but separated by the intermetallic phase, has been confirmed. Only Cu_8Zr_3 intermetallic is an exception, while there is only one peak in glass forming ability near it. This may be caused by the fact that Cu_8Zr_3 intermetallic is a peritectic phase. To compare the composition range of glass formation of eutectic glasses and intermetallic glasses, the critical sizes and the corresponding compositions of all the glass formers in Cu-Zr binary system are summarized in **Table 3.1** and are also plotted in **Figure 3.13** [57, 78, 81, 109-111]. It clearly shows that the intermetallic glasses have different glass formation ranges from those of the eutectic glasses. Furthermore, despite the fact that the composition is very close to the intermetallic compound, the intermetallic glass is capable to form bulk size sample, e.g. the glass near CuZr intermetallic can form 2 mm rod, which equals to the critical size of eutectic glass formers [81]. Moreover, for compositions near each intermetallic, the only phase detected by XRD is the corresponding intermetallic phase.

Table 3.1 Summary of the critical sizes of both eutectic glass formers and intermetallic glass formers

Composition range	Eutectic		Intermetallic	
	Composition	Critical size	Composition	Critical size
$Cu_{51}Zr_{14}$			$Cu_{79.46}Zr_{20.54}$	<15 μm
			$Cu_{78.46}Zr_{21.54}$	<15 μm
$Cu_{51}Zr_{14}$-$Cu_{10}Zr_7$	$Cu_{64.5}Zr_{35.5}$	2 mm		
$Cu_{10}Zr_7$			$Cu_{59.32}Zr_{40.68}$	520 μm
			$Cu_{58.32}Zr_{41.68}$	460 μm
$Cu_{10}Zr_7$-CuZr	$Cu_{45}Zr_{55}$	1.5 mm		
CuZr			$Cu_{51.5}Zr_{48.5}$	2 mm
			$Cu_{49}Zr_{51}$	2 mm
CuZr-$CuZr_2$	$Cu_{56}Zr_{44}$	1 mm		
$CuZr_2$			$Cu_{34.33}Zr_{65.67}$	470 μm
			$Cu_{31.33}Zr_{68.67}$	400 μm

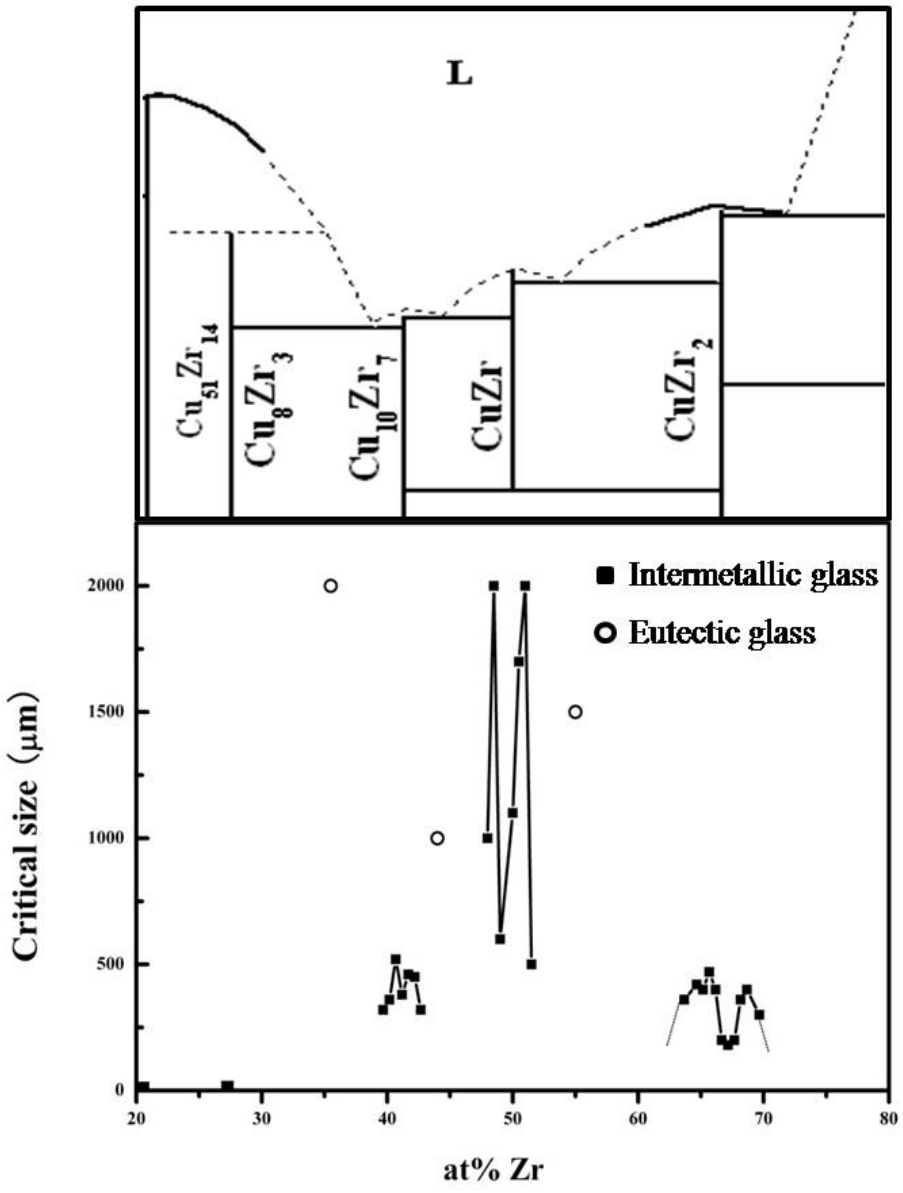

Figure 3.13 Partial of Cu-Zr binary phase diagram and summary of the critical sizes of both eutectic glass formers and intermetallic glass formers.

3.3 Discussion

3.3.1 Calculation of Gibbs free energy of liquid and intermetallic phases as a function of composition by CALPHAD method

It has been revealed that GFA is correlated with crystallization driving force whereas a smaller crystallization force often accompanies a better GFA [40, 43, 44, 112]. Generally, two methods are often used to calculate the free energy of liquid and intermetallics phases. One is the CALPHAD method (calculation of phase diagram) [113-119]. The other method is based on the Miedema model [120-123]. Here, CALPHAD method was used to calculate the Gibbs free energy as function of composition of liquid and interemetallic phases and the corresponding crystallization driving forces for the $Cu_{51}Zr_{14}$, $Cu_{10}Zr_7$, CuZr and $CuZr_2$ intermetallics.

3.3.1.1 Calculation of free energy of liquid phase

In this thesis, substitutional solution model in CALPHAD method [114] is employed to calculate the Gibbs free energy, *G*. The Gibbs free energy of the liquid phase can be described as [114]:

$$G=G^{ref}+G^{id}+G^{ex} \tag{3.1}$$

where G^{ref} is the contribution of the pure constituents, G^{id} is the contribution of ideal mixing, and G^{ex} is the non-ideal mixing contribution or the excess part:

$$G^{ref}=x_{Cu}{}^{0}G_{Cu}(T)+x_{Zr}{}^{0}G_{Zr}(T) \tag{3.2}$$

$$G^{id}=RT(x_{Cu}\,ln\,(x_{Cu})+x_{Zr}\,ln\,(x_{Zr})) \tag{3.3}$$

$$G^{ex}=x_{Cu}x_{Zr}\sum_{m=0}L^{m}_{Cu,Zr}\left(x_{Cu}-x_{Zr}\right)^{m} \tag{3.4}$$

where x_{Cu} and x_{Zr} are the molar fraction of Cu and Zr. The Gibbs free energy of pure element in liquid phase as function of temperature, ${}^{0}G_{i}(T)$, can be described as:

$${}^{0}G_{i}(T)=a+bT+cT\,ln(T)+dT^{2}+eT^{-1}+fT^{3}+gT^{4}+hT^{7}+kT^{-9} \tag{3.5}$$

where a, b, c, d, e, f, g, h and k are coefficients, and they may have different values under different temperatures; and here i represents Cu or Zr. In this chapter, the corresponding values of these coefficients for Cu and Zr were taken from the Ref. [124].

The parameter $L^{m}_{Cu,Zr}$ in equation (3.4) can be expressed as a function of

temperature, where m = 0 or 1 or 2 in liquid phase:

$$L^{m}_{Cu,Zr}=A+BT+CT\,ln(T) \tag{3.6}$$

3.3.1.2 Calculation of free energy of intermetallic phases

All intermetallic compounds were treated as stoichiometric phases due to the fact that there were no homogeneity ranges for these intermetallic compounds. The Gibbs free energy of compound Cu_iZr_j can be expressed as [125]:

$$G^{Cu_iZr_j}(T)=x_{Cu}{}^{0}G^{FCC}_{Cu}+x_{Zr}{}^{0}G^{HCP}_{Zr}+C+DT \tag{3.7}$$

where ${}^{0}G^{FCC}_{Cu}$ and ${}^{0}G^{HCP}_{Zr}$ are the free energies of pure Cu and Zr in stable solid state at 298.15K under 1 atm (the stable states are FCC_A1 for Cu and HCP_A3 for Zr), which can be obtained in Ref. [124]. The $C + DT$ part is the Gibbs free energy of formation of intermetallic phase. Here, the values of C and D were taken from Ref. [125] to calculate the free energy of $Cu_{51}Zr_{14}$, $Cu_{10}Zr_7$, CuZr and $CuZr_2$ intermetallic compounds.

3.3.1.3 The resulting Gibbs free energy of liquid and intermetallic phases

By applying eqs (3.1) to (3.7), the Gibbs free energy of liquid phase as a function of composition and that of intermetallic compositions has been calculated, as shown in **Figure 3.14**. The temperatures used are the corresponding glass transition temperatures (as listed in **Table 3.2**). As the T_g of $Cu_{51}Zr_{14}$ intermetallic is not obvious, T_x is used instead. All the expressions of the Gibbs free energies of the liquid and intermetallic phases are listed in **Table 3.3**. The crystallization driving forces at compositions of $Cu_{51}Zr_{14}$, $Cu_{10}Zr_7$, CuZr and $CuZr_2$ intermetallic compounds are plotted with the corresponding maximum critical thicknesses in **Figure 3.15**. It shows that CuZr intermetallic compound has the smallest crystallization driving force, followed by $Cu_{51}Zr_{14}$, $Cu_{10}Zr_7$, and then $CuZr_2$ intermetallic. On the other hand, the maximum critical thickness around CuZr intermetallic is 2 mm, which is the largest one, followed by $Cu_{10}Zr_7$ intermetallic (520 μm), $CuZr_2$ intermetallic (470 μm), and then $Cu_{51}Zr_{14}$ intermetallic (< 15 μm). It reveals that a smaller crystallization driving force is correlated with a better glass forming ability. The only exception is $Cu_{51}Zr_{14}$ intermetallic, which has a smaller crystallization force than $CuZr_2$ intermetallic but worse glass forming ability. However, this can be explained that $Cu_{51}Zr_{14}$ intermetallic has the highest melting temperature among all these four intermetallics, which makes the glass formation more difficult. This may imply that thermodynamic may not

be the sole determining factor for the glass formation of intermetallic glass.

Figure 3.16 shows the changing of crystallization driving force of all these four intermetallics as a function of temperature. This result is in a good agreement with the results obtained in other multi-component systems [40, 43, 44, 112], where a smaller crystallization driving force implies a smaller critical cooling rate or a better glass forming ability.

Table 3.2 Temperautre of T_g and T_x of $Cu_{51}Zr_{14}$, $Cu_{10}Zr_7$, CuZr and $CuZr_2$ intermetallics.

	T_g (K)	T_x (K)	T_m (K)	T_{rg}	Critical size
$Cu_{51}Zr_{14}$	—	760	1388	0.55	<15 μm
$Cu_{10}Zr_7$	711	761	1183	0.60	520 μm
CuZr	674	720	1220	0.55	2 mm
$CuZr_2$	615	662	1294	0.48	470 μm

Table 3.3 Gibbs free energies of liquid and intermetallic phases.

Phase	Temperature range	Function
Liquid	298.15<T<1357.77	${}^{0}G_{Cu}^{Liquid}$ =+5194.277+120.973331T-24.112392T×ln(T)-0.00265684T^{2}
		+1.29223E-7×T^{3}+52478T^{-1}-5.8489E-21×T^{7}
	1357.77<T<3200.00	${}^{0}G_{Cu}^{Liquid}$ =-46.545+173.881484T-31.38T×ln(T)
	298.15<T<2128.00	${}^{0}G_{Zr}^{Liquid}$ =+10320.095+116.568238T-24.1618T×ln(T)-0.00437791T^{2}+34971T^{-1}
		+1.6275E-22×T^{7}
	2128.00<T<6000.00	${}^{0}G_{Zr}^{Liquid}$ =-8281.26+253.812609T-42.144T×ln(T)
	298.15<T<3000.00	${}^{0}L_{Cu:Zr}^{Liquid}$ =-140638.632+444.1606T-51.3121T×ln(T)
	298.15<T<3000.00	${}^{1}L_{Cu:Zr}^{Liquid}$ =-22066.212+84.9923T-9.6125T×ln(T)
	298.15<T<3000.00	${}^{2}L_{Cu:Zr}^{Liquid}$ =56633.154-307.3817T+36.8512T×ln(T)
	298.15<T<3000.00	${}^{3}L_{Cu:Zr}^{Liquid}$ =-22368.721+119.5438T-13.6488T×ln(T)

FCC_A1	298.15<T<1357.77	${}^{0}G_{Cu}^{FCC\_A1}$=-7770.458+130.485235T-24.112392T×ln(T)-0.00265684T^{2} +1.29223E-7×T^{3}+52478T^{-1}
	1357.77<T<3200.00	${}^{0}G_{Cu}^{FCC\_A1}$=-13542.026+183.803828T-31.38T×ln(T)-0.00265684T^{2}+3.64167E +29×T^{9}
HCP_A3	130.00<T<2128.00	${}^{0}G_{Zr}^{HCP\_A3}$=-7827.595+125.64905T-24.1618T×ln(T)-0.00437791T^{2}+34971T^{-1}
	2128.00<T<6000.00	${}^{0}G_{Zr}^{HCP\_A3}$=-26085.921+262.724183T-42.144T×ln(T)-0.00265684T^{2}+1.342896E +31×T^{9}
$Cu_{51}Zr_{14}$	298.15<T<3000.00	${}^{0}G_{Cu:Zr}^{Cu_{51}Zr_{14}}$ =-10184.262-1.0260T+0.785GHSERCU+0.215GHSERZR
$Cu_{10}Zr_{7}$	298.15<T<3000.00	${}^{0}G_{Cu:Zr}^{Cu_{10}Zr_{7}}$ =-20463.114+5.8825T+0.588GHSERCU+0.412GHSERZR
CuZr	298.15<T<3000.00	${}^{0}G_{Cu:Zr}^{CuZr}$ =-14836.032+0.8587T+0.5GHSERCU+0.5GHSERZR
$CuZr_2$	298.15<T<3000.00	${}^{0}G_{Cu:Zr}^{CuZr_2}$ =-17045.108+4.2935T+0.333GHSERCU+0.667GHSERZR

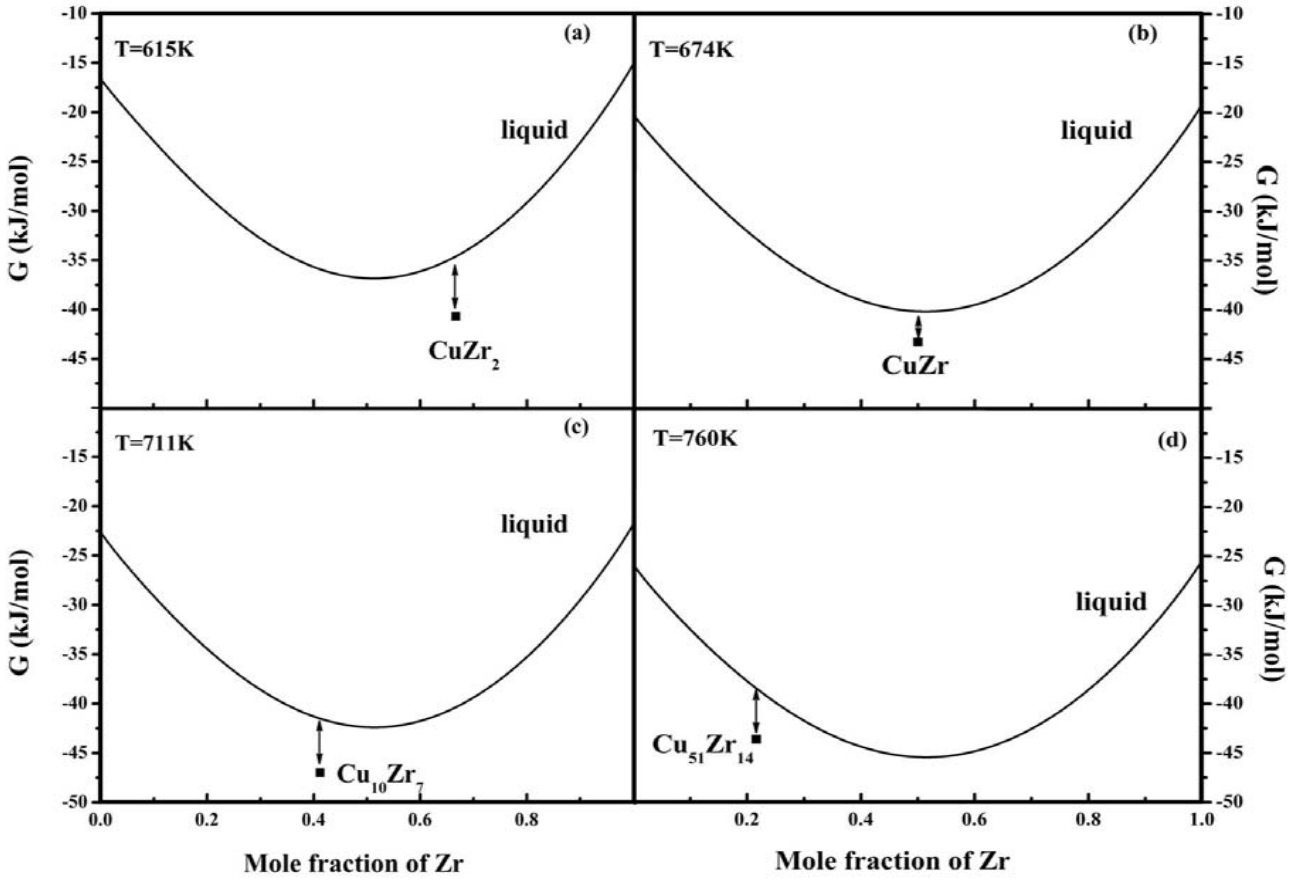

Figure 3.14 Gibbs free energy curves of liquid phase and (a)$CuZr_2$, (b) CuZr, (c) $Cu_{10}Zr_7$ and (d) $Cu_{51}Zr_{14}$ phases under their corresponding T_g or T_x temperatures.

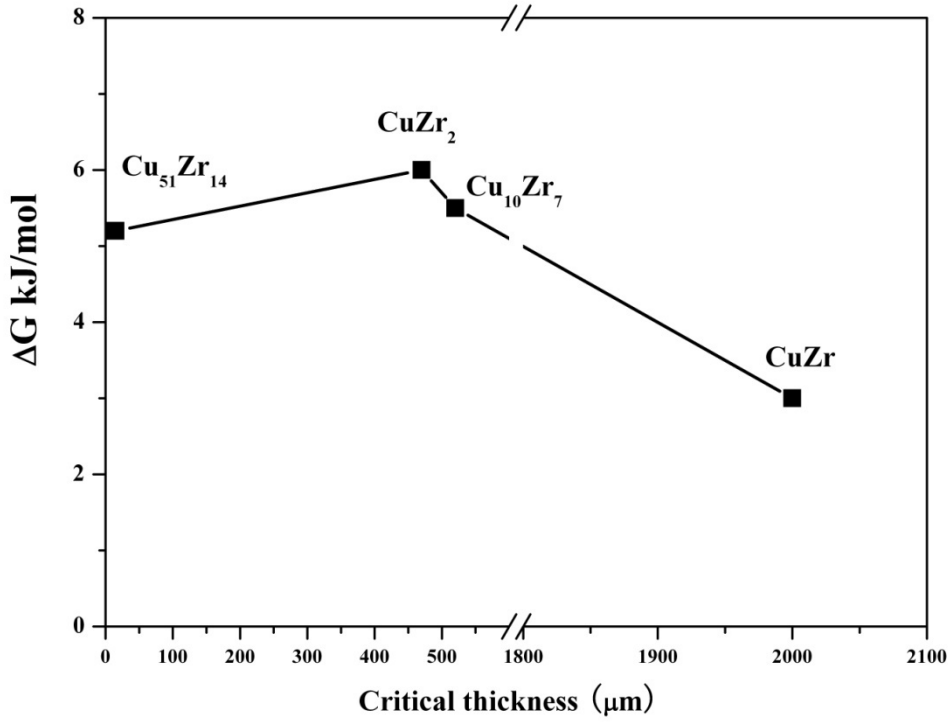

Figure 3.15 The crystallization driving force of $CuZr_2$, CuZr, $Cu_{10}Zr_7$ and $Cu_{51}Zr_{14}$ intermetallics under their corresponding T_g or T_x temperatures.

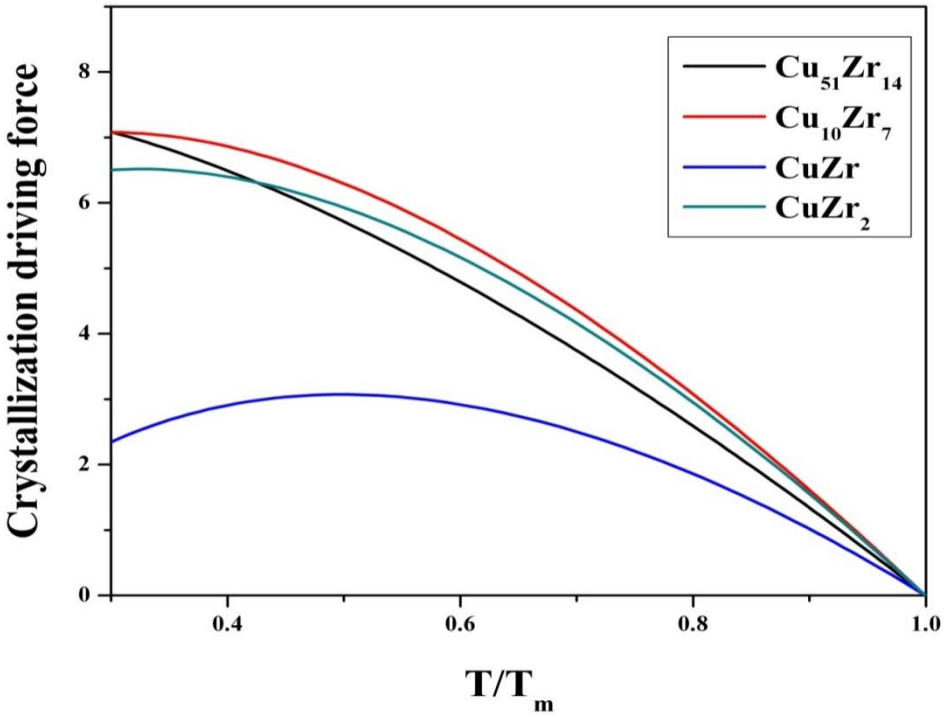

Figure 3.16 The crystallization driving forces of $CuZr_2$, CuZr, $Cu_{10}Zr_7$ and $Cu_{51}Zr_{14}$ intermetallics, which are normalized to the corresponding melting temperature.

3.3.2 The thermodynamic explanation for the formation of intermetallic glasses

3.3.2.1 The relationship between the localize minimum crystallization driving force and the optimum glass formers

Generally, the compositions with local minimum crystallization driving forces in the whole composition range should be the optimum glass formers [87, 96, 126-129]. To locate the optimum glass formers, the crystallization driving force of each intermetallic as a function of composition needs to be obtained, by the method illustrated in **Figure 3.17** [91]. As shown in **Figure 3.17(a)**, the two solid curves represent the Gibbs free energy of liquid phase and α phase, respectively. The two paralleled dash lines are the tangent lines of the Gibbs free energy of these two phases. At a certain temperature, the crystallization driving force of α phase at composition X_0 is expressed by the arrow, or line Aa. **Figure 3.17(b)** shows the schematic diagram of the resulting crystallization driving force of α phase in the whole composition range.

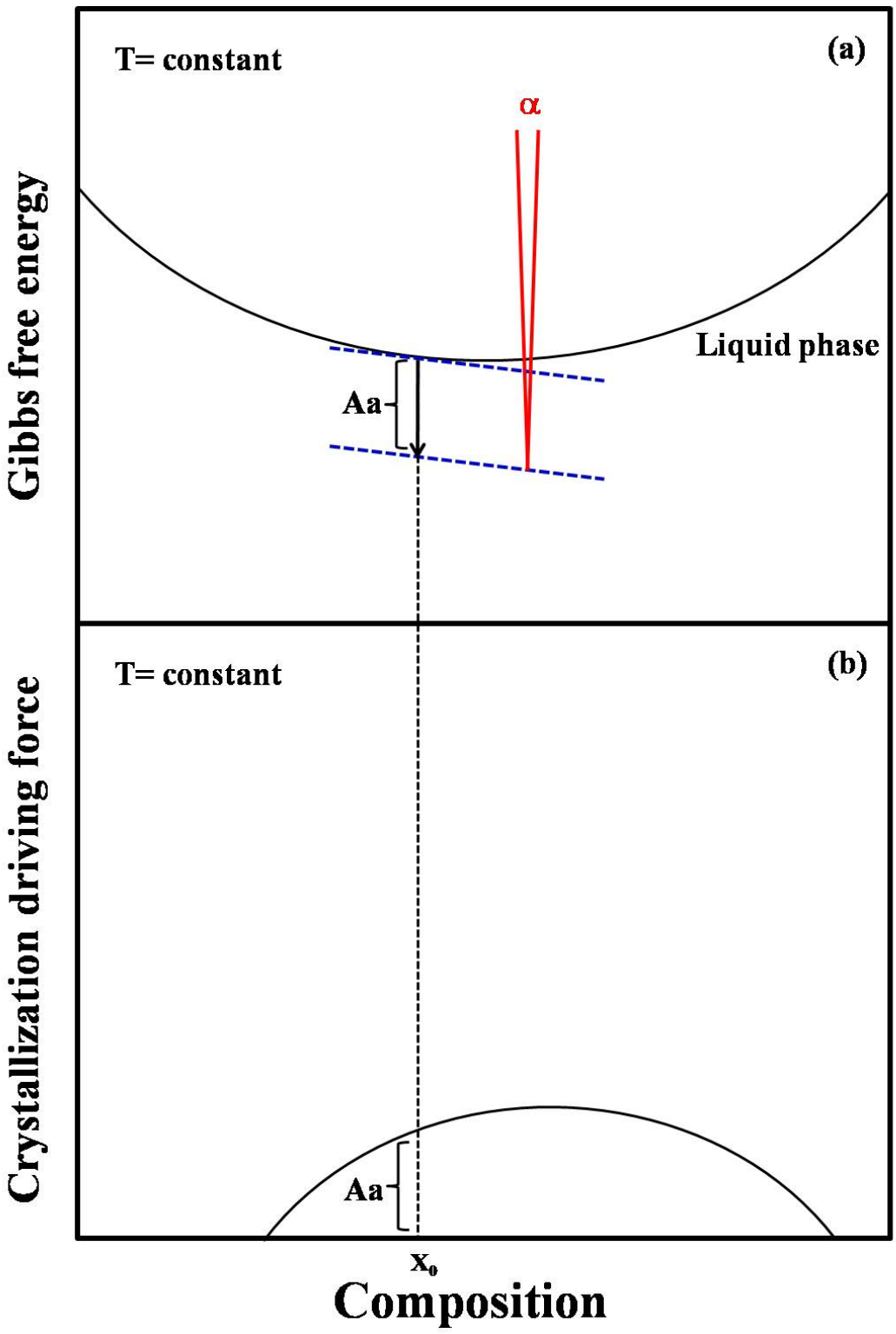

Figure 3.17 (a) sketch diagram of the method to calculate the crystallization driving force of intermetallic from the liquid with composition X_0; (b) sketch diagram of the crystallization driving force of intermetallic phase in the whole composition range.

Figure 3.18 shows the crystallization driving forces of $Cu_{51}Zr_{14}$, $Cu_{10}Zr_7$, CuZr and $CuZr_2$ intermetallics as a function of the mole fraction of Zr. The local minimum crystallization driving forces located at around 0.321 and 0.536 mole fraction of Zr suggest that there are optimum glass formers, which match two eutectic glass formers as shown in **Figure 3.13**. Obviously, there is no local minimum crystallization driving forces near each intermetallic compound, where a pair of intermetallic glass formers is experimentally located. Thus, the method using local minimum in crystallization driving force to predict optimum glass formers failed to predict the intermetallic glass formers.

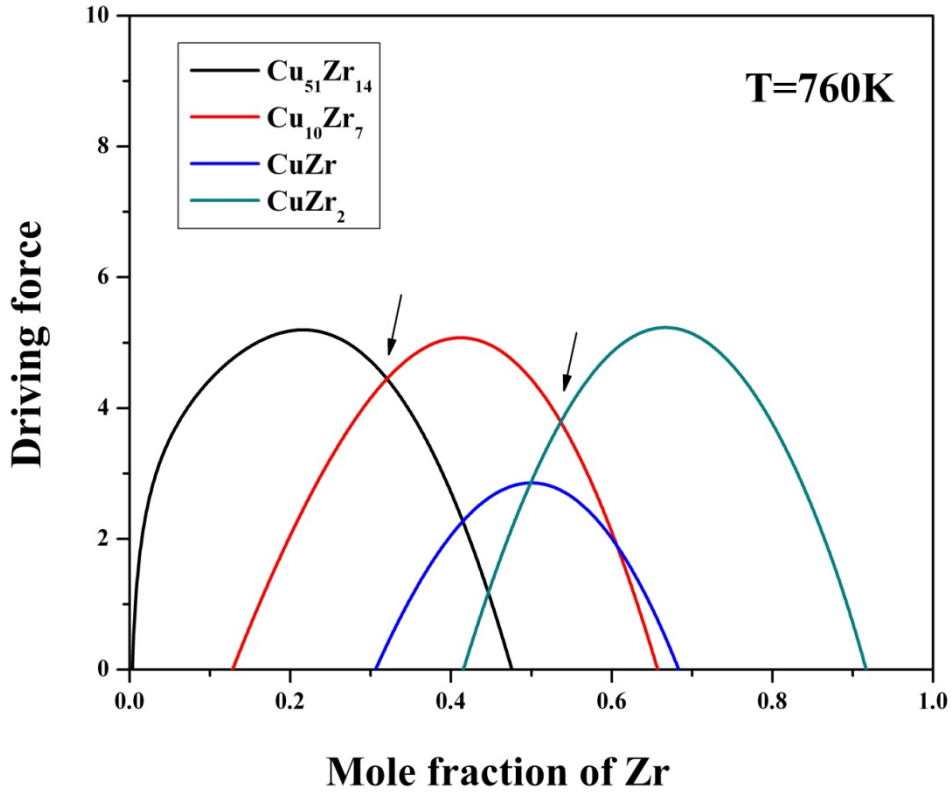

Figure 3.18 The crystallization driving force of $Cu_{51}Zr_{14}$, $Cu_{10}Zr_7$, CuZr and $CuZr_2$ intermetallic compounds in the whole composition range.

3.3.2.2 A new method to predict the formation of intermetallic glass

Due to the failure of the method mentioned in **Figure 3.17** on the glass formation of intermetallic glass, a new method was proposed to predict intermetallic glass formers, as shown in **Figure 3.19**. **Figure 3.19(a)** shows a hypothetical binary system which has two intermetallic phases α and β. The solid curves were the free energy of liquid and intermetallic phases respectively. It is proposed that the Gibbs free energy curve of intemetallic phase rises sharply once composition shifts slightly away from the intermetallic compound. Moreover, this free energy curve covers a narrow composition range only as the intermetallic phase is treated as stoichiometric composition. It should be noticed that this sharp profile free energy curve is a hypothetical one and cannot be calculated by the CALPHAD method due to there is no solubility of the intermetallic phase. Therefore, the driving force of phase formation at any composition located between these two intermetallics should be the difference between the tangent line connecting α and β phases and the free energy curve of liquid phase. However, under quenching, it is suggested that the phase formation for compositions near α phase would not be influenced by β phase anymore, as shown in **Figure 3.19(b)**. Thus the dominant factor of the phase formation would be which phase has a lower Gibbs free energy. The new method to calculate the crystallization driving force of α phase as a function of composition under quenching was illustrated

as **Figure 3.19(c)**: (1) at the intermetallic composition, the intermetallic phase has the lowest Gibbs free energy thus it is favored to be formed thermodynamically. (2) When the composition shifted slightly away from the intermetallic compound, glass is favored to be formed thermodynamically due to the liquid phase has a lower Gibbs free energy at this composition range. Thus the crystallization driving force should be considered as zero. (3) When the composition shifted further away from the intermetallic compound, it reaches the composition range beyond where the Gibbs free energy curve of α phase covered. The crystallization driving force was calculated by the method shown in **Figure 3.17**. It should be noticed that even the composition in (3) was still far away from the eutectic composition, and the phase formation still would not be influenced by β phase. **Figure 3.19(d)** shows the resulting crystallization driving force of α phase. The two compositions ranges, near the intermetallic compound, with local minima crystallization driving forces were the glass formation ranges for intermetallic glass. Our proposed thermodynamic principle successfully interprets the phenomenon of formation of intermetallic glass.

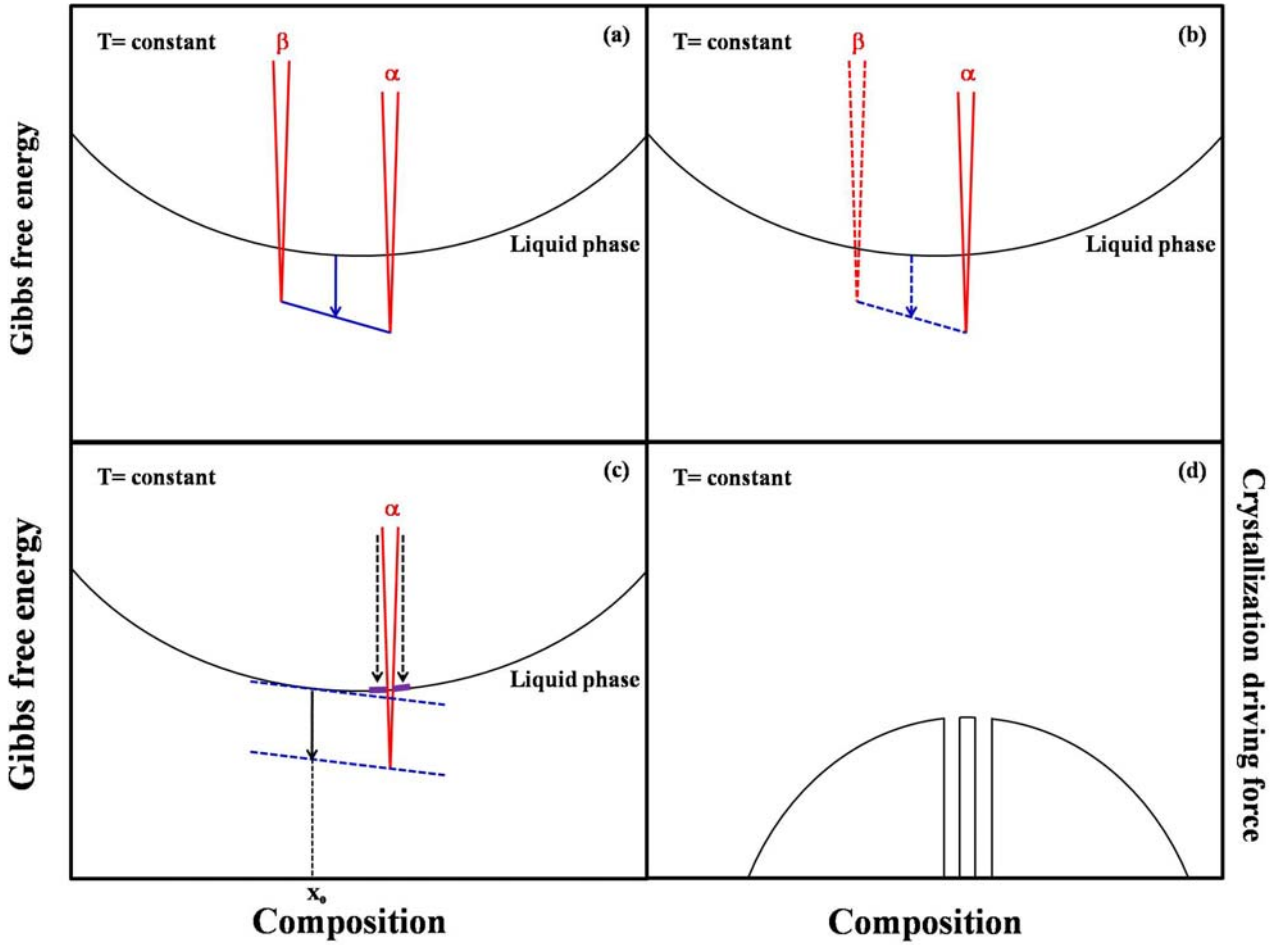

Figure 3.19 (a) a hypothetical free energy curves of liquid and intermetallic phases and the corresponding driving force of phase formation; (b) the free energy curves of liquid and intermetallic phases under liquid quenching; (c) the suggested method to calculate the crystallization driving force of intermetallic phase under liquid quenching condition; (d) the resulting crystallization driving force from (c).

3.3.3 Kinetic influence on the formation of intermetallic glasses

Even though thermodynamic consideration can predict the formation of intermetallic glass successfully, the kinetic consideration is still valuable to help to understand the underlying mechanism of this phenomenon. The kinetic consideration can be represented by the critical cooling rate (R_c) for glass formation, as a lower R_c is related to a better glass forming ability. The R_c can be estimated through construction of the time-temperature-transition (TTT) curves. In order to compare their R_c, two optimum glass formers near $Cu_{10}Zr_7$, CuZr and $CuZr_2$ intermetallics respectively ($Cu_{59.32}Zr_{40.68}$ and $Cu_{58.32}Zr_{41.68}$, $Cu_{51.5}Zr_{48.5}$ and $Cu_{49}Zr_{51}$, $Cu_{34.33}Zr_{65.67}$ and $Cu_{31.33}Zr_{68.67}$) and the three corresponding intermetallic compounds were selected to construct their TTT curves. According to the kinetic treatment of Uhlmann and Davies [130-133], the time needed for crystallization of volume fraction x can be estimated from:

$$t = \frac{9.32\eta}{kT}\left\{\frac{a_0^9 x exp(1.024/T_r^3\Delta T_r^2)}{N_v f^3[1\text{-}exp(-\Delta H_m^f \Delta T_r/RT)]^3}\right\}^{1/4} \quad (3.8)$$

where a_0 is the average atomic diameter, which equals to 0.28nm; k is the Boltzmann's constant; R is the universal gas constant; f is a structural constant

and $f = 0.2(T_m-T)/T_m$, where T_m is the melting temperature; N_v is the number of atoms per unit volume, here $N_v = 5 \times 10^{28}$atoms/m^3; $T_r = T/T_m$ and $\Delta T_r = (T_m-T)/T_m$; ΔH_m is the molar heat of fusion and all the values of T_m and ΔH_m are listed in **Table 3.4**; x was taken as 10^{-6} here [91]. The only unknown parameter is the temperature dependent viscosity η, which can be expressed by Vogel-Fulcher equation:

$$\eta(T)=Aexp(\frac{B}{T-T_0}) \tag{3.9}$$

where A, B and T_0 are constants. To determine A, B and T_0, knowledge of η or $(d\eta)/(dT)$ at three temperature points is required. According to Ref. [134-136], the following three temperature points are taken to obtain a realistic estimation for the temperature dependent viscosity (as listed in **Table 3.5**): (1) the viscosity (=10^{13} Poise) at $T=T_g$, T_g was measured at a heating rate of 0.667 K/s; (2) the viscosity (=3.5×10^{-2} Poise) at melting temperature of pure Zr (T_m=2125K); (3) $E(T_g)$ at $T=T_g$, where $E(T_g)$ is the activation energy of glass transition and can be expressed as [137-139]:

$$E(T_g)=\frac{RBT_g^2}{(T_g-T_0)^2} \tag{3.10}$$

The value of $E(T_g)$ can be determined by Kissinger plot [137-139]:

$$\frac{E}{RT} = ln\left(\frac{T^2}{r}\right) + constant \tag{3.11}$$

Table 3.4 List of the values of T_m and ΔH_m.

	$Cu_{59.32}Zr_{40.68}$	$Cu_{10}Zr_7$	$Cu_{58.32}Zr_{41.68}$
T_m **(K)**	1182	1183	1180
ΔH_m^f **(J/Mol)**	6.3×10^3	6.7×10^3	6.2×10^3
	$Cu_{51.5}Zr_{48.5}$	$Cu_{51}Zr_{49}$	$Cu_{49}Zr_{51}$
T_m **(K)**	1210	1213	1218
ΔH_m^f **(J/Mol)**	4.1×10^3	3.6×10^3	3.2×10^3
	$Cu_{34.33}Zr_{65.67}$	$CuZr_2$	$Cu_{31.33}Zr_{68.67}$
T_m **(K)**	1291	1294	1292
ΔH_m^f **(J/Mol)**	1.4×10^3	3.0×10^3	3.6×10^3

Table 3.6 lists the T_g and T_p values of selected compositions under different heating rates. Typical Kissinger plots at T_g are shown in **Figure 3.20** for the selected alloys. The values of the corresponding *A, B* and T_0 are calculated and they are listed in **Table 3.7**.

Table 3.5 List of points were taken to calculate the values of *A, B and T0*.

	$Cu_{59.32}Zr_{40.68}$	$Cu_{10}Zr_7$	$Cu_{58.32}Zr_{41.68}$
Point 1	$\eta(T_g)= 10^{13}$ Poise	$\eta(T_g)= 10^{13}$ Poise	$\eta(T_g)= 10^{13}$ Poise
Point 2	E_g=681KJ/mol Where T_g=710.3K	E_g=772KJ/mol Where T_g=711.6K	E_g=672KJ/mol Where T_g=702.6K
Point 3	$\eta(T_m$ of Zr=2125K) =$3.5x10^{-2}$ Poise	$\eta(T_m$ of Zr=2125K) =$3.5x10^{-2}$ Poise	$\eta(T_m$ of Zr=2125K) =$3.5x10^{-2}$ Poise
	$Cu_{51.5}Zr_{48.5}$	$Cu_{51}Zr_{49}$	$Cu_{49}Zr_{51}$
Point 1	$\eta(T_g)= 10^{13}$ Poise	$\eta(T_g)= 10^{13}$ Poise	$\eta(T_g)= 10^{13}$ Poise
Point 2	E_g=681KJ/mol Where T_g=682.5K	E_g=805KJ/mol Where T_g=681.5K	E_g=649KJ/mol Where T_g=670.7K
Point 3	$\eta(T_m$ of Zr=2125K) =$3.5x10^{-2}$ Poise	$\eta(T_m$ of Zr=2125K) =$3.5x10^{-2}$ Poise	$\eta(T_m$ of Zr=2125K) =$3.5x10^{-2}$ Poise
	$Cu_{34.33}Zr_{65.67}$	$CuZr_2$	$Cu_{31.33}Zr_{68.67}$
Point 1	$\eta(T_g)= 10^{13}$ Poise	$\eta(T_g)= 10^{13}$ Poise	$\eta(T_g)= 10^{13}$ Poise
Point 2	E_g=628KJ/mol Where T_g=621.0K	E_g=717KJ/mol Where T_g=615.1.0K	E_g=584KJ/mol Where T_g=606.5K
Point 3	$\eta(T_m$ of Zr=2125K) =$3.5x10^{-2}$ Poise	$\eta(T_m$ of Zr=2125K) =$3.5x10^{-2}$ Poise	$\eta(T_m$ of Zr=2125K) =$3.5x10^{-2}$ Poise

Table 3.6 T_g and T_p of selected compositions at different heating rates.

Heating rate		0.083K/s	0.167K/s	0.333K/s	0.667K/s	1.333K/s
$Cu_{59.32}Zr_{40.68}$	T_g (K)	704.2	707.7	710.3	715.8	720.9
	T_p (K)	743.9	752.7	765.0	776.1	786.2
$Cu_{10}Zr_7$	T_g (K)	707.3	709.5	711.6	716.3	721.8
	T_p (K)	744.4	757.9	769.5	781.3	791.9
$Cu_{58.32}Zr_{41.68}$	T_g (K)	700.6	701.1	702.6	710.1	714.7
	T_p (K)	735.6	745.3	755.4	766.1	775.7
$Cu_{51.5}Zr_{48.5}$	T_g (K)	675.7	677.5	682.5	686.4	690.4
	T_p (K)	714.0	723.4	733.8	742.1	752.8
$Cu_{51}Zr_{49}$	T_g (K)	675.0	678.5	681.5	686.4	686.8
	T_p (K)	714.4	724.3	732.0	742.5	751.6
$Cu_{49}Zr_{51}$	T_g (K)	664.7	668.7	670.7	676.7	680.1
	T_p (K)	705.5	713.9	723.0	734.0	743.4
$Cu_{34.33}Zr_{65.67}$	T_g (K)	614.1	616.5	621.0	622.9	628.0
	T_p (K)	657.0	668.5	678.6	689.8	699.3
$CuZr_2$	T_g (K)	610.5	612.2	615.1	618.4	622.2
	T_p (K)	652.4	664.8	675.4	691.7	696.0
$Cu_{31.33}Zr_{68.67}$	T_g (K)	599.3	604.0	606.5	609.1	614.3
	T_p (K)	640.5	650.1	663.2	675.1	691.8

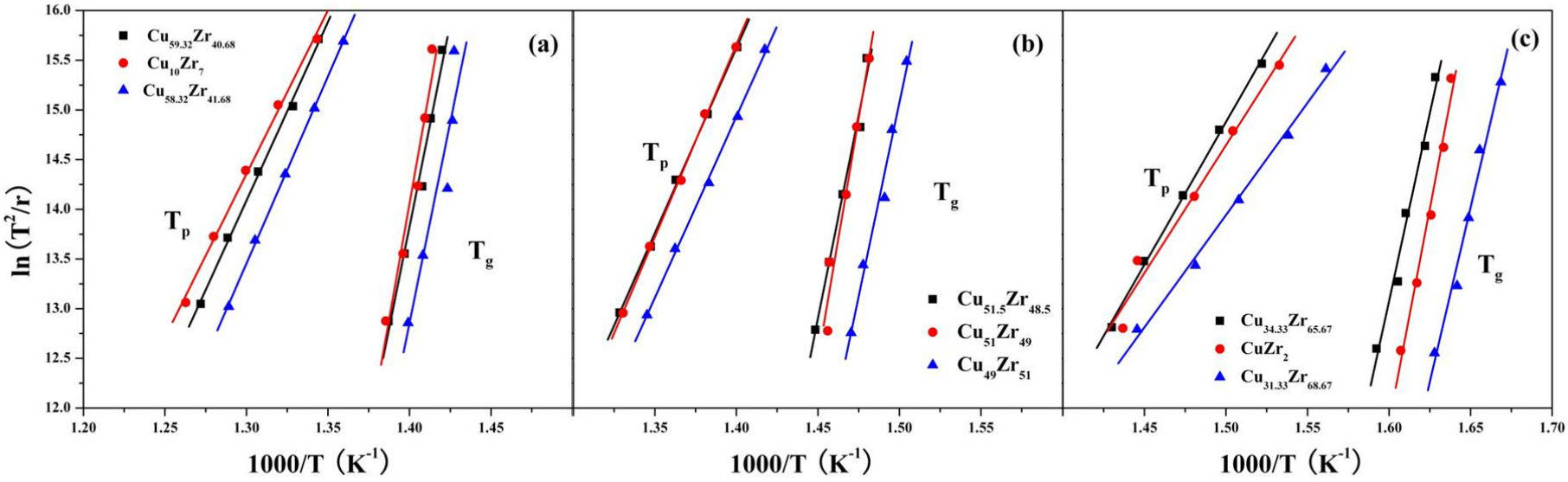

Figure 3.20 ln(T^2/r) versus 1000/T for T_g and T_p of (a) compositions near $Cu_{10}Zr_7$ intermetallic compound; (b) compositions near CuZr intermetallic compound; (c) compositions near $CuZr_2$ intermetallic compound; the lines are the best fit lines.

The resulting viscosities as a function of temperature of the selected alloys are shown in **Figure 3.21**. It clearly shows that the viscosity curves of the two intermetallic glass formers (e.g. $Cu_{59.32}Zr_{40.68}$ and $Cu_{58.32}Zr_{41.68}$) near each intermetallic (e.g. $Cu_{10}Zr_7$ intermetallic) have a similar trend. However, the viscosity curve of the corresponding interemetallic composition (e.g. $Cu_{10}Zr_7$ ($Cu_{58.82}Zr_{41.18}$)) has a lower viscosity at high temperature but rises more quickly than that of the nearby intermetallic glass formers when temperature decreases.

Table 3.7 List of the values of *A*, *B* and T_0.

	A	**B**	**T_0**
$Cu_{59.32}Zr_{40.68}$	5.118×10^{-5}	10928.762	450.810
$Cu_{10}Zr_7$	1.218×10^{-4}	9273.487	486.785
$Cu_{58.32}Zr_{41.68}$	5.709×10^{-5}	10776.071	446.070
$Cu_{51.5}Zr_{48.5}$	1.047×10^{-4}	9752.947	446.925
$Cu_{51}Zr_{49}$	2.965×10^{-4}	7810.424	487.980
$Cu_{49}Zr_{51}$	1.015×10^{-4}	9893.202	431.918
$Cu_{34.33}Zr_{65.67}$	2.631×10^{-4}	8368.582	414.262
$CuZr_2$	5.791×10^{-4}	6907.203	440.972
$Cu_{31.33}Zr_{68.67}$	2.373×10^{-4}	8644.413	393.991

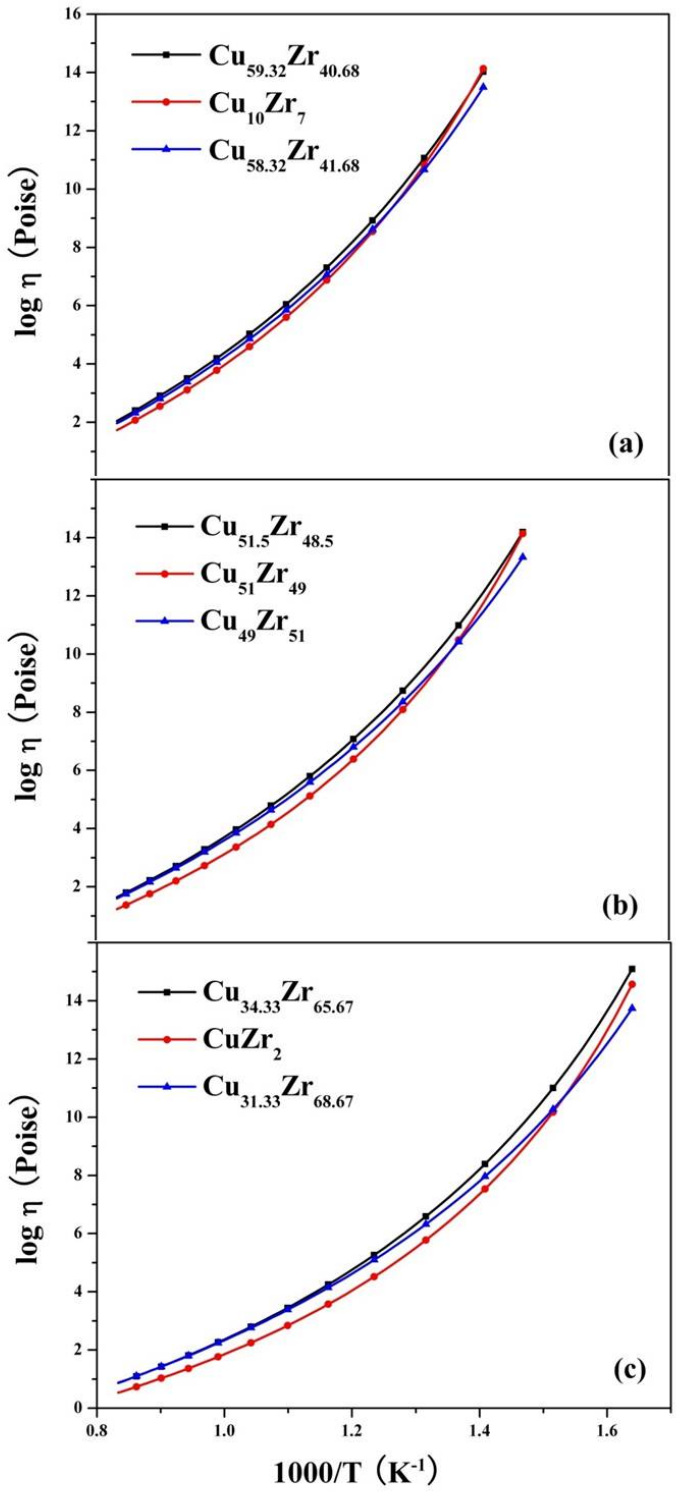

Figure 3.21 The viscosity curves of (a) compositions near $Cu_{10}Zr_7$ interemtallic compound; (b) compositions near CuZr interemtallic compound; (c) compositions near $CuZr_2$ interemtallic compound.

Based on equation (3.8), the TTT curves of the selected alloys were calculated, and **Figure 3.22** shows the results. Based on these TTT curves, the critical cooling rates are approximated by:

$$R_c = \frac{T_m - T_n}{t_n} \tag{3.12}$$

where T_n and t_n are the temperature and time of the nose of the corresponding TTT curves, respectively. **Table 3.8** lists the values of R_c for the selected alloys. Some of them are unrealistically low down to ~10^{-6}K/s, this may be caused by the fact that some values of the parameters are estimated during the construction of TTT curves. However, qualitatively, it still surprisingly clearly shows that the trend of values of R_c matches that of critical thicknesses. Among the selected alloys near $Cu_{10}Zr_7$, CuZr and $CuZr_2$ intermetallics respectively, the intermetallic compound, which has the smallest experimental critical thickness, always has a higher critical cooling rate than the two optimum glass formers near it. For instance, $CuZr_2$ ($Cu_{33.33}Zr_{66.67}$) has the highest critical cooling rate at 1.4 K/s, and then followed by $Cu_{31.33}Zr_{68.67}$ at 0.4 K/s and $Cu_{34.33}Zr_{65.67}$ at 0.1 K/s. This matches with the experimental critical thicknesses as 180 μm, 400 μm and 470 μm, respectively. This match provides a direct confirmation that kinetic consideration plays an important role in the determination of the glass forming ability of intermetallic glass.

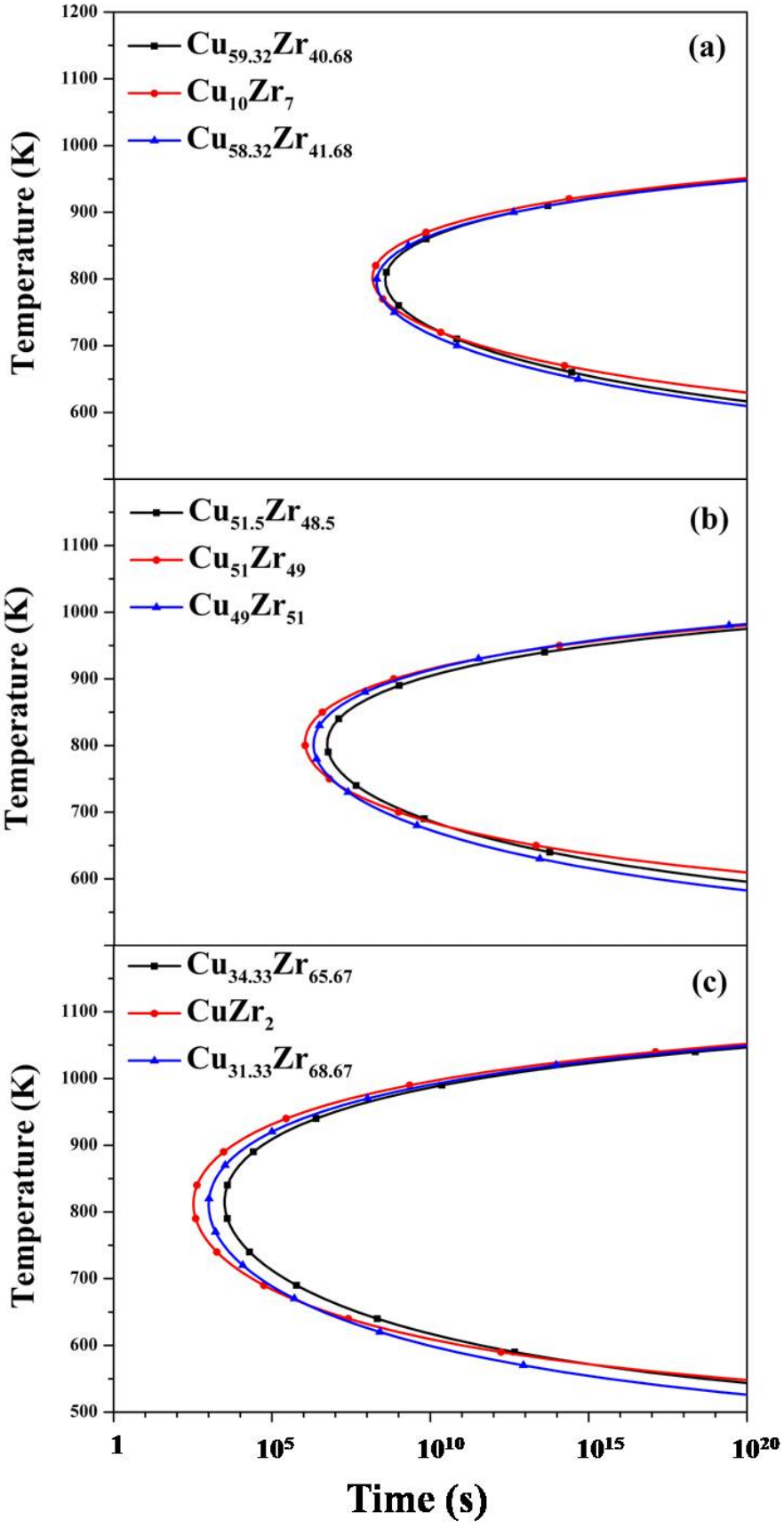

Figure 3.22 Calculated TTT curves of selected composition.

Table 3.8 the critical cooling rate, R_c, for the selected alloys.

Composition	Critical cool rate(K/s)
$Cu_{59.32}Zr_{40.68}$	1.0E-6
$Cu_{10}Zr_{7}$	2.5E-6
$Cu_{58.32}Zr_{41.68}$	1.9E-6
$Cu_{51.5}Zr_{48.5}$	7.5E-5
$Cu_{51}Zr_{49}$	3.6E-4
$Cu_{49}Zr_{51}$	2.0E-4
$Cu_{34.33}Zr_{65.67}$	0.1
$CuZr_2$	1.4
$Cu_{31.33}Zr_{68.67}$	0.4

The glass formation near $Cu_{51}Zr_{14}$, Cu_8Zr_3, $Cu_{10}Zr_7$ and $CuZr_2$ intermetallics is systematically studied. The so called intermetallic glass phenomenon of two optimum glass formers formed near but separated by the intermetallic phase was confirmed, as similar to the previous results of the formation of intermetallic glass near CuZr intermetallic. Furthermore, a new method was proposed to predict the glass formation ranges of intermetallic glasses. A pair of intermetallic glass formation ranges with local minimum crystallization

driving force was located. Kinetically, through construction of the TTT curves, it reveals that the intermetallic glass formers always have lower critical cooling rate than the corresponding intermetallic compound. Based on both thermodynamic and kinetic consideration, some unique characters of intermetallic glasses were summarized as following:

(1) The intermetallic glasses present in pair but separated by intermetallic compounds. This was explained by our hypothetical Gibbs free energy curves: due to the different rising rates of the Gibbs free energy of liquid and intermetallic phases at compositions near intermetallic compound, the liquid phase has a lower Gibbs free energy. Thus two separated thermodynamically favored glass formation ranges can be located when the formation of primary phases next to the corresponding intermetallic would be kinetic suppressed under quenching.

(2) Furthermore, the intermetallic glasses are sharply composition dependent, which are close to the intermetallic compounds. Thermodynamically, this is consistent with the narrow composition ranges covered by the Gibbs free energy curve of intermetallic phase. Moreover, if the compositions are too far away from the intermetallic compound, the formation of the neighbor primary phases become

kinetically feasible thus the two thermodynamically favored composition ranges would not exist.

(3) Due to the kinetic constraint, the only crystalline phase competing with the amorphous phase during the precipitation is the corresponding intermetallic phase. For example, the glass formation of compositions close enough to $CuZr_2$ interemtallic would not be influenced by the nearby phases CuZr interemetallic and pure Zr under quenching. Thus no other primary phase would be precipitation during the cooling. This has been proved by the results of XRD and the observation optical microscope.

(4) Surprisingly, the phenomenon that the critical cooling rates were also sharply composition dependant near intermetallic compound is discovered. The optimum intermetallic glass formers show different temperature dependent viscosity and R_c from those of the corresponding intermetallic compound. This may provide a kinetic evidence of formation of intermetallic glass.

There is no question that the intermetallic glass is a new family of glass and it provides a new perspective for the future research. There are still some questions needed to be investigated. Firstly, the structure of intermetallic glass is still a mystery. There are several atomic model had been proposed about the

structure of metallic glass, however, none of these models can explain the phenomenon of intermetallic glass [140-144]. The challenge is a pair of optimum glass formers located near but separated by the intermetallic compound, the glass forming ability changes a lot in such narrow composition range. Secondly, it is proved that the intermetallic glass can be located not only near the equiatomic intermtallic like CuZr intermetallic but also near non-equiatomic intermtallics, which indicates that intermetallic glass can be located in a wide composition range in the phase diagram. However, all the intermetallics studied so far are so called line compounds, which have no solubility at all. It is open to question that whether the phenomenon of interemtallic glass exists in the intermetallic with solubility or not. Thirdly, as demonstrated above, the temperature dependent viscosities of the intermetallic glass formers and the intermetallic compounds show different trends, and it causes that the critical cooling rate changes quickly in a narrow composition range near interemtallic compound. The underlying mechanism of the sharply changing critical cooling rate needs further investigation.

3.4 Conclusion

Glass formation around the $Cu_{51}Zr_{14}$, Cu_8Zr_3, $Cu_{10}Zr_7$ and $CuZr_2$ intermetallic compounds has been carefully studied. The formation of interemetallic glass has been explained from both thermodynamic and kinetic perspectives. Here are the conclusions:

(1) Two optimum intermetallic glass formers can be easily located near but separated by almost every intermetallic compound in the Cu-Zr binary system. The result shows that maximum critical thickness of intermetallic glass formed near $Cu_{10}Zr_7$ intermetallic is 520 μm, followed by 470 μm near $CuZr_2$ intermetallic and less than 15 μm near $Cu_{51}Zr_{14}$ intermetallic. However, due to Cu_8Zr_3 intermetallic is a peritectic phase, there is only one optimum glass forming range near Cu_8Zr_3 intermetallic.

(2) The Gibbs free energy as a function of composition of liquid and intermetallic phases is calculated by CALPHAD method at different temperatures. An explanation has been provided that two thermodynamically favored glass forming ranges are present due to the liquid phase has a lower Gibbs free energy under quenching.

(3) The temperature dependent viscosities of the selected compositions are studied. Furthermore, the TTT curves and the critical cooling rates of these selected compositions are calculated, and they are related to the experimental determined critical sizes: two optimum glass formers show lower critical cooling rates or larger critical thickness than those of the corresponding intermetallic compound.

Chapter 4

The formation of intermetallic glasses in Zr–Cu-Ti system

4.1 Introduction

The Zr-Cu-Ti ternary alloy system has attracted increasing interest due to the good glass forming ability and the superior mechanical property [99, 145-151]. Lin et al. indicated that $Ti_{35}Zr_{10}Cu_{55}$ can form metallic glass with critical thickness of 500 μm; and the critical cooling rate was calculated as 2×10^4 K/s [97]. Inoue et al. studied the glass formation of $Cu_{60}Zr_{40-x}Ti_x$, where x= 0-40 at% [101]. $Cu_{60}Zr_{30}Ti_{10}$ was the best glass former with 4 mm glass forming ability. More recently, a new glass forming range was reported

around composition $Cu_{52}Zr_{40}Ti_8$, the critical size was determined as 4 mm [103]. In this chapter, two new composition ranges ((1) $Cu_{100-x}(ZrTi)_x$, where Ti=5% and x=47.5-53; (2) compositions around Cu_2ZrTi intermetellic) are selected to study the phenomenon of formation of intermetallic glass and the glass forming ability.

It is commonly believed that when more elements are involved in the alloy system, the alloy should become too confused to have chance of crystallization under quenching [41]: elements with different radiuses can lead to dense packing structure in the liquid state, therefore glass formation should be favored than crystallization kinetically. Therefore, element addition is a very effective way to improve the glass forming ability or to develop new BMGs systems [66, 152-158]. In the first composition range studied in this chapter ($Cu_{100-x}(ZrTi)_x$, where Ti=5% and x=47.5-53), titanium can be considered as a third additional element. Although Zr-Cu binary system is the one of best glass formation binary systems, 2 mm critical size is still too small for the engineering application. Ti has an atomic radius between Zr and Cu, which may increase the dense packing in the liquid state. Also, the heat of mixing between Ti and Cu is negative as -9 kJ/mol, which may help to the glass formation [9, 64, 159]. Furthermore, from the Cu-Ti binary phase diagram, it shows TiCu phase is also an intermetallic phase (as shown in **Figure 4.1**). Therefore, the Zr-Ti-Cu system would be a good choice to obtain a

good glass forming ability and also to further study the formation of intermetallic glass in ternary system.

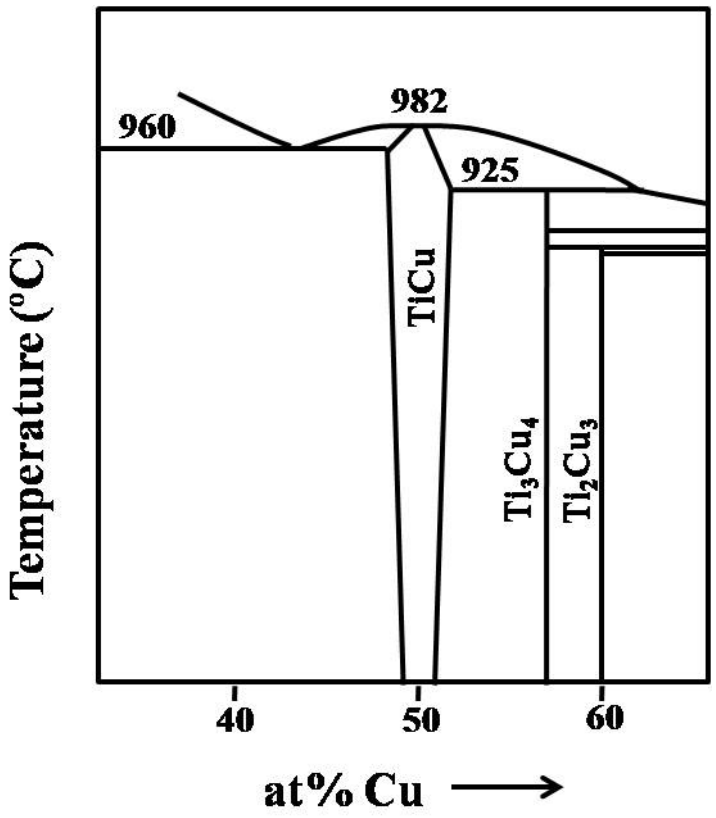

Figure 4.1 Part of Ti-Cu binary phase diagram.

The second composition range to be studied is around the Cu_2ZrTi intermetallic, which is a Laves phase. It has been reported that this Cu_2ZrTi phase covered a wide composition range at high temperature (more than 10 at%) [119, 160, 161]. The wide Laves phase homogeneity range suggests that the Gibbs free energy varies slowly with the changing of composition and the liquidus lines are relatively flat with respect to compositions. In this sense, the Laves phase is "forgiving" of composition variation. Moreover, it is believed

that when the composition of the liquid phase is very different from that of the competing crystalline phase, the nucleation would be difficult for the crystalline phase due to the fact that composition required may not be satisfied through diffusion in the undercooling liquid. All of these suggest that crystallization of the Laves phase may occur more easily than the formation of amorphous phase in this Laves phase composition range [97]. Therefore, all the reported investigations about glass forming ability in this Zr-Ti-Cu ternary system focus on the compositions away from Laves phase, and there is no report about the glass forming ability in the Laves phase composition range before. At the meantime, there was also some work treated Cu_2ZrTi phase as a stoichiometric compound, because there was no solubility of the Cu_2ZrTi phase at low temperature reported [100]. In this chapter, the glass forming ability around the Cu_2ZrTi ternary intermetallic phase would be studied.

Figure 4.2 shows the composition ranges studied in this chapter. For the first composition range, 5 at% Ti would be added into Zr-Cu system. Ti was demonstrated to stabilize the $Cu_{10}Zr_7$ phase but there are still two optimum glass formers separated by the center composition. Cu_2ZrTi phase was found cover a wide composition range, and the phenomenon of formation of intermetallic glass was not clear in this area.

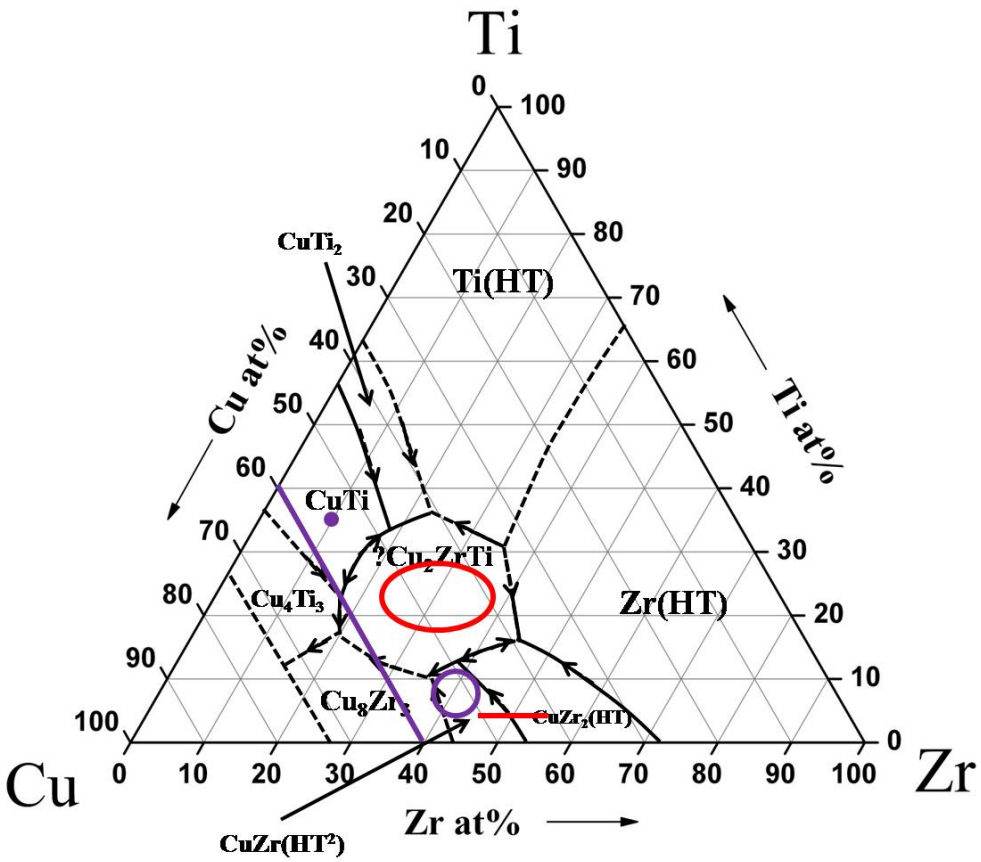

Figure 4.2 The composition ranges studied in this chapter (marked by the red line and the red circle) and the composition ranges studied before (marked by the purple line and the pruple circle) [97, 101-103].

4.2 Glass formation of compositions $Cu_{100-x}(ZrTi)_x$ (Ti=5 at% and x=47.5-53)

CuZr intermetallic was selected to investigate the influence of Ti addition on the formation of intermetallic glass. Based on the fact that a pair of optimum glass formers ($Cu_{51.5}Zr_{48.5}$ and $Cu_{49}Zr_{51}$) are located near but separated by CuZr intermetallic [81], 5 at% Ti was added to replace Zr from composition

$Cu_{52.5}Zr_{47.5}$ to $Cu_{47}Zr_{53}$. Two kinds of rods were cast with diameter in 3 mm and 5 mm, respectively.

4.2.1 Glass formation of 3 mm rods of alloy $Cu_{100-x}(ZrTi)_x$ (Ti=5 at% and x=47.5-53)

Figure 4.3 shows the SEM photos of the longitudinal view of 3 mm rods with compositions from $Cu_{52.5}(ZrTi)_{47.5}$ to $Cu_{47}(ZrTi)_{53}$. The dark contras parts are amorphous phase and the light contrast parts are the crystalline phase. Two crystalline phases can be observed in these 3 mm rods: CuZr phase and $Cu_{10}Zr_7$ phase, whose morphologies are shown in **Figure 4.4**, respectively. The CuZr phase can be easily observed even under low magnification, while the $Cu_{10}Zr_7$ phase is much "smaller" in the size and only can be observed under high magnification. According to the (ZrTi) content, the whole composition range can be divided into five regions with different amount of crystalline phase: (1) For the starting composition $Cu_{52.5}(ZrTi)_{47.5}$, there is clearly large amount of crystalline phase scattered in the amorphous matrix. Although the light contrast parts are not obvious in the SEM photos of $Cu_{52}(ZrTi)_{48}$, large amount of $Cu_{10}Zr_7$ phase (as shown in **Figure 4.4(b)**) can be observed under high magnification. (2) When the composition reaches $Cu_{51.5}(ZrTi)_{48.5}$, the 3 mm rod shows as-cast structure with > 90% amount of amorphous phase.

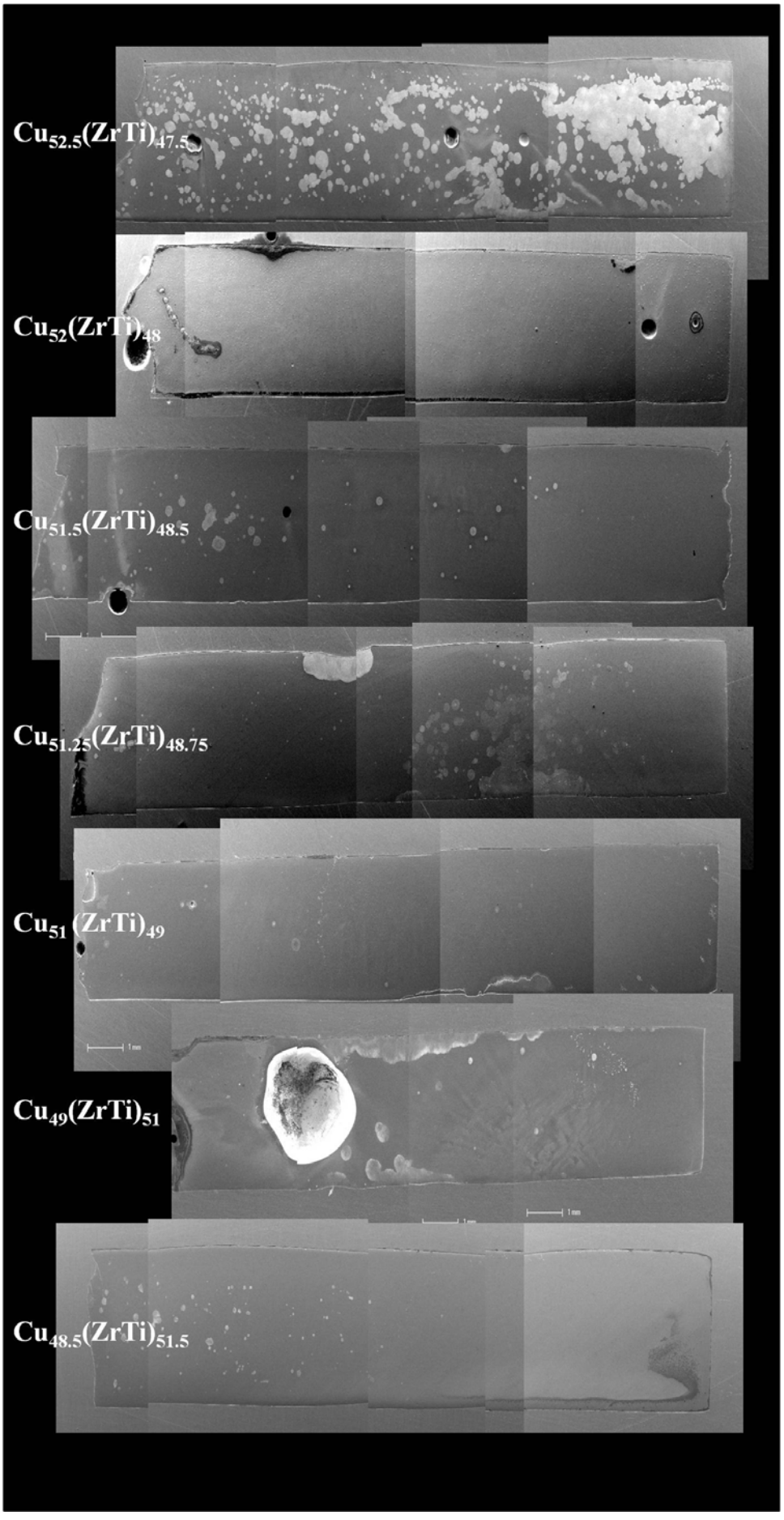
$Cu_{52.5}(ZrTi)_{47.5}$
$Cu_{52}(ZrTi)_{48}$
$Cu_{51.5}(ZrTi)_{48.5}$
$Cu_{51.25}(ZrTi)_{48.75}$
$Cu_{51}(ZrTi)_{49}$
$Cu_{49}(ZrTi)_{51}$
$Cu_{48.5}(ZrTi)_{51.5}$

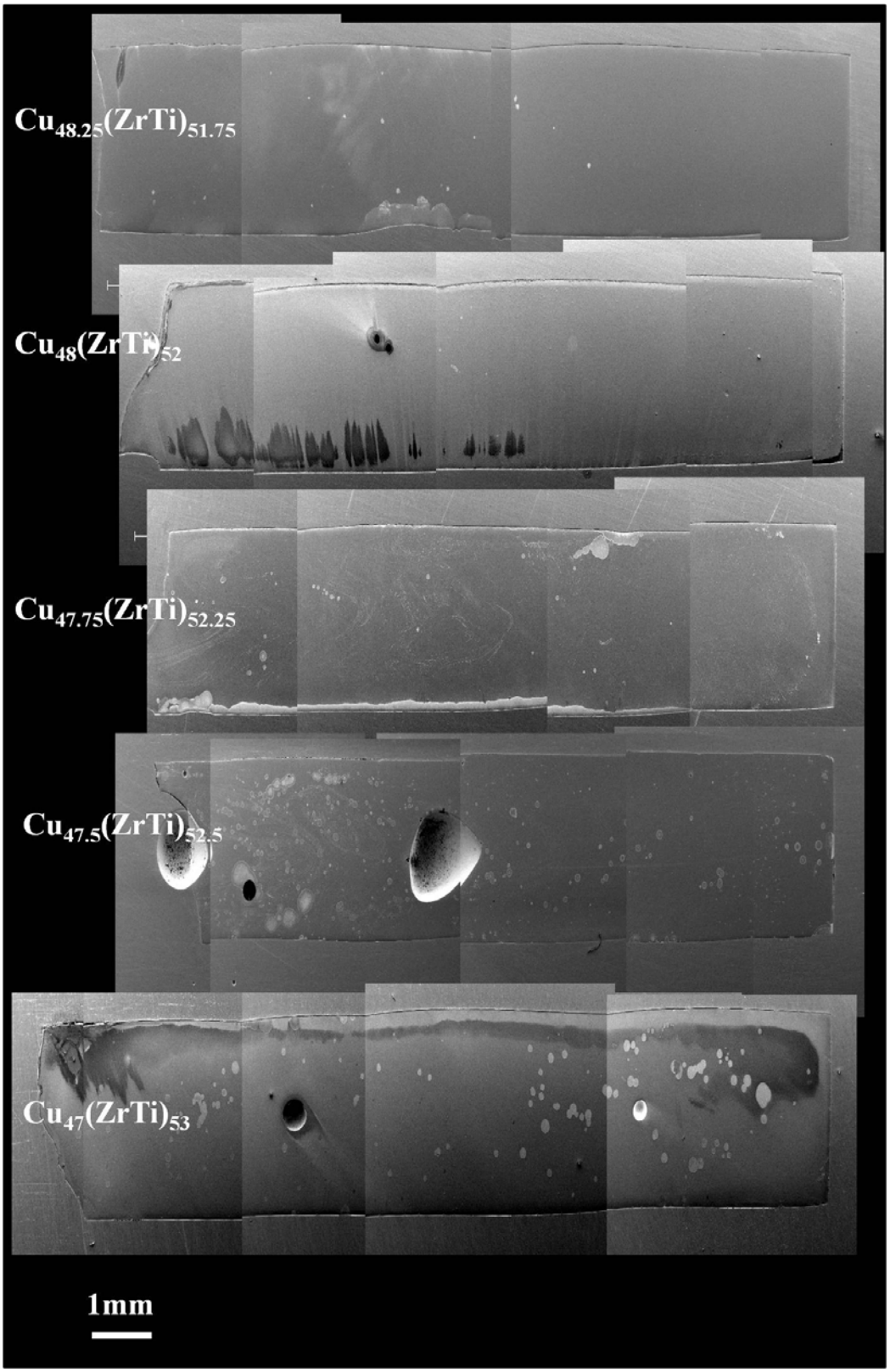

Figure 4.3 SEM photos of the longitudinal view of 3 mm rods with composition from $Cu_{52.5}(ZrTi)_{47.5}$ to $Cu_{47}(ZrTi)_{53}$.

(3) The amount of amorphous phase decreases with the further increase (ZrTi) content to $Cu_{51.25}(ZrTi)_{48.75}$ and $Cu_{51}(ZrTi)_{49}$. (4) Within the composition range from $Cu_{49}(ZrTi)_{51}$ to $Cu_{47.75}(ZrTi)_{52.25}$, all the 3 mm rods contain large amount of amorphous phase, while $Cu_{48}(ZrTi)_{52}$ show fully amorphous structure. (5) The amount of crystalline phase becomes more (than the previous region) when the composition reaches $Cu_{47.5}(ZrTi)_{52.5}$ and $Cu_{47}(ZrTi)_{53}$. It shows that two optimum glass forming ranges (regions (2) and (4)) are located near but separated by region (3). This result is in good agreement with the glass forming ranges near CuZr intermetallic: two optimum glass formers $Cu_{51.5}Zr_{48.5}$ and $Cu_{49}Zr_{51}$ were separated by CuZr intermetallic.

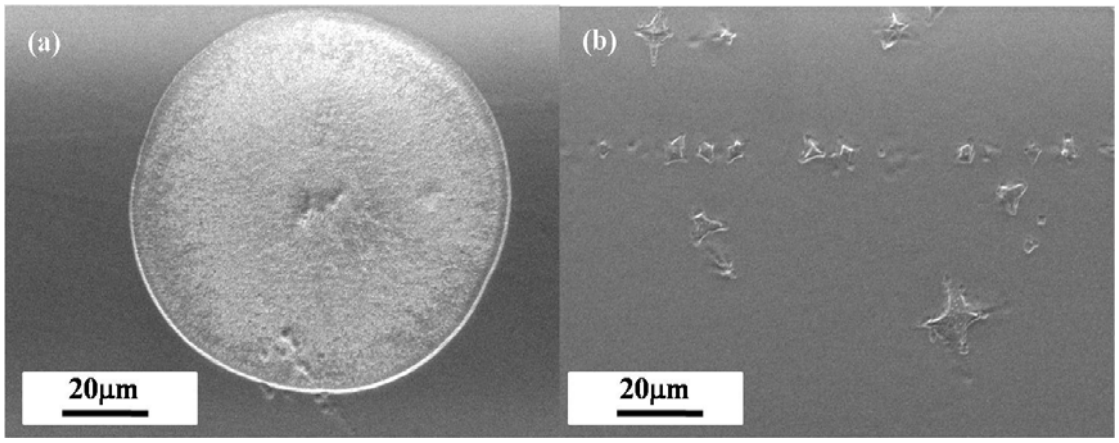

Figure 4.4 SEM photos of two kinds of crystalline phases detected in the 3 mm rods with composition from $Cu_{52.5}(ZrTi)_{47.5}$ to $Cu_{47}(ZrTi)_{53}$: (a) CuZr phase and (b) Cu10Zr7 phase.

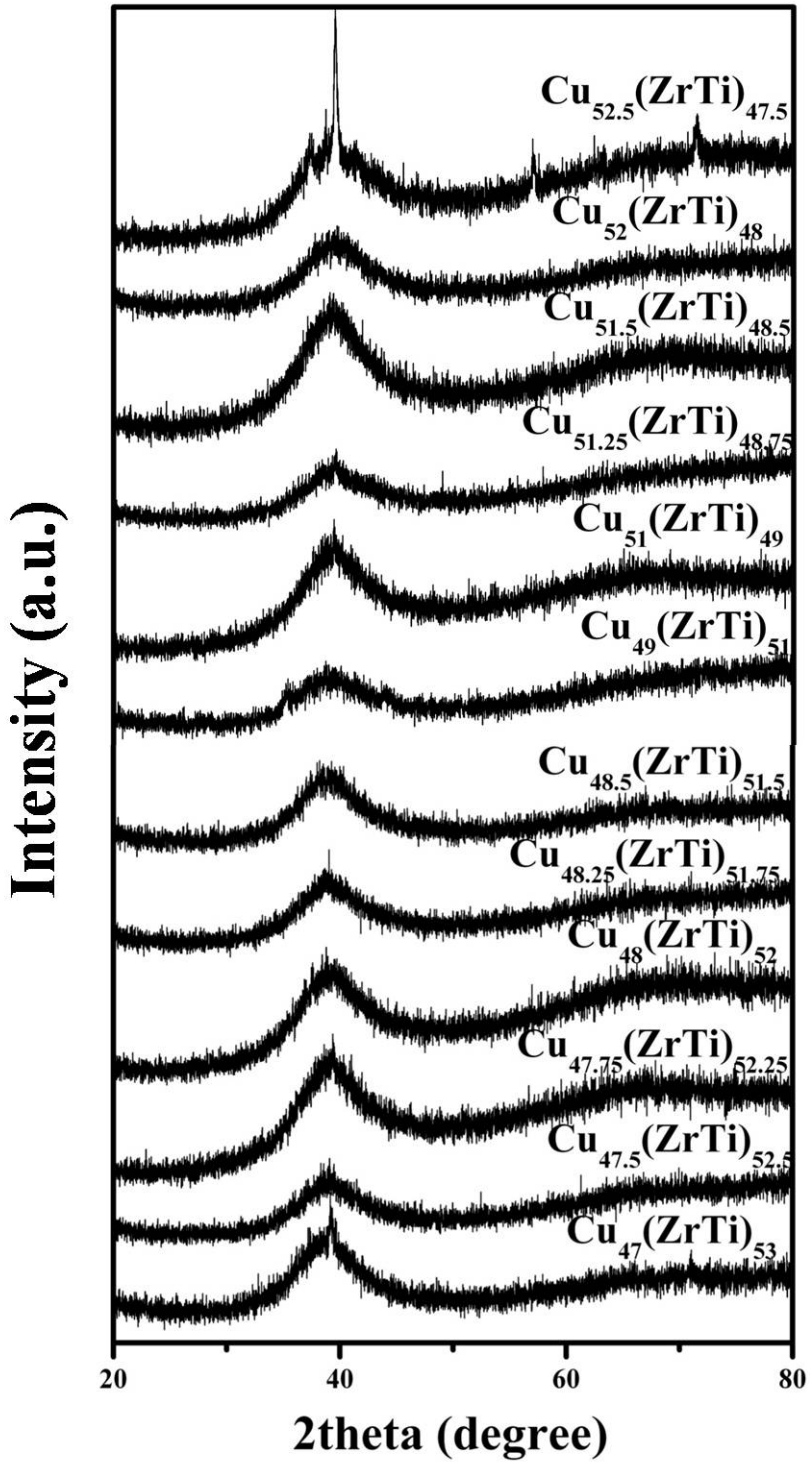

Figure 4.5 XRD patterns of 3 mm rods with composition from $Cu_{52.5}(ZrTi)_{47.5}$ to $Cu_{47}(ZrTi)_{53}$.

The XRD patterns of the cross-section of all the 3 mm rods are shown in **Figure 4.5**. Only $Cu_{52.5}(ZrTi)_{47.5}$ shows clearly diffraction peaks of crystalline

phases. All the others show either a board amorphous hump or some tiny peaks of crystalline phase on it. This may be caused by that the amount of crystalline phases in these 3 mm rods is small (the morphology of $Cu_{10}Zr_7$ phase is "small"). Therefore, the area covered by the crystalline phases is not big enough to be detected as only $Cu_{52.5}(ZrTi)_{47.5}$ contains large amount of crystalline phase among all these compositions.

The corresponding DSC curves of these 3 mm rods are shown in **Figure 4.6** to further confirm the observation of the SEM photos and the XRD results. The enthalpies of crystallization were used to estimate the amount of the amorphous phase, as plotted in **Figure 4.7**. $Cu_{51.5}(ZrTi)_{48.5}$ and $Cu_{48}(ZrTi)_{52}$ have 71.8 J/g and 79.3 J/g of enthalpies of crystallization respectively, which are the highest two values among their neighbor compositions. Composition $Cu_{48}(ZrTi)_{52}$ has the highest enthalpy of crystallization among all the composition, and moreover, there is no crystalline phase observed from both XRD and SEM results. Thus $Cu_{48}(ZrTi)_{52}$ is believed as a fully amorphous structure. According to the resulting enthalpies of crystallization, the percentage of the amorphous phase in each rod can be easily calculated and plotted in **Figure 4.7**. The DSC results confirm that there are two optimum glass formers separated by the composition of $Cu_{51.25}(ZrTi)_{48.75}$, which is consistent with the character of intermetallic glass. It is also noticed that the

glass transition temperature T_g and the onset crystallization temperature T_x shift to lower temperature with the increasing (ZrTi) content. The crystallization peaks split from on peak into two peaks at high (ZrTi) composition side, which suggests that new crystalline phase precipitates. This indicates the end of the intermetallic glass formation zone, as it is proposed that the crystalline phases (competing with the amorphous) during cooling would not change in the interemtallic glass formation range.

Therefore, the SEM and DSC results show the phenomenon of formation of intermetallic glass in the studied composition range ($Cu_{100-x}(ZrTi)_x$ (x=47.5-53)). However, the XRD results are not convincing enough as almost all compositions seem like “fully” amorphous.

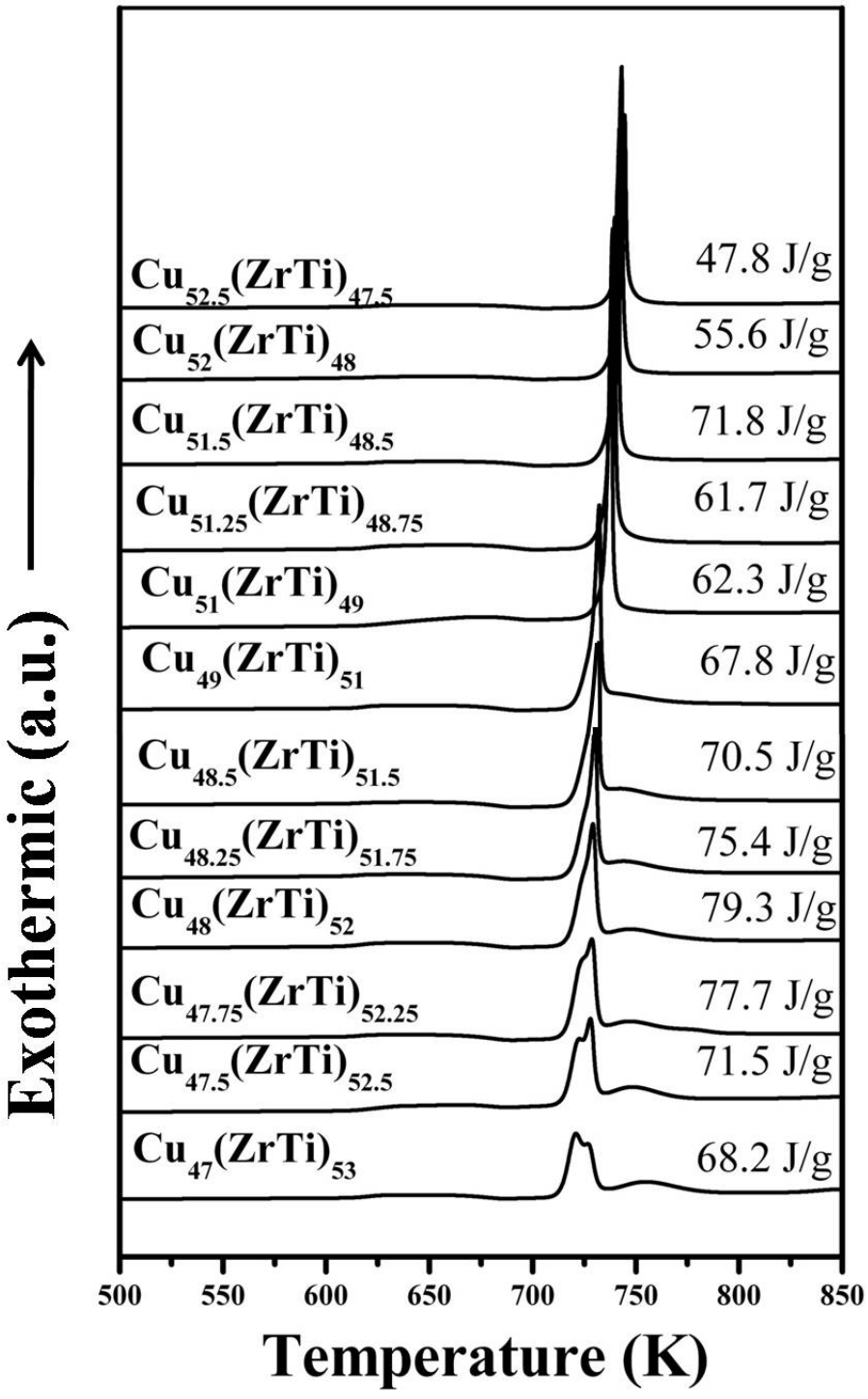

Figure 4.6 DSC curves of 3 mm rods with composition from $Cu_{52.5}(ZrTi)_{47.5}$ to $Cu_{47}(ZrTi)_{53}$.

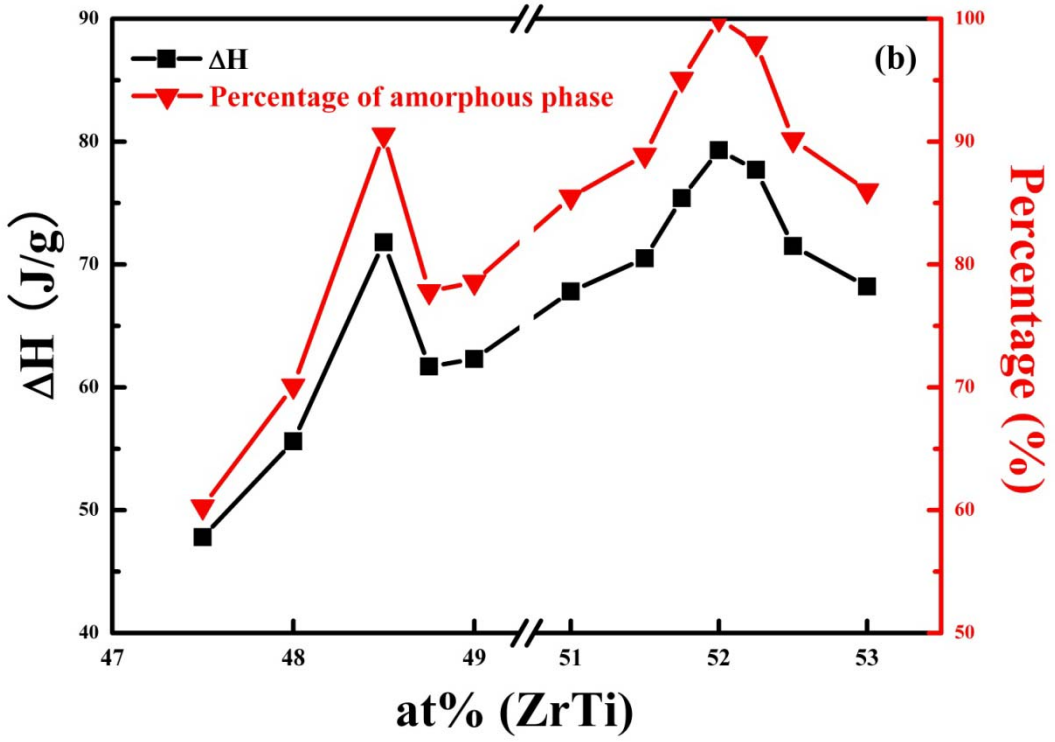

Figure 4.7 Calculated enthalpies of crystallization and percentage of amorphous phase of all 3 mm rods.

4.2.2 Glass formation of 5 mm rods of alloy $Cu_{100-x}(ZrTi)_x$ (x=47.5-53)

In the same composition range as $Cu_{100-x}(ZrTi)_x$ (x=47.5-53), 5 mm rods were cast to further investigate the glass forming ability and to confirm the phenomenon of formation of intermetallic glass obtained through 3 mm rods. **Figure 4.8** shows the SEM photos of the longitudinal view of the 5 mm rods. Unfortunately, there is no fully amorphous structure observed. Therefore, the optimum glass former is defined as the composition containing the largest amount of amorphous phase among the compositions around it. The studied

composition range also can be divided into five regions: (1) Compositions $Cu_{52.5}(ZrTi)_{47.5}$ and $Cu_{52}(ZrTi)_{48}$ show almost fully crystalline structure. (2) $Cu_{51.5}(ZrTi)_{48.5}$ shows the largest area covered by amorphous phase among its neighbor composition, which suggests that it is an optimum glass former. (3) Composition $Cu_{51}(ZrTi)_{49}$ has structure of almost fully crystalline phase. (4) With the further increase (ZrTi) content, all compositions from $Cu_{49}(ZrTi)_{51}$ to $Cu_{48}(ZrTi)_{52}$ show structure of crystalline phases embedded in the amorphous matrix. $Cu_{48}(ZrTi)_{52}$ is considered as the optimum glass former among them as it has the largest amount of amorphous phase. (5) The amount of crystalline phase keeps increasing from $Cu_{47.75}(ZrTi)_{52.25}$ to $Cu_{47}(ZrTi)_{53}$ and finally ends with structure of fully crystalline phase. These five composition ranges are consistent with those obtained through 3 mm rods, and two optimum glass formers ($Cu_{51.5}(ZrTi)_{48.5}$ and $Cu_{48}(ZrTi)_{52}$) are located near but separated by the composition of $Cu_{51}(ZrTi)_{49}$. There are also two kinds of phases can be observed in all the rods: CuZr phase and $Cu_{10}Zr_7$ phase.

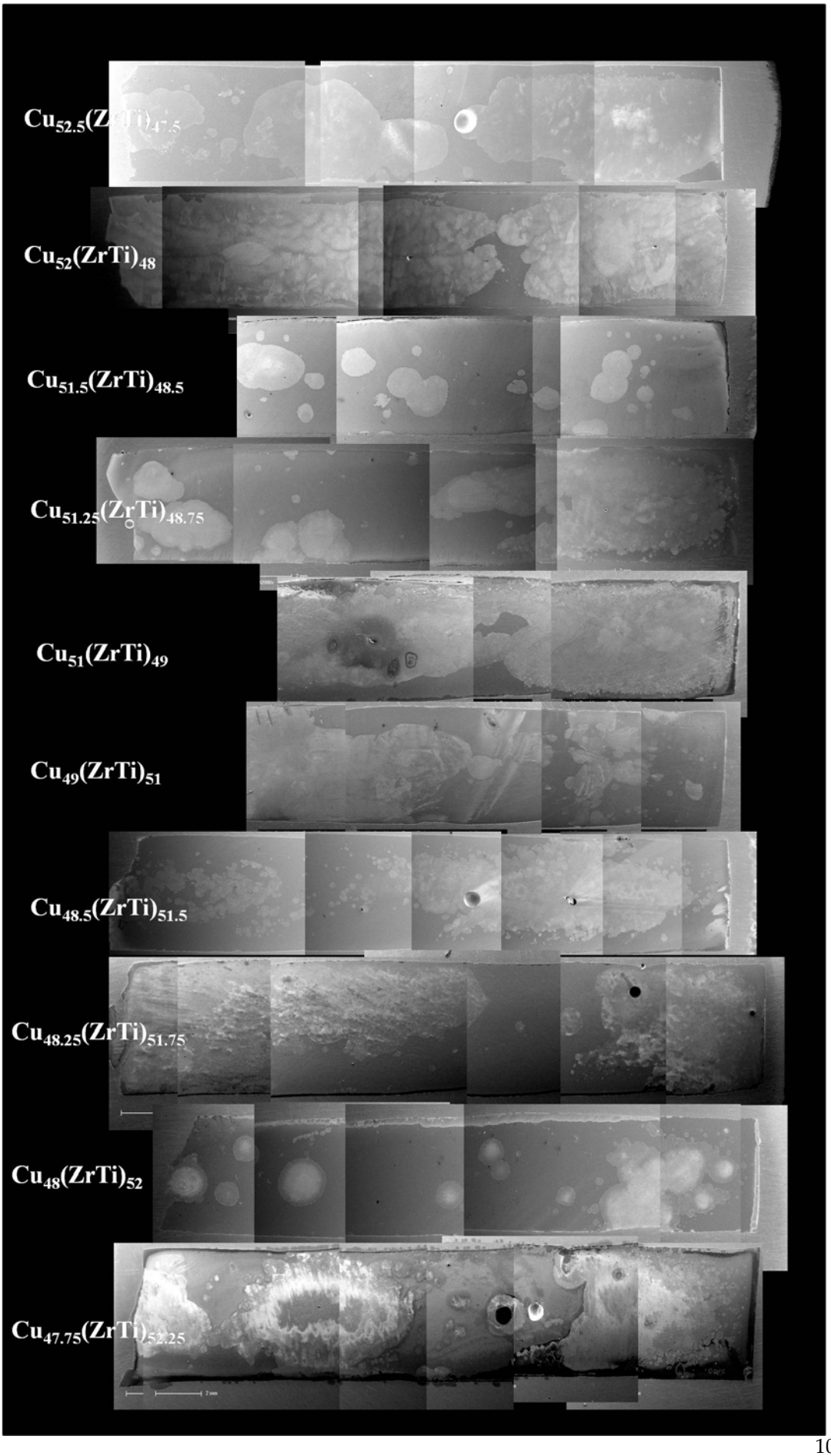
$Cu_{52.5}(ZrTi)_{47.5}$
$Cu_{52}(ZrTi)_{48}$
$Cu_{51.5}(ZrTi)_{48.5}$
$Cu_{51.25}(ZrTi)_{48.75}$
$Cu_{51}(ZrTi)_{49}$
$Cu_{49}(ZrTi)_{51}$
$Cu_{48.5}(ZrTi)_{51.5}$
$Cu_{48.25}(ZrTi)_{51.75}$
$Cu_{48}(ZrTi)_{52}$
$Cu_{47.75}(ZrTi)_{52.25}$

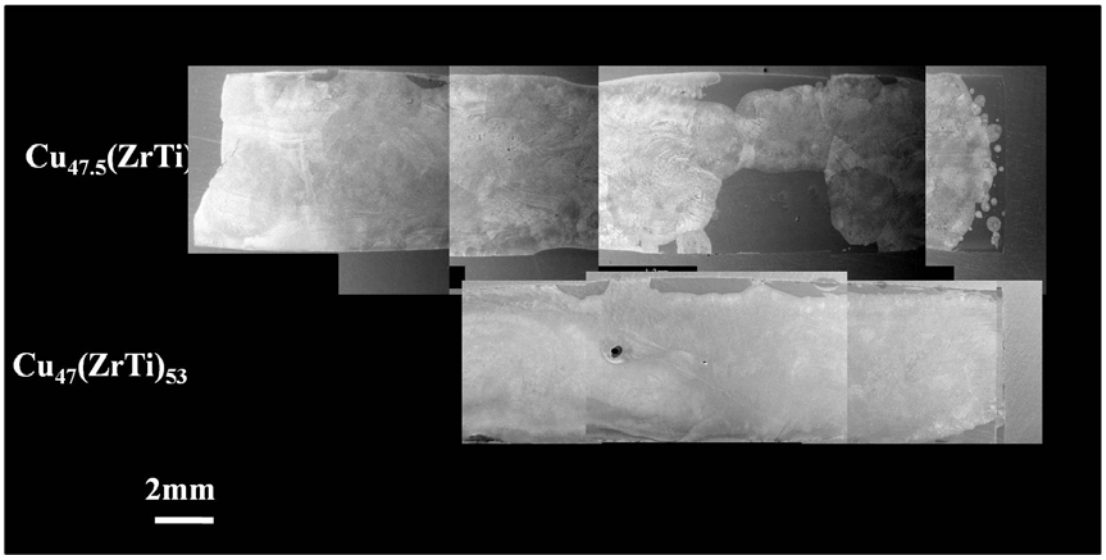

Figure 4.8 SEM photos of longitudinal view of 5 mm rods with composition from $Cu_{52.5}(ZrTi)_{47.5}$ to $Cu_{47}(ZrTi)_{53}$.

DSC studied is also carried out to confirm the observation obtained from the SEM photos and the results are shown in **Figure 4.9** along with the calculated enthalpies of crystallization. The enthalpies of crystallization of $Cu_{51.5}(ZrTi)_{48.5}$ and $Cu_{48}(ZrTi)_{52}$ are 52.7 J/g and 69.1 J/g respectively, which are highest value among their neighbor compositions. Compositions from $Cu_{49}(ZrTi)_{51}$ to $Cu_{48.25}(ZrTi)_{51.75}$ also have relatively high values of enthalpies of crystallization, which suggest the presence of quite amount of amorphous phase. The DSC results are almost consistent with the observation obtained from SEM photos and confirm the phenomenon of formation of intermetallic glass. The only exception is $Cu_{48.25}(ZrTi)_{51.75}$; its enthalpy of crystallization is much lower than those of compositions around it. However, it should be noticed that the value of enthalpy of crystallization would be highly dependent on the selected position (on the 5 mm rods) measured by DSC. Therefore, the DSC results can

only imply the amount of amorphous phase in this 5 mm case.

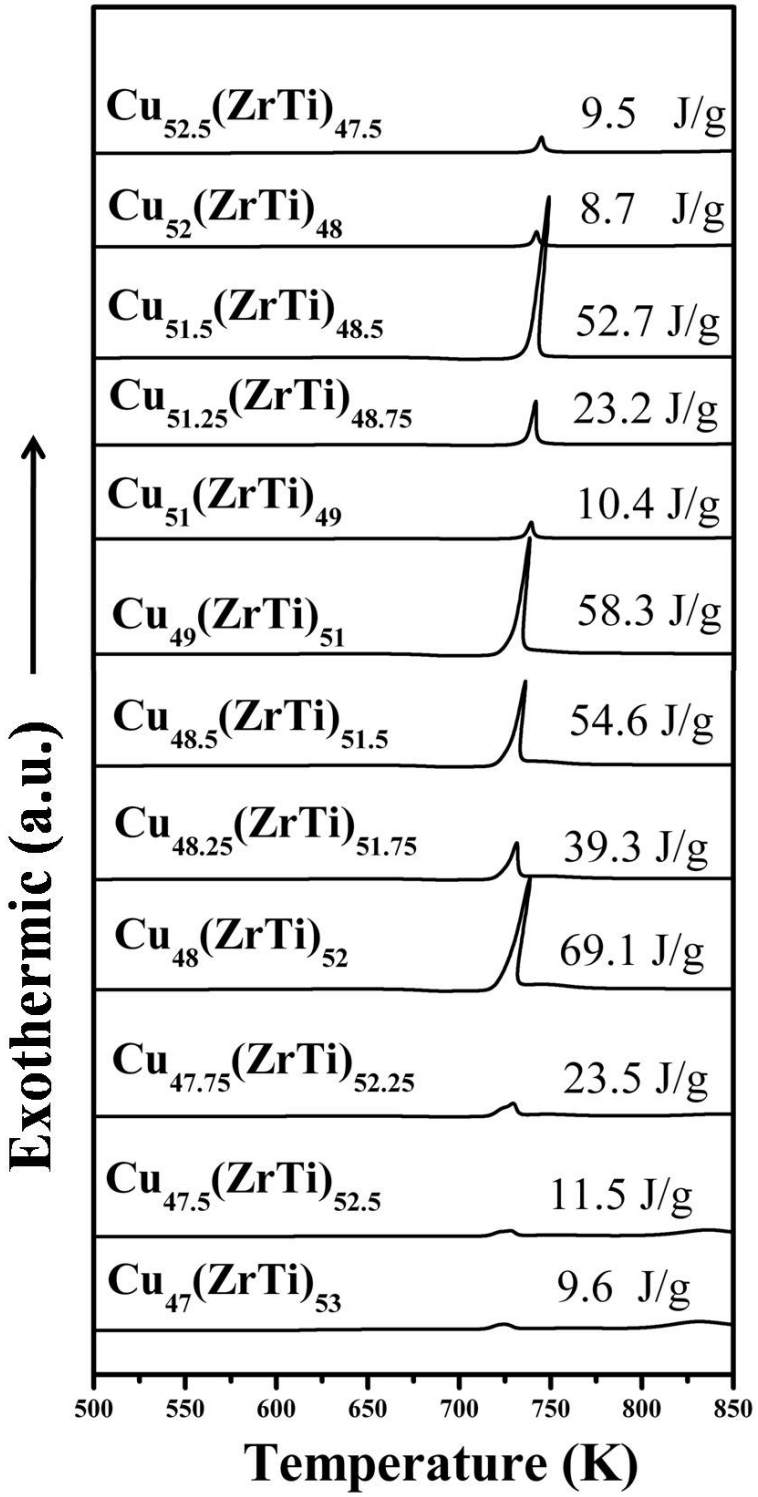

Figure 4.9 DSC curves of 3 mm rods with composition from $Cu_{52.5}(ZrTi)_{47.5}$ to $Cu_{47}(ZrTi)_{53}$.

Based on the experimental results of both 3 mm and 5 mm rods with compositions from $Cu_{52.5}(ZrTi)_{47.5}$ to $Cu_{47}(ZrTi)_{53}$, the glass formation of this composition range can be summarized as following:

(1) The phenomenon of intermetallic glass, two optimum glass formers located near but separated by the intermetallic phase, can be confirmed. However, with the addition of 5 at% Ti, two kinds of intermetallic phases precipitated in both 3 mm and 5 mm rods instead of only one corresponding intermetallic phase can be detected in all the samples in binary system. It should be noticed that there is no crystalline phase containing Ti detected. The precipitated of $Cu_{10}Zr_7$ phase was unexpected due to the composition range was based on the compositions near CuZr intermetallic. More importantly, the $Cu_{10}Zr_7$ phase can still be detected when the composition reaches high (ZrTi) content ((ZrTi) > 50 at%), where should correspond to composition region between CuZr and $CuZr_2$ phases in binary system. Thus the role of Ti addition may not be simply replace Zr but also stabilize the $Cu_{10}Zr_7$ phase.

(2) As mentioned before, two optimum glass formers were located at $Cu_{51.5}Zr_{48.5}$ and $Cu_{49}Zr_{51}$, which are separated by $Cu_{51}Zr_{49}$ with fully crystalline structure in Zr-Cu binary system [81]. With the addition of Ti, the two optimum glass formers in the ternary system, separated by

$Cu_{51}(ZrTi)_{49}$, are located at $Cu_{51.5}(ZrTi)_{48.5}$ and $Cu_{48}(ZrTi)_{52}$. Although composition $Cu_{48}(ZrTi)_{52}$ is slightly different from composition $Cu_{49}Zr_{51}$, the compositions of the two optimum glass formers in ternary system still can be considered as same as those in binary system.

4.3 Glass formation of compositions near Cu_2ZrTi intermetallic phase

Generally, it is believed that the glass formation range should be (1) close to eutectic points, where the value of T_{rg} should be high; (2) away from Laves phase, where the nucleation would occur easily [97]. Previously, the formation of glasses near intermetallic phases has been demonstrated. In this section, the glass formation near Laves phase would be studied.

4.3.1 Glass formation of compositions $Cu_{50}Zr_xTi_{50-x}$, $Cu_yZr_{77-y}Ti_{23}$ and $Cu_yZr_{27}Ti_{73-y}$

Starting with the composition of Cu_2ZrTi ($Cu_{50}Zr_{25}Ti_{25}$), the glass forming ability near it was investigated by studying the critical thickness of the wedge cast samples, and **Figure 4.10** shows the compositions studied.

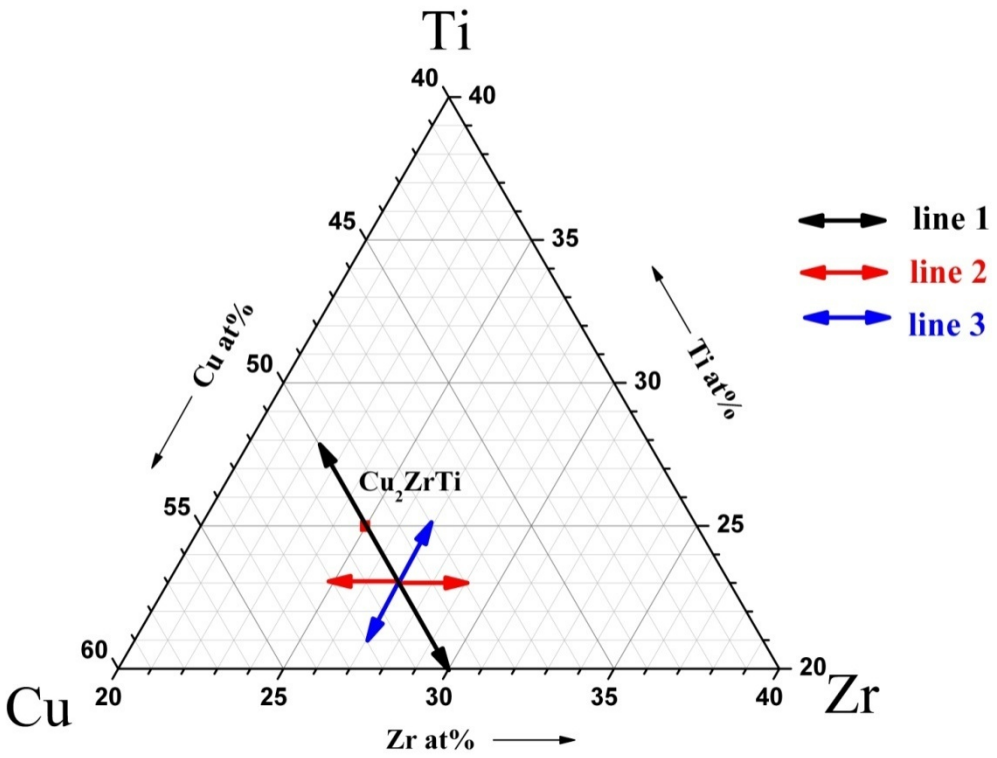

Figure 4.10 The studied compositions near Cu_2ZrTi ($Cu_{50}Zr_{25}Ti_{25}$), marked by the red dot.

The OM photos of the longitudinal view of the wedge samples with the compositions $Cu_{50}Zr_xTi_{50-x}$ (x=22-30) are shown in **Figure 4.11**. The arrows are pointing to the boundaries between the crystalline phase and the amorphous phase, where the critical thicknesses are measured. The critical thicknesses of the wedge samples are plotted in **Figure 4.12**. The results show that the Cu_2ZrTi ($Cu_{50}Zr_{25}Ti_{25}$) has the maxmium critical thickness of 600 μm among these compositions. With the decreasing Zr content, the critical thickness decreases from 600 μm to 400 μm first and then rises to 480 μm, after that the critical thickness keeps decreasing to 300 μm. With the increasing Zr content, the critical thickness changes with no clear trend; the smallest critical

thickness presents at $Cu_{50}Zr_{27}Ti_{23}$ of 320 μm, as pointed by the arrow in **Figure 4.12**. If $Cu_{50}Zr_{27}Ti_{23}$ is considered as the center composition, there are two peaks in critical thickness located at both sides of it although the critical thickness keeps fluctuating. Furthermore, Line 2 ($Cu_yZr_{77-y}Ti_{23}$) and line 3 ($Cu_yZr_{27}Ti_{73-y}$) are extended from $Cu_{50}Zr_{27}Ti_{23}$ since it has the smallest critical thickness.

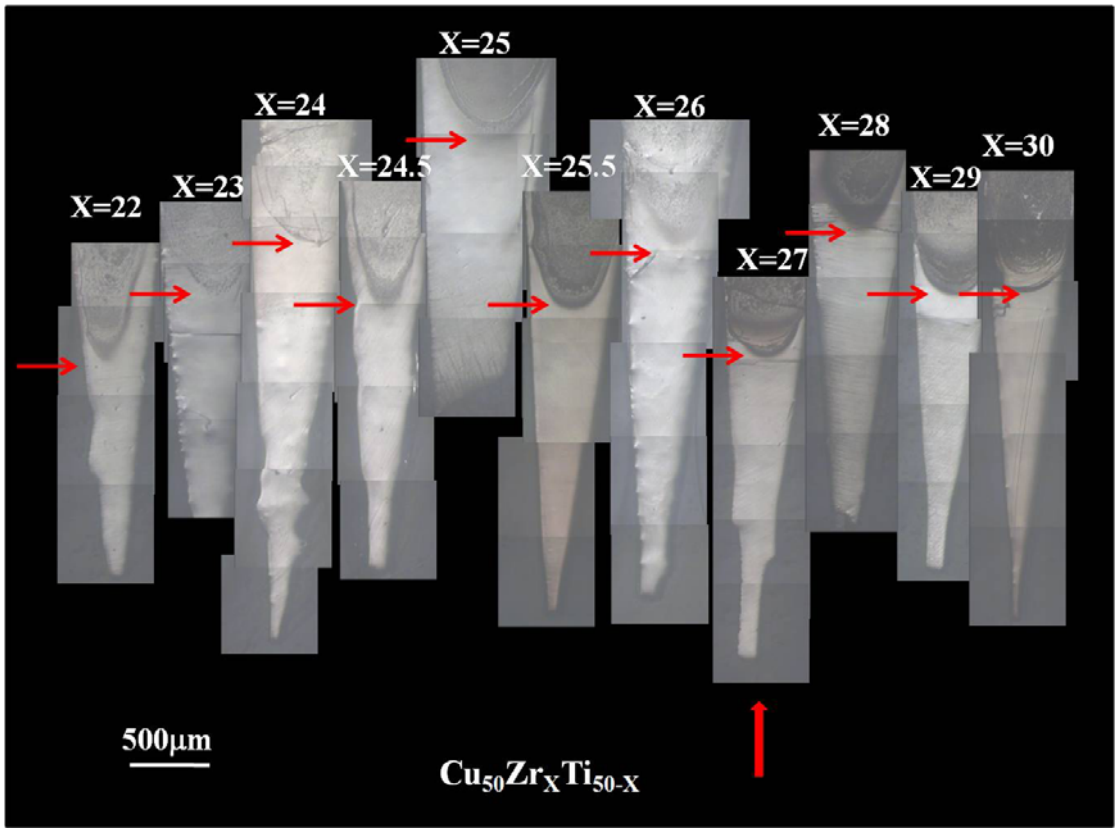

Figure 4.11 OM photos of the longitudinal view of the wedge cast samples of $Cu_{50}Zr_xTi_{50-x}$ (x=22-30).

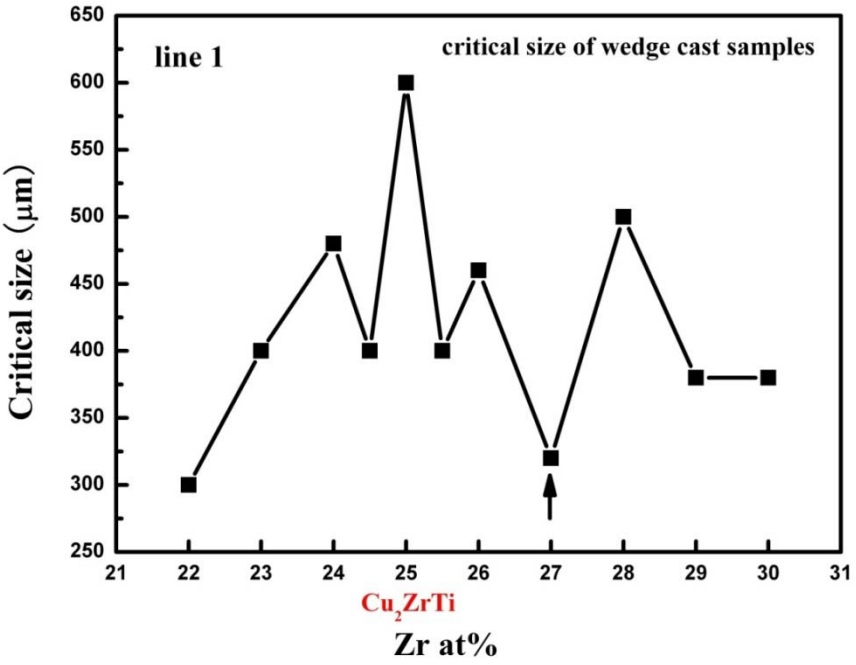

Figure 4.12 The critical sizes of the wedge cast samples of $Cu_{50}Zr_xTi_{50-x}$ (x=22-30).

Figure 4.13 shows the OM photos of the cross-section view of the wedge cast samples with compositions along line 2 ($Cu_yZr_{77-y}Ti_{23}$, y=48-52). The horizontal arrows are pointing to the critical thickness and the vertical arrow indicates the composition of $Cu_{50}Zr_{27}Ti_{23}$, which is the starting composition of line 2. **Figure 4.14** summarizes the critical thicknesses of compositions along line 2. Unlike the fluctuating of the critical thicknesses observed in line 1, it shows that two peaks in the critical thickness (480 μm at $Cu_{51.5}Zr_{25.5}Ti_{23}$ and 400 μm at $Cu_{49.5}Zr_{27.5}Ti_{23}$) are separated by the compositions of $Cu_{50.5}Zr_{26.5}Ti_{23}$ and $Cu_{50}Zr_{27}Ti_{23}$.

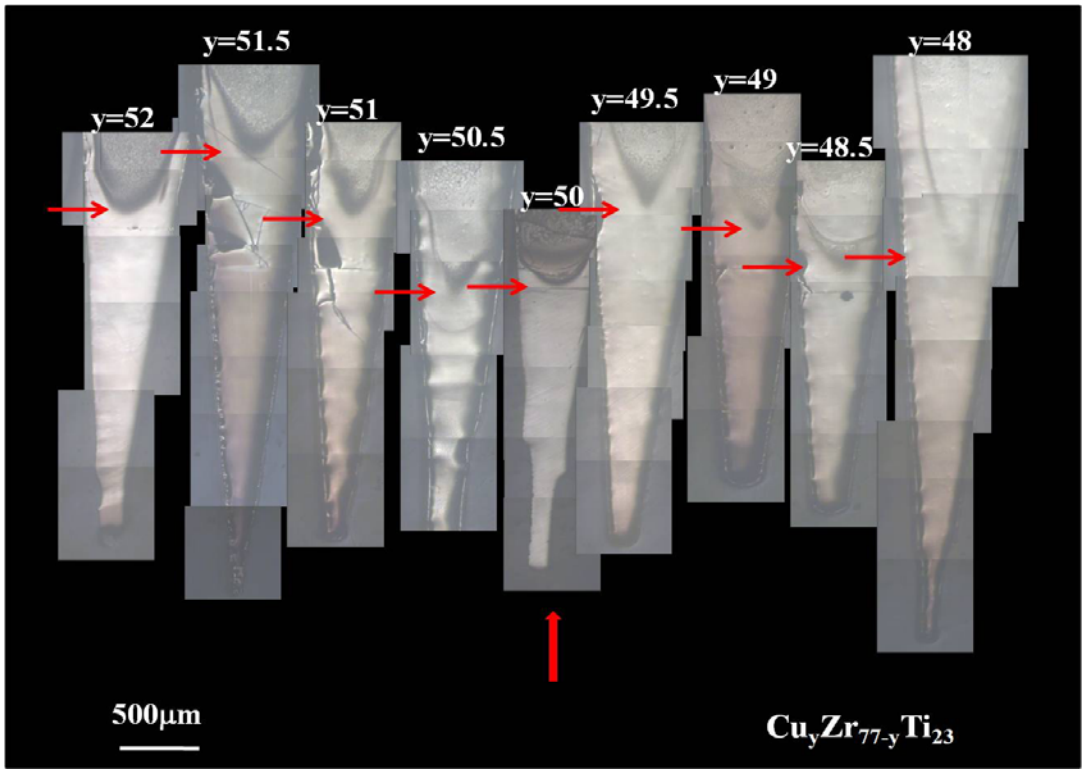

Figure 4.13 OM photos of the longitudinal view of the wedge cast samples of $Cu_yZr_{77-y}Ti_{23}$ (y=48-52).

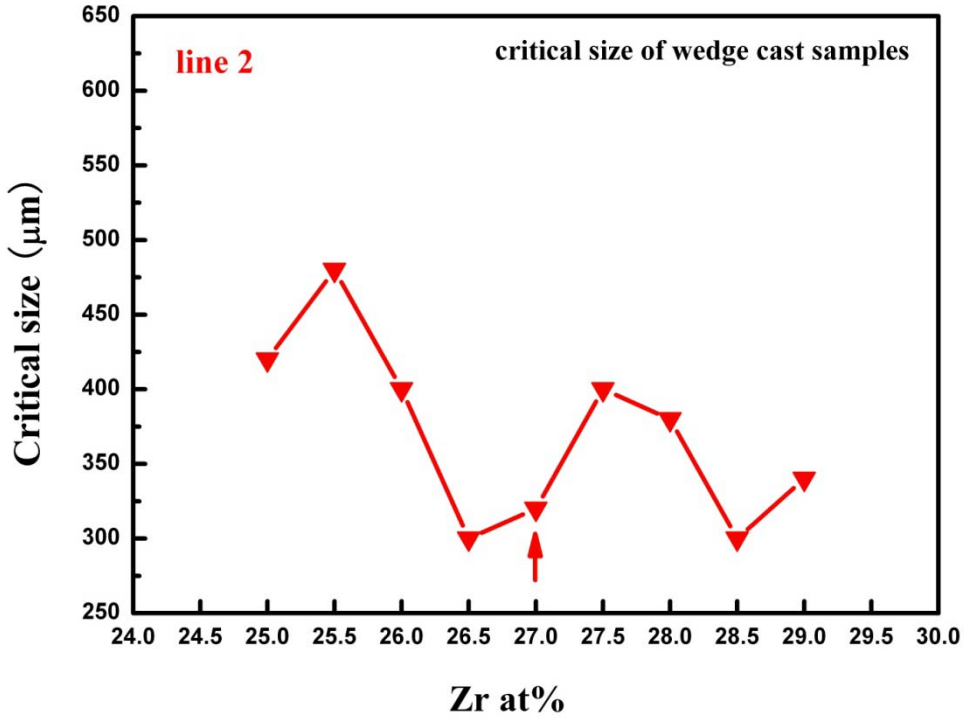

Figure 4.14 The critical sizes of the wedge cast samples of $Cu_yZr_{77-y}Ti_{23}$ (y=48-52).

Figure 4.15 shows the OM photos of the wedge samples with the compositions along line 3 and their critical thicknesses are summarized in **Figure 4.16**. The vertical arrows in both **Figure 4.15** and **Figure 4.16** indicate the composition of $Cu_{50}Zr_{27}Ti_{23}$. The changing of critical thickness has similar trend as that of line 2. Two peaks in critical thickness (480 μm at $Cu_{51.5}Zr_{27}Ti_{21.5}$ and 440μm at $Cu_{49.5}Zr_{27}Ti_{23.5}$) are located at both sides of composition $Cu_{50}Zr_{27}Ti_{23}$.

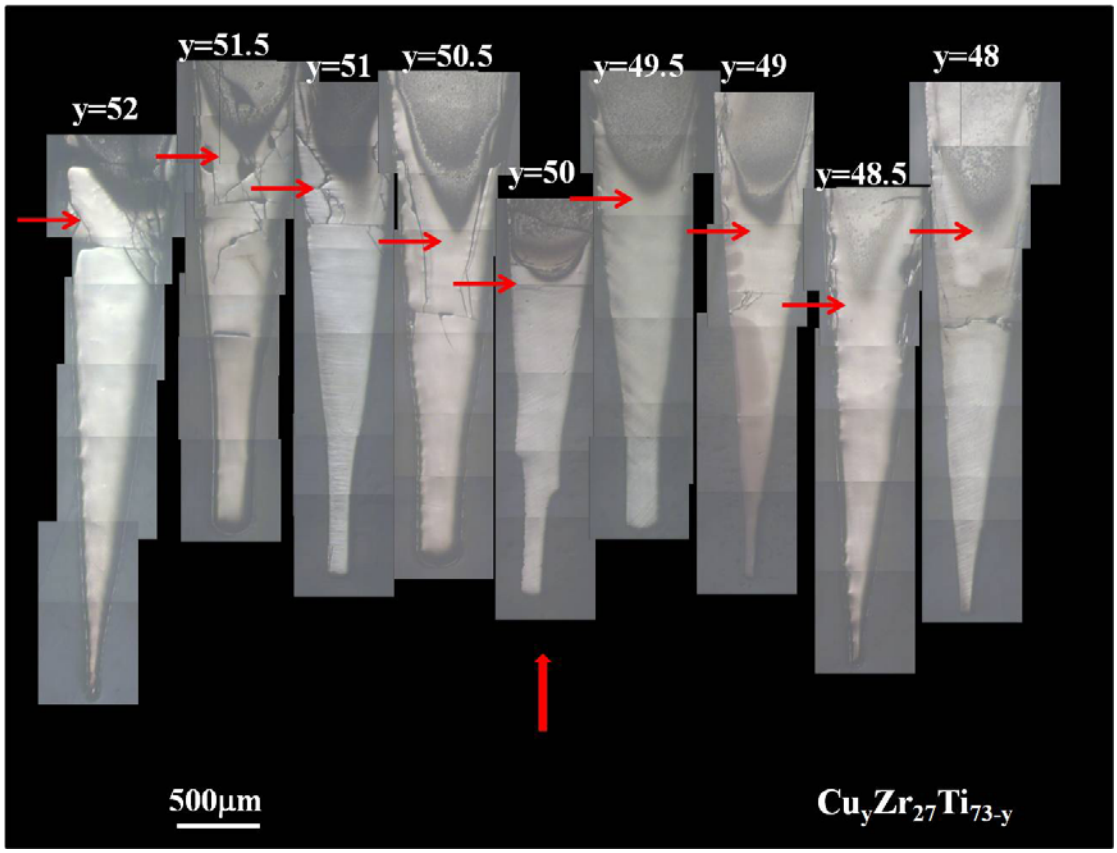

Figure 4.15 OM photos of the longitudinal view of the wedge cast samples of $Cu_yZr_{27}Ti_{73-y}$ (y=48-52).

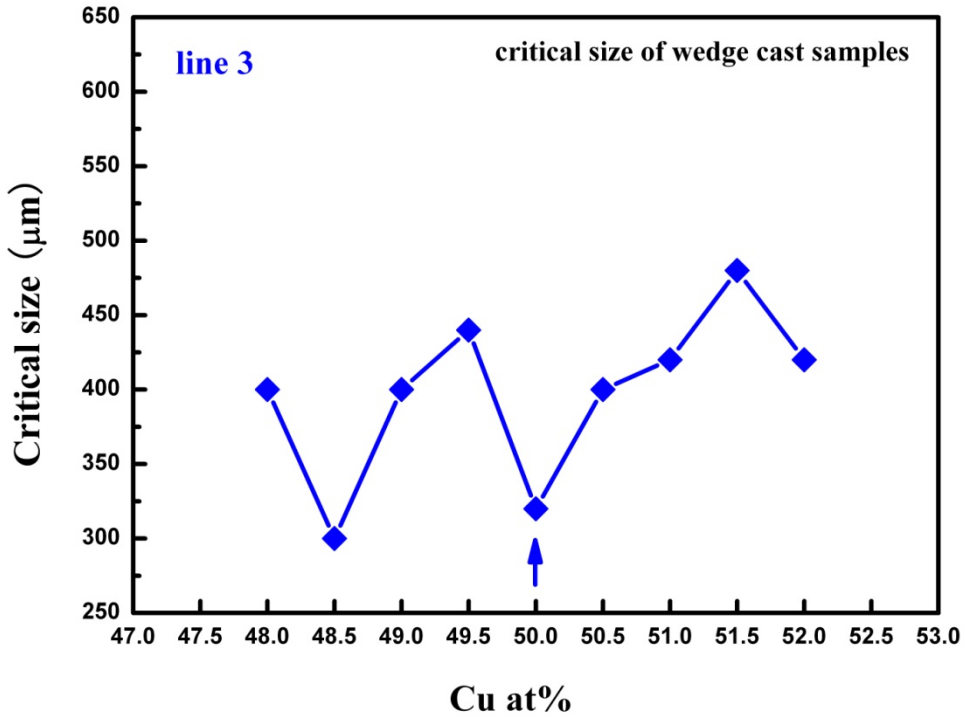

Figure 4.16 The critical sizes of the wedge cast samples of $Cu_yZr_{27}Ti_{73-y}$ (y=48-52).

Figure 4.17 summaries the critical thicknesses of compositions along line 1, 2 and 3. It is assumed that $Cu_{50}Zr_{27}Ti_{23}$ is the composition with minimum critical thickness, just like the intermetallic compound has the smallest critical thickness among the compositions near it in binary system. **Figure 4.17** suggest that there is a "ring" of peaks in critical thickness around $Cu_{50}Zr_{27}Ti_{23}$, although line 1 shows weakly fluctuation in critical thickness. It is noticed that the difference between the maximum and minimum values of the critical thickness is small: for line 2, one of the maximum values is only 400 μm as only 80-100 μm difference to the minimum value. It may be caused by the wide homogeneity composition range covered by the Laves phase: the

insensitivity to the composition variation leads to slightly changing in critical thickness. XRD and melting studies were carried out to confirm that the compositions studied are all located in the range of Cu_2ZrTi intermetallic phase.

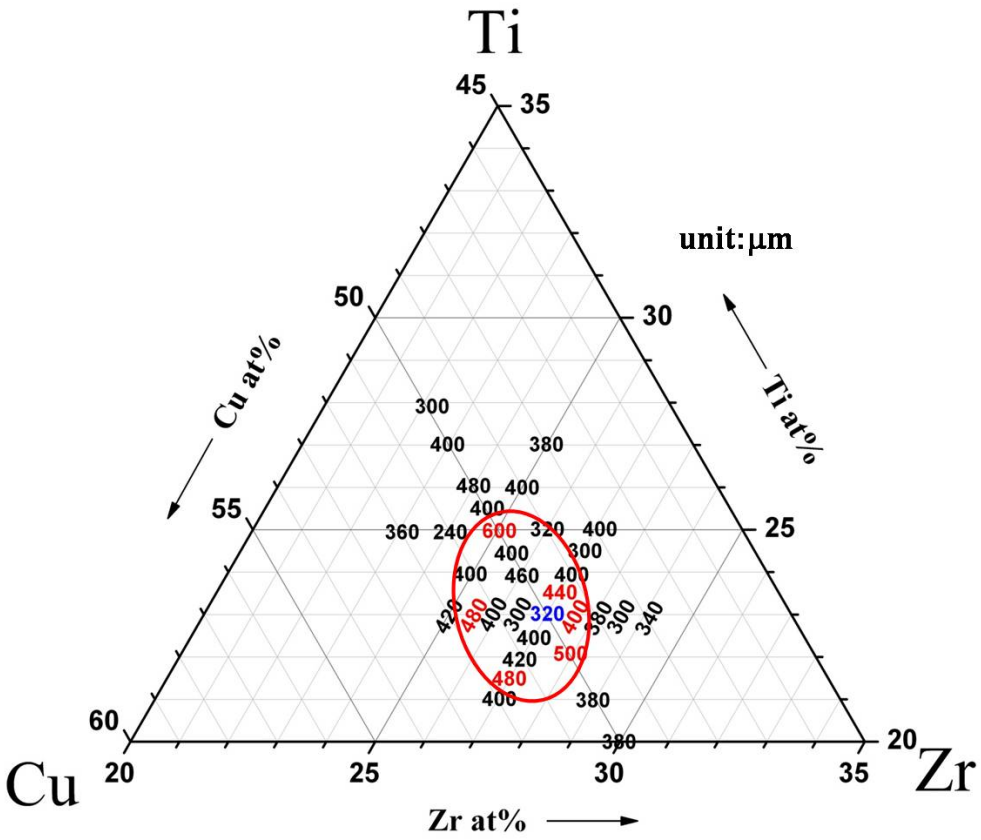

Figure 4.17 Summary of the critical sizes of compositions along line 1, 2 and 3. A "ring" of the peaks in the critical thickness is marked by the red circle. The red values represent the "peak" values of critical size and the blue value represents the critical thickness of composition $Cu_{50}Zr_{27}Ti_{23}$.

4.3.2 XRD and melting studies of the composition in line 1, 2 and 3

To identify the crystalline phase precipitated during the casting, the crystallization parts of all the wedge cast samples were investigated by XRD. **Figure 4.18** shows the resulting XRD patterns. In all these samples, only one phase can be detected, which is believed as Cu_2ZrTi phase. There is no other crystalline phase precipitated. It can be interpreted by the liquid project of the ternary phase diagram shown in **Figure 1.12**. It shows that the compositions studied in this section are away from any eutectic point reported. Therefore, the precipitation of other crystalline phases is kinetically suppressed under quenching. These XRD results prove that all the compositions studied are in the Laves phase range.

The melting temperatures and the liquidus temperatures were also measured for all the studied compositions. **Figure 4.19** shows the melting curves of these compositions. The liquidus temperatures of the alloys with compositions along line 1 do not change too much from each other, they all fluctuates around 1145K. For line 2, the liquidus temperature increases from 1143K at $Cu_{52}Zr_{25}Ti_{23}$ to 1154K at $Cu_{48}Zr_{29}Ti_{23}$. For line 3, liquid temperature increases from 1143K at $Cu_{52}Zr_{27}Ti_{21}$ to 1152K at $Cu_{48}Zr_{27}Ti_{25}$.

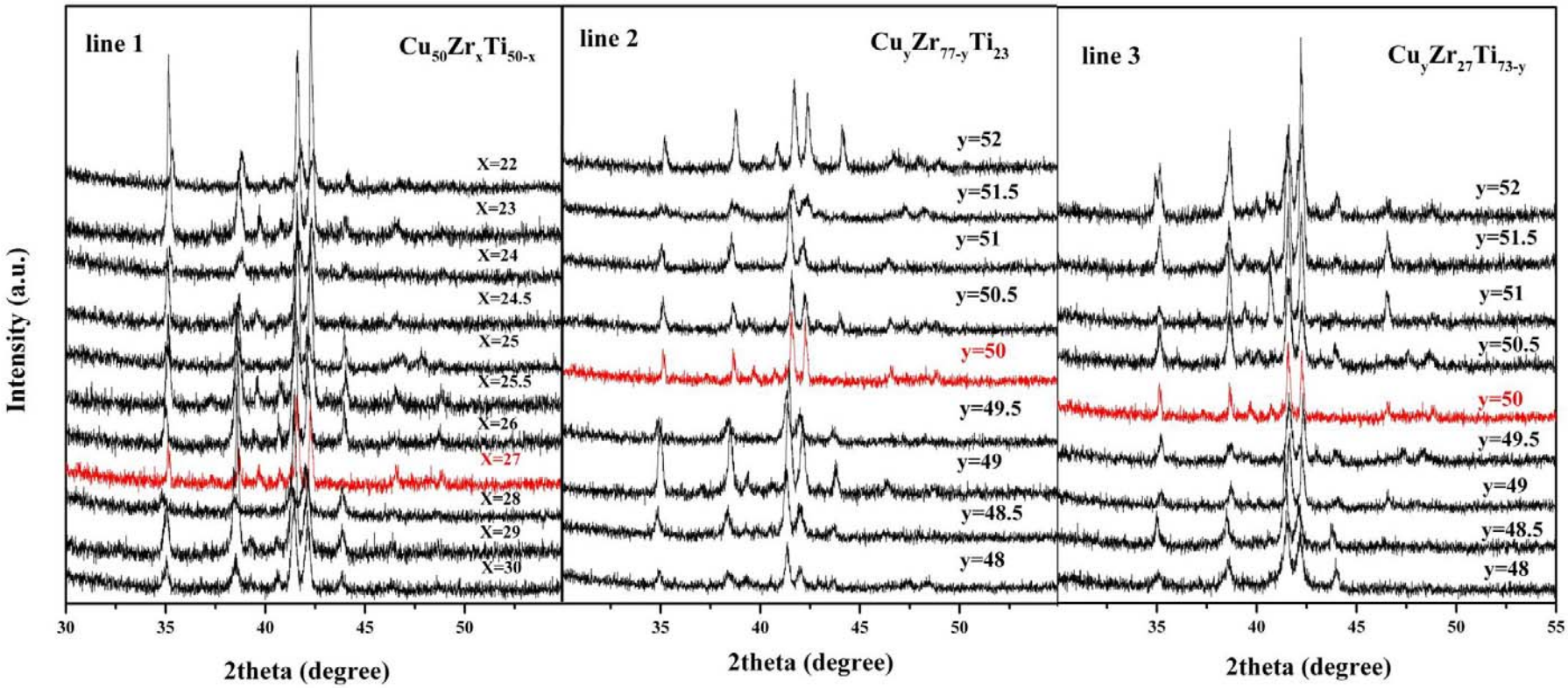

Figure 4.18 XRD patterns of the crystallization part of wedge cast samples of line 1, 2 and 3.

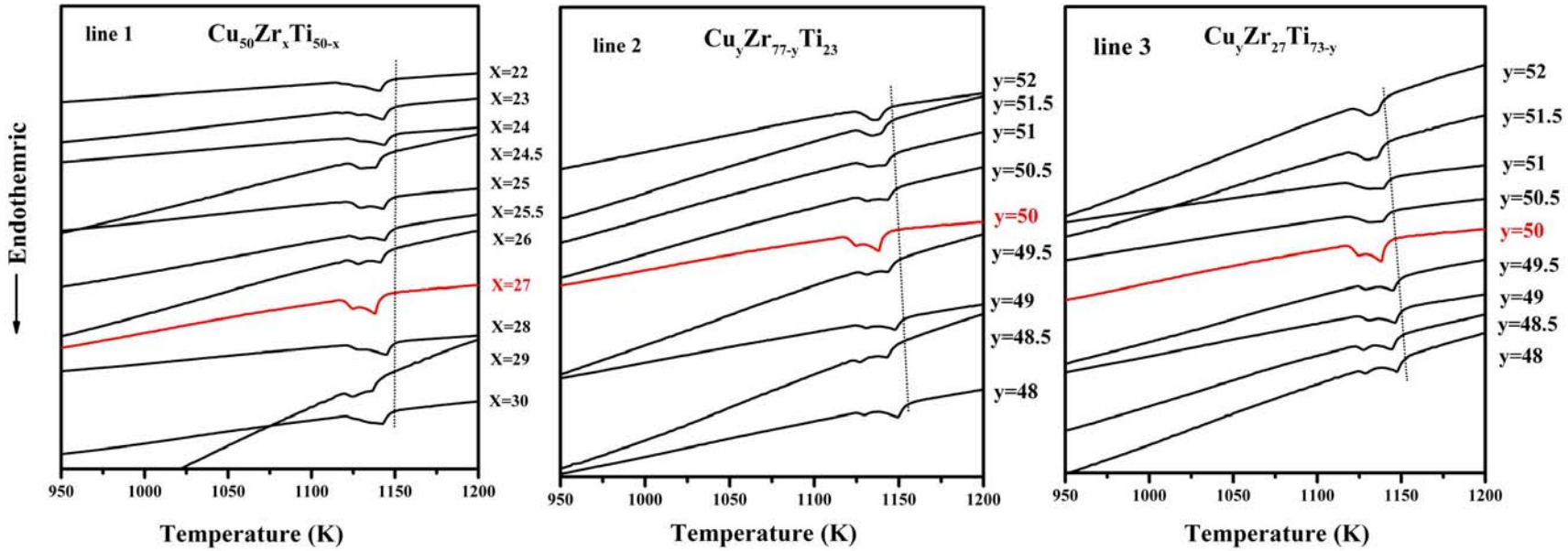

Figure 4.19 Melting curves of compositions in line 1, 2 and 3. The dash dot lines indicate the liquid temperature.

It indicates that the liquidus temperature increases with the decreasing Cu content in this Laves phase range. Moreover, there are two melting peaks in these melting curves and the first peak becomes smaller when the liquidus temperature is higher. It is believed that there should be only one melting peak if no other phase involved. In the binary system, like Zr-Cu system, the liquidus temperature of the intermetallic compound is higher than those of the compositions near it. It is assumed that the intermetallic glass may locate near the composition with the highest melting temperature. Therefore, further investigation need to be done to locate the composition with both the highest melting temperature and one melting peak.

According to **Figure 4.19**, the melting of a new composition line (line 4 and the compositions change from high Cu content to low Cu content) was studied, as shown in **Figure 4.20**. It clearly shows that the composition $Cu_{44}Zr_{30}Ti_{26}$ has the highest liquidus temperature, however, two melting peaks. $Cu_{42}Zr_{31}Ti_{27}$ shows only one melting peak, which means the Cu_2ZrTi phase is the only phase formed. Thus, the critical thicknesses of compositions around $Cu_{42}Zr_{31}Ti_{27}$ were studied and they were plotted in **Figure 4.21**. The critical thickness decreases from 420 μm at $Cu_{44}Zr_{30}Ti_{26}$ to 280 μm at $Cu_{40}Zr_{32}Ti_{28}$ except $Cu_{41}Zr_{31.5}Ti_{27.5}$. But $Cu_{41}Zr_{31.5}Ti_{27.5}$ should not be considered as a peak in critical thickness as its 360 μm critical thickness is only 20 μm higher than that of $Cu_{42}Zr_{31}Ti_{27}$. Therefore, there is no a pair of optimum glass formers near

$Cu_{42}Zr_{31}Ti_{27}$.

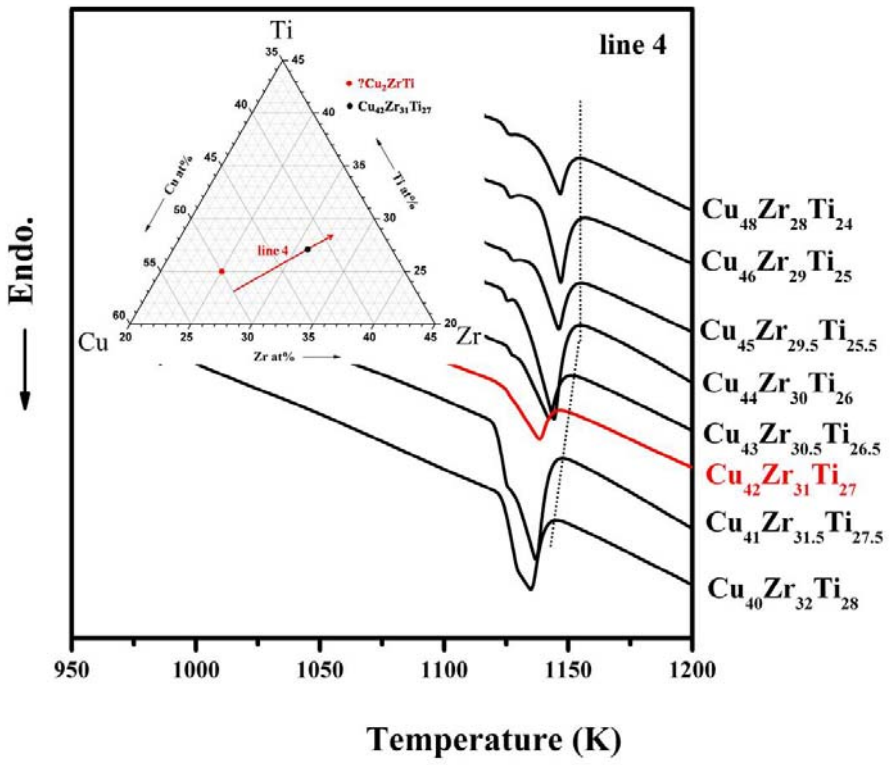

Figure 4.20 Melting curves of composition line 4.

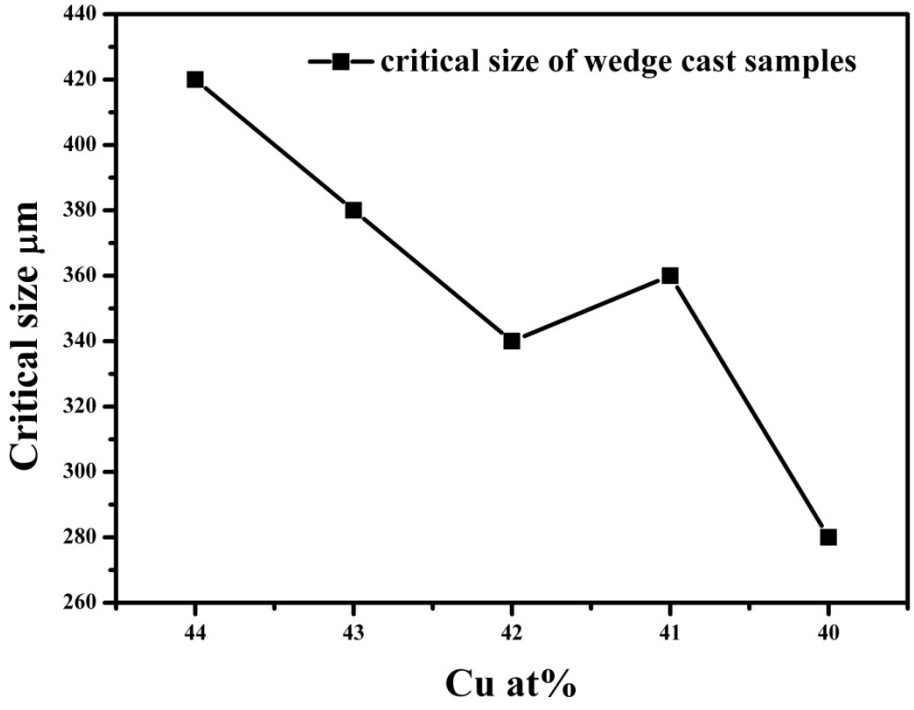

Figure 4.21 Critical sizes of compositions around $Cu_{42}Zr_{31}Ti_{27}$.

According to the experimental results mentioned above, the glass formation in the composition range of Cu_2ZrTi Laves phase can be summarized as following:

(1) $Cu_{50}Zr_{27}Ti_{23}$ has a relatively minimum critical thickness as 320 μm among the compositions around it, and there is a "ring" of peaks in critical thicknesses around it. However, the difference in critical thickness among all the compositions along line 1, 2 and 3 is not significant enough and the fluctuating of critical thickness in line 1 should not be ignored. Thus, the phenomenon of formation of intermetallic glasses may not be present in this Laves phase composition range.

(2) By the investigation of melting behavior, a new composition $Cu_{42}Zr_{31}Ti_{27}$ with relatively high liquidus temperature and one step of melting was located. But there is no a pair of optimum glass formers located near it, which is the character of intermetallic glass.

(3) It is unexpected that among all the compositions studied in this section, the composition with the maximum critical thickness is composition Cu_2ZrTi ($Cu_{50}Zr_{25}Ti_{25}$). The critical thickness of it reaches 600 μm, which is higher than that of $Ti_{35}Zr_{10}Cu_{55}$: 500 μm [97]. More importantly, $Ti_{35}Zr_{10}Cu_{55}$ is believed to be located near eutectic point and to be considered as a

eutectic glass former. This discovery is significant: usually, compositions in or near Laves phase region were considered as poor glass former; however, the critical thickness in Laves phase region in this section is higher than that of eutectic glass former.

(4) This study proves that Cu_2ZrTi intermetallic phase has a wide composition range. It also proves the glass formation in this composition range is more complicated than that near intermetallics in binary system. Further work need to be done to investigate the underlying mechanism of the glass formation in Laves phase or intermetallic with solubility.

4.4 Calculation of the glass forming range in Zr-Cu-Ti ternary system

For Zr-Cu-Ti ternary system, unlike the binary system, the CALPHAD method is no longer appropriate due to the lack of thermodynamic information of the ternary intermetallic phase. Also, the wide composition range of the Laves phase makes it more complicated. Therefore, Miedema method is used to calculate the glass forming range [120]. This model is actually a semi-empirical model adopting a few parameters to predict the heat

of mixing (or the enthalpy of formation) two pure liquid metals, resulting a liquid solution, solid solution or intermetallic and it is applicable to a plenty of alloy systems. The amorphous phase can form if the enthalpy of formation of the amorphous is less than that of the solid solution phase.

The enthalpy of formation of a solid solution is comprised by three parts: interfacial (chemical) enthalpy, elastic enthalpy and structural enthalpy, and for a binary system it can be written as [162]:

$$\Delta H_{AB}=\Delta H^{c}_{AB}+\Delta H^{e}_{AB}+\Delta H^{s}_{AB} \tag{4.1}$$

The chemical enthalpy of enthalpy of mixing can be obtained from:

$$\Delta H^{c}_{AB}=X_A X_B(X_A \Delta H^{inter}_{B\ in\ A}+X_B \Delta H^{inter}_{A\ in\ B}) \tag{4.2}$$

where X_A and X_B are the mole fraction of element A and B, respectively; ΔH^{inter} is the interfacial enthalpy of solving one mole of element A in an excess of element B and have a expression as:

$$\Delta H^{inter}_{A\ in\ B}=\frac{V_A^{2/3}}{\frac{1}{2}\left(\frac{1}{n_{ws\ A}^{1/3}}+\frac{1}{n_{ws\ B}^{1/3}}\right)}\{-P(\Delta\varphi)^2+Q(\Delta n_{ws}^{1/3})^2\} \tag{4.3}$$

where V_A is the mole volume of pure element A; n_{ws} is the electron density parameter; φ is the electronegativity or the work function of pure element; P and Q are constants, and for a transition-transition binary metal alloys, P=14.1 and Q/P=9.4.

For the enthalpy of elastic part, which is caused by the mismatch during mixing, can be defined as:

$$\Delta H^{e}_{AB}=X_A X_B(X_A \Delta H^{e}_{B\ in\ A}+X_B \Delta H^{e}_{A\ in\ B}) \tag{4.4}$$

where ΔH^{e} is the elastic enthalpy of per mole of element A in excess of element B and can be calculated based on the continuous elastic model (or the sphere and hole model) [163, 164]:

$$\Delta H^{e}_{A\ in\ B}=\frac{2K_A G_B (W_A-W_B)^2}{4G_B W_A+3K_A W_B} \tag{4.5}$$

where K and G are the bulk modulus and shear modulus respectively; W_A and W_B are the modified volumes of sphere and hole as:

$$W_A=V_A+\alpha\frac{(\varphi_A-\varphi_B)}{n^{A}_{ws}} \tag{4.6}$$

$$W_B = V_B + \alpha \frac{(\varphi_A - \varphi_B)}{n_{ws}^B} \tag{4.7}$$

and

$$\alpha = 1.5 \frac{V_A^{2/3}}{n_{ws}^{A\ -1/3} + n_{ws}^{B\ -1/3}} \tag{4.8}$$

For the structural enthalpy, the contribution to the enthalpy of formation is so small that it is neglected in this section.

For the case of amorphous phase, the enthalpy of formation does not comprise the elastic and structural parts but a part of enthalpy difference between the amorphous and crystalline states of the pure element, and can be written as [165, 166]:

$$\Delta H^{am} = \Delta H^{c} + X_A H_A^{a\text{-}s} + X_B H_B^{a\text{-}s} \tag{4.9}$$

where $\Delta H^{a\text{-}s}$ is the enthalpy difference between the amorphous and crystalline states of the pure element or enthalpy of topological and the quantity is given by [167]:

$$\Delta H_i^{a\text{-}s} = \alpha T_{m,i} \tag{4.10}$$

where α = 3.5 $Jmol^{-1}K^{-1}$ and $T_{m,i}$ is the melting temperature of element *i*. Furthermore, due to the short-range order structure of amorphous phase, a factor *f* was multiplied to the right part of equation (4.2) and *f* is given as [168]:

$$f=1+5(c_A^s c_B^s)^2 \tag{4.11}$$

where c^s_A and c^s_B are the surface fraction and can be defined as:

$$c_A^s=\frac{c_A V_A^{2/3}}{c_A V_A^{2/3}+c_B V_B^{2/3}} \tag{4.12}$$

$$c_B^s=\frac{c_B V_B^{2/3}}{c_A V_A^{2/3}+c_B V_B^{2/3}} \tag{4.13}$$

If extending the Miedema model to ternary systems, the enthalpy of formation of the solid solution have a similar form of that of the binary system and can be written as [162]:

$$\Delta H_{ABC}=\Delta H^c_{ABC}+\Delta H^e_{ABC}+\Delta H^s_{ABC} \tag{4.14}$$

$$\Delta H^c_{ABC}=\Delta H^c_{AB}+\Delta H^c_{AC}+\Delta H^c_{BC} \tag{4.15}$$

$$\Delta H^e_{ABC}=\Delta H^e_{AB}+\Delta H^e_{AC}+\Delta H^e_{BC} \tag{4.16}$$

and the enthalpy of formation of amorphous phase is:

$$\Delta H_{ABC}^{am}=\Delta H^{c}+X_A H_A^{a\text{-}s}+X_B H_B^{a\text{-}s}+X_C H_C^{a\text{-}s} \quad (4.17)$$

Table 4.1 Values of parameters needed to calculate the enthalpy of formation.

	Cu	**Zr**	**Ti**
φ **(V)**	4.45	3.45	3.80
n_{ws}	3.18	2.80	3.51
V **(×10^{-6}m^3/mol)**	7.09	14.06	10.64
T_m **(K)**	1356	2125	1939
G **(GPa)**	45.13	34.14	39.34
K **(GPa)**	130.10	83.35	105.20

Table 4.2 The calculated chemical enthalpies and elastic enthalpies.

	ΔH^{chem} **(KJ/mol)**	$\Delta H^{elastic}$ **(KJ/mol)**
Cu in Zr	-78	62
Zr in Cu	-110	96
Cu in Ti	-33	21
Ti in Cu	-40	33
Zr in Ti	-1	15
Ti in Zr	-1	15

All the parameters used to calculate the enthalpy of formation are taken from Refs [162] and [169] and they are listed in **Table 4.1**. By applying equations (4.2) to (4.8), the chemical enthalpies and elastic enthalpies are calculated and listed in **Table 4.2**.

By applying equations (4.1) to (4.17), the enthalpies of formation of solid solution phase and amorphous phase of Zr-Cu-Ti ternary system are calculated and plotted in **Figure 4.22** and **Figure 4.23**, respectively. **Figure 4.24** shows the values of difference between **Figure 4.22** and **Figure 4.23**. If the value of entropy of formation is considered as small enough to be ignored, the Gibbs free energy should equal to the enthalpy of formation. Thus the driving force of formation of amorphous phase should equal to the values of difference shown in **Figure 4.24**, where the influences from the binary or ternary intermetallics are ignored. It should be noticed that this result is only an approximated result; the modeling of the Gibbs free energy of Zr-Cu-Ti system is still an unsolved question. Therefore, the glass forming range in Zr-Cu-Ti ternary system is defined as where the value of the difference between the enthalpies of formation of solid solution phase and amorphous phase is positive [166]. The calculated glass forming range can be shown as **Figure 4.25**. It shows the glass forming range is quite wide, which covers from 15 at% to 95 at% of Cu, from 0 at% to 85 at% of Zr and from 0 at% to 70% of Ti.

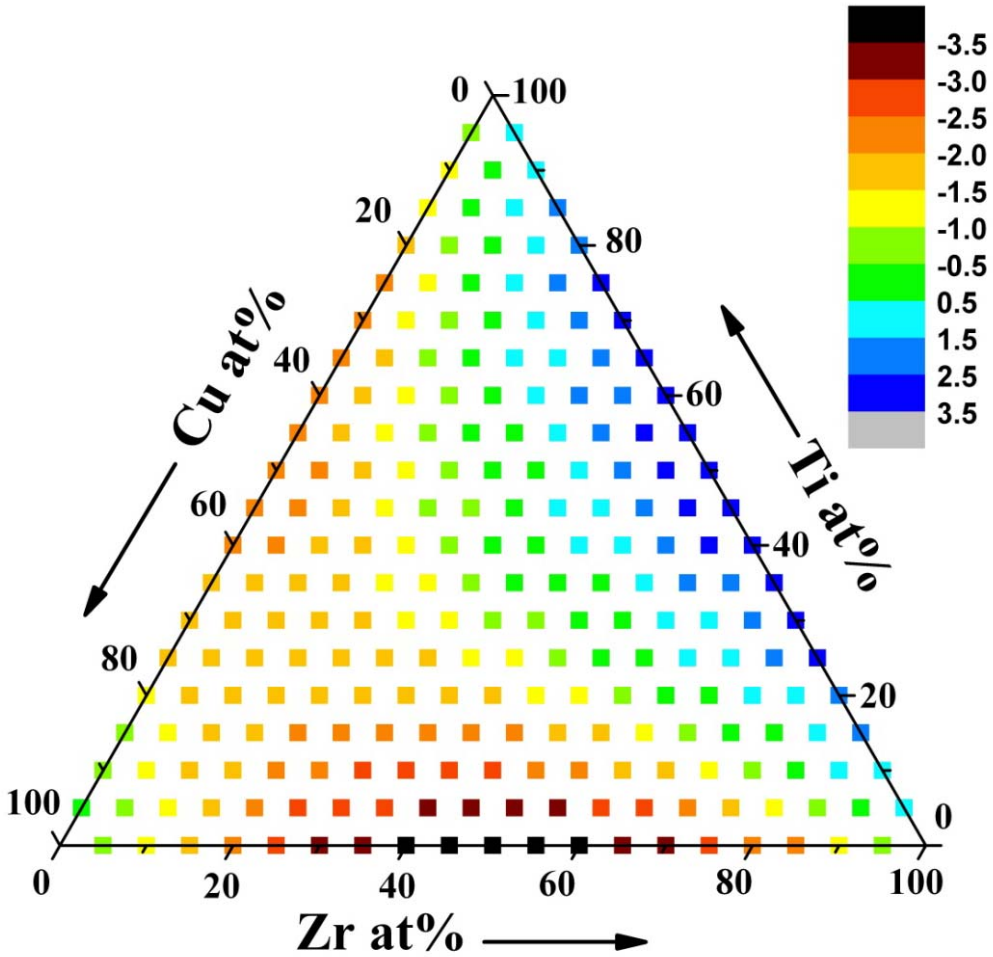

Figure 4.22 Color map of the calculated enthalpy of formation of solid solution phase in Zr-Cu-Ti ternary system. The unit is KJ/mol.

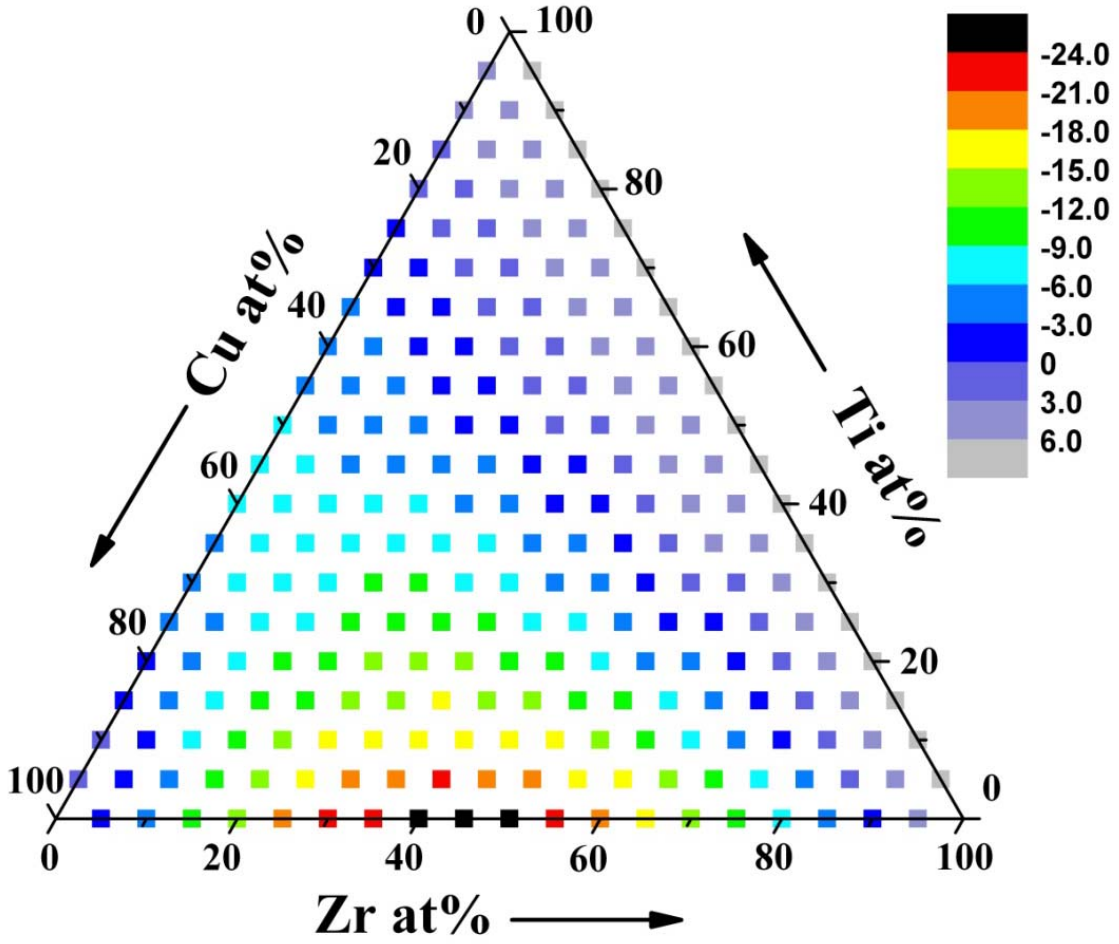

Figure 4.23 Color map of the calculated enthalpy of formation of amorphous phase in Zr-Cu-Ti ternary system. The unit is KJ/mol.

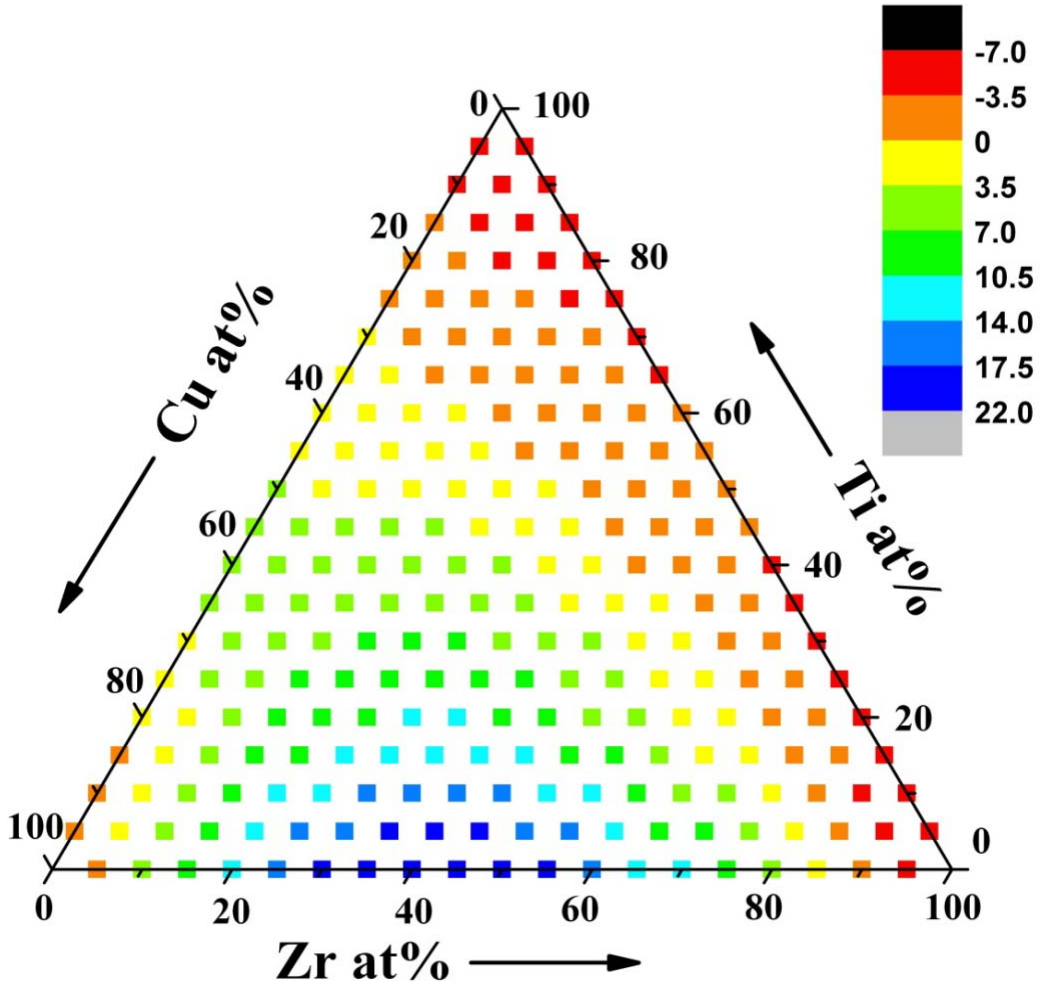

Figure 4.24 Color map of the approximated driving force of formation of amorphous phase for the Zr-Cu-Ti ternary system. The unit is KJ/mol.

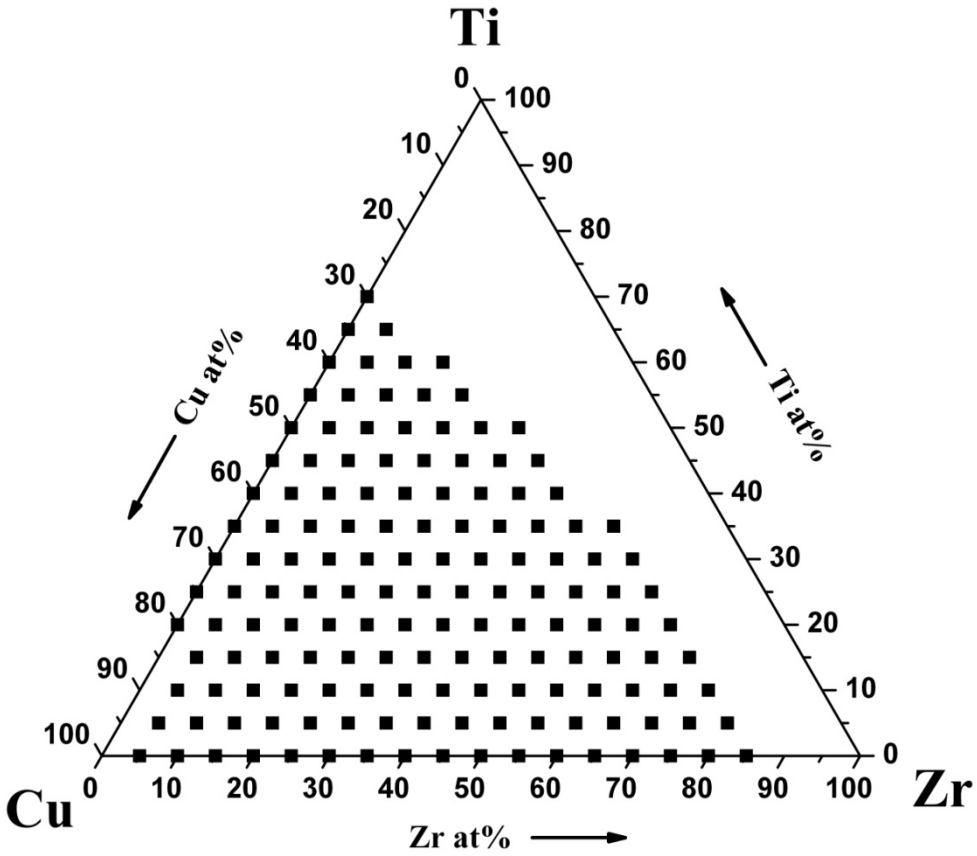

Figure 4.25 The calculated glass forming range in Zr-Cu-Ti ternary system.

This resulting ternary glass forming range is much wider than the experimental determined one [98, 151, 170, 171]. For the binary Cu-Ti and Zr-Cu systems, the calculated glass forming range covers from 30 at% Cu to 80 at % Cu in Cu-Ti system and from 5 at% to 85 at% Zr in Zr-Cu system. These are in agreement to the reported glass forming range in these two systems: from 28 at% to 75 at% Cu in Cu-Ti system [172, 173] and from 10 at% to 75 at% of Zr in Zr-Cu system [94].

It is believed that the enthalpy of mixing, or the enthalpy of chemical, plays an important role in the glass formation [9, 64, 159, 174]. It suggests that a larger negative enthalpy of mixing among the elements can lead to a better glass forming ability. Therefore, the enthalpy of mixing for the Zr-Cu-Ti ternary system is also calculated and shown in **Figure 4.26**. It shows that the large negative enthalpy of mixing can be found at compositions with 30 at% to 60 at% of Zr, 50 at% to 70 at% of Cu and 0 at% to 10 at% of Ti. This composition range is consistent with the reported compositions which can form bulk metallic glass in this Zr-Cu-Ti system: $Cu_{60}Zr_{40-x}Ti_x$, where x=0-40 at% [101] and compositions near $Cu_{52}Zr_{40}Ti_8$ [103]. Moreover, among the corresponding binary systems, Zr-Cu system has the relatively largest negative enthalpy of mixing and the best glass forming ability, followed by Cu-Ti system. The Zr-Ti system has no glass forming ability at all.

It should be noticed that the Cu_2ZrTi phase is treated as solid solution during the calculation in this section, which is based on the experimental result that the Cu_2ZrTi phase covers a wide composition range.

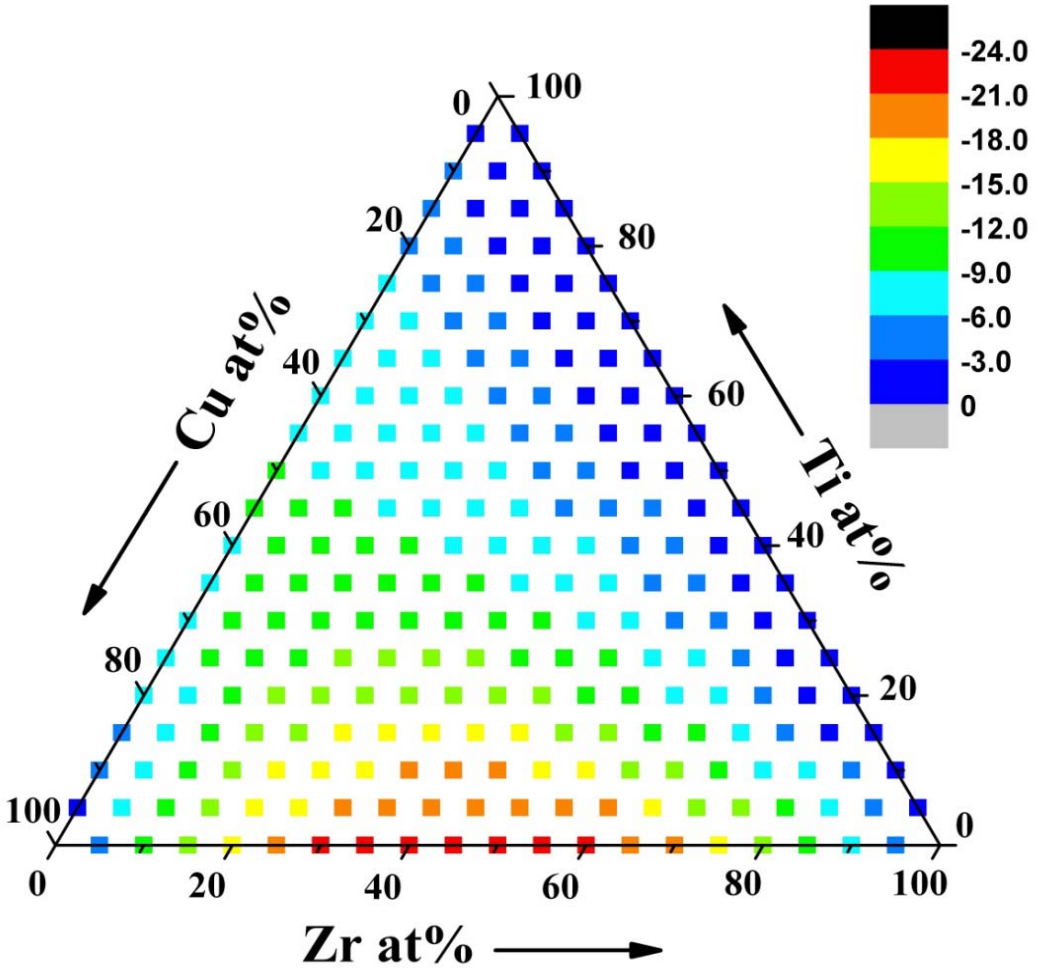

Figure 4.26 Color map of the calculated enthalpy of mixing (enthalpy of chemical) for the Zr-Cu-Ti ternary system. The unit is KJ/mol.

4.5 Conclusion

In this chapter, the glass formation of two composition ranges in Zr-Cu-Ti system has been studied. Miedema model was used to calculate the enthalpy of mixing, enthalpy of elastic, enthalpy of formation and glass formation range. The followings are the conclusions:

(1) For the compositions from $Cu_{52.5}(ZrTi)_{47.5}$ to $Cu_{47}(ZrTi)_{53}$ (Ti = 5 at%), the phenomenon of intermetallic glass still can be observed as two optimum glass formers $Cu_{51.5}(ZrTi)_{48.5}$ and $Cu_{48}(ZrTi)_{52}$ are separated by composition $Cu_{51}(ZrTi)_{49}$. The critical size reaches to 3 mm by the Ti addition. $Cu_{10}Zr_7$ phase was stabilized by Ti and precipitated with CuZr phase during the cooling.

(2) For the compositions nearby Cu_2ZrTi, the phenomenon of intermetallic glass is not clear enough. The critical sizes fluctuated from ~300 μm to 600 μm. The liquidus temperature changes slowly with the changing of composition. A wide composition range was proved to be covered by Cu_2ZrTi intermetallic.

(3) The Miedema model was used to calculate the glass forming range for

Zr-Cu-Ti system. The resulting glass forming range covers from 15 at% to 95 at% of Cu, from 0 at% to 85 at% of Zr and from 0 at% to 70% of Ti. Also the enthalpy of mixing (chemical) was calculated and the possible composition range with good glass forming ability was suggested.

Chapter 5

Conclusion

5.1 Summary of results

This dissertation has explored the phenomenon of formation of intermetallic glass in binary and ternary systems, the relationship between the glass forming ability of intermetallic glass and the crystallization driving force or the temperature dependant viscosity. Also the possible glass forming range in ternary system has been studied. The major results are summarized as follows:

(1) The glass formation near $Cu_{51}Zr_{14}$, Cu_8Zr_3, $Cu_{10}Zr_7$ and $CuZr_2$ intermetallics

has been systemically studied. Intermetallic glasses can be easily located near almost all intermetallic compounds in the Cu-Zr binary system. Two optimum intermetallic glass formers were located near but separated by the corresponding intermetallic ($Cu_{51}Zr_{14}$, $Cu_{10}Zr_7$ and $CuZr_2$ intermetallics), respectively. The result shows that glass formed near $Cu_{10}Zr_7$ intermetallic has the a maximum critical thickness of 520 μm, followed by glass near $CuZr_2$ intermetallic with 470 μm critical thickness and glass near $Cu_{51}Zr_{14}$ intermetallic with less than 15 μm critical thickness. Due to the fact that Cu_8Zr_3 intermetallic is a peritectic phase, only one optimum glass former was found near it.

(2) The Gibbs free energy as a function of composition of liquid and intermetallic phases is calculated by CALPHAD method at different temperatures. All the crystallization driving forces at compositions $Cu_{51}Zr_{14}$, $Cu_{10}Zr_7$, CuZr and $CuZr_2$ are also calculated under their corresponding T_g or T_x temperatures. According to the relationship between the maximum critical thickness of the intermetallic glass and the crystallization driving force of the corresponding intermetallic, a smaller crystallization driving force is related to a better glass forming ability.

(3) The nature of formation of intermetallic glasses was explained from both thermodynamic and kinetic perspectives. Thermodynamically, it is

proposed that the Gibbs free energy of intermetallic rises sharply near intermetallic composition. The liquid phase has a lower Gibbs free energy when the composition shifts slightly from the intermetallic compound. Thus two thermodynamically favored glass forming ranges are present, when the formation of neighbor primary phases was kinetically suppressed under quenching. Kinetically, it is surprisingly found that the two optimum glass formers near intermetallic compound have lower critical cooling rates (which lead to a better glass forming ability) than that of the corresponding intermetallic compound. This provides a kinetic evidence of the formation of intermetallic glass. The changing of critical cooling rate in such a narrow composition range can be considered as an evidence of the sharp profile of the Gibbs free energy of the intermetallic phase.

(4) The formation of intermetallic glass was also studied in Zr-Cu-Ti ternary system. Based on the glass formation near CuZr intermetallic in binary system, the glass formation of the compositions from $Cu_{52.5}(ZrTi)_{47.5}$ to $Cu_{47}(ZrTi)_{53}$ (Ti = 5 at%) was studied. The phenomenon of formation of intermetallic glass still can be observed as two optimum glass formers $Cu_{51.5}(ZrTi)_{48.5}$ and $Cu_{48}(ZrTi)_{52}$ are located near but separated by composition $Cu_{51}(ZrTi)_{49}$ in both 3 mm and 5 mm rods. The critical size is improved to 3 mm by adding Ti element into Zr-Cu system. $Cu_{10}Zr_7$ phase

was stabilized by Ti and precipitated along with CuZr phase in this composition range.

(5) Glass formation in the composition range of Cu_2ZrTi ternary intermetallic phsae, or Laves phase, was also studied. The phenomenon of intermetallic glass is not clear enough. The critical sizes of the wedge cast samples fluctuated from ~300 μm to 600 μm without consistently trend. Cu_2ZrTi ($Cu_{50}Zr_{25}Ti_{25}$) was discovered to have a critical thickness of 600 μm, which is larger than that of eutectic glass $Ti_{35}Zr_{10}Cu_{55}$. Furthermore, the liquidus temperature in this composition range changes slowly with the changing of composition. Along with the XRD results of the crystalline parts of all the samples, it reveals that Cu_2ZrTi intermetallic covers a wide composition range more than 10 at%.

(6) The Miedema model was used to calculate the glass forming range in Zr-Cu-Ti ternary system. The resulting glass forming range covers from 15 at% to 95 at% of Cu, from 0 at% to 85 at% of Zr and from 0 at% to 70% of Ti, which is much wider than reported experimental glass forming range. Also the enthalpy of mixing (chemical) was calculated and the possible composition range with good glass forming ability (compositions with 30 at% to 60 at% of Zr, 50 at% to 70 at% of Cu and 0 at% to 10 at% of Ti) was suggested.

5.2 Future work

This thesis demonstrates the experimental phenomenon and underlying mechanism of formation of intermetallic glass. However, the intermetallic glass is a new family of metallic glasses, there are more work needed to do. Based on the current results and understanding, the following points are raised for future work:

(1) In binary system, the intermetallic phases selected in this thesis are all line compounds with no solubility. Also, the investigation of glass formation in Cu_2ZrTi phase did not show convincing evidence of existence of intermetallic glass. Therefore, binary intermetallic phase with limited solubility would be a great choice to study whether the phenomenon of formation of intermetallic glass is present.

(2) The phenomenon of formation of intermetallic glass makes a challenge for the modeling of the structure of metallic glass. The glass forming ability is sharply dependant on the composition in such a narrow composition range. There is no method to modeling the structure of intermetallic glass so far. Knowing the structure of intermetallic glass would help the further investigation.

(3) It would be interesting to study the mechanical property of intermetallic glass. Since intermetallic glass has different glass forming range from eutectic glasses, whether they show similar mechanical property is still open to question.

Bibliography

[1]. Klement W., Willens R.H.,Duwez P., *Nature* 1960; **187**, 869-870.

[2]. Duwez P., Willens R.H.,Klement W., *J. Appl. Phys.* 1960; **31**, 1136-1137.

[3]. Chen H.S., *Acta Metallurgica* 1974; **22**, 1505-1511.

[4]. Kui H.W., Greer A.L.,Turnbull D., *Appl. Phys. Lett.* 1984; **45**, 615-616.

[5]. Inoue A., Zhang T.,Masumoto T., *Mater. Trans. JIM* 1989; **30**, 965-972.

[6]. Inoue A., Yamaguchi H., Zhang T.,Masumoto T., *Mater. Trans. JIM* 1990; **31**, 104-109.

[7]. Inoue A., Nakamura T., Sugita T., Zhang T.,Masumoto T., *Mater. Trans. JIM* 1993; **34**, 351-358.

[8]. Inoue A., Zhang T.,Masumoto T., *Mater. Trans. JIM* 1990; **31**, 425-428.

[9]. Inoue A., *Acta Mater.* 2000; **48**, 279-306.

[10]. Guo F.Q., Poon S.J.,Shiflet G.J., *Appl. Phys. Lett.* 2003; **83**, 2575-2577.

[11]. Park E.S.,Kim D.H., *Appl. Phys. Lett.* 2005; **86**, 3.

[12]. Schroers J., Lohwongwatana B., Johnson W.L.,Peker A., *Appl. Phys. Lett.* 2005; **87**, 3.

[13]. Zhang B., Zhao D.Q., Pan M.X., Wang W.H.,Greer A.L., *Phys. Rev. Lett.*

2005; **94**, 4.

[14]. Inoue A., Nakamura T., Nishiyama N.,Masumoto T., *Mater. Trans. JIM* 1992; **33**, 937-945.

[15]. Dai C.L. *et al.*, *Scr. Mater.* 2006; **54**, 1403-1408.

[16]. Shen J., Chen Q.J., Sun J.F., Fan H.B.,Wang G., *Appl. Phys. Lett.* 2005; **86**, 3.

[17]. Peker A.,Johnson W.L., *Appl. Phys. Lett.* 1993; **63**, 2342-2344.

[18]. Inoue A., Zhang T., Nishiyama N., Ohba K.,Masumoto T., *Mater. Trans. JIM* 1993; **34**, 1234-1237.

[19]. Li Y., Jones H.,Davies H.A., *Scr. Metall. Materialia* 1992; **26**, 1371-1375.

[20]. Kim Y.J., Busch R., Johnson W.L., Rulison A.J.,Rhim W.K., *Appl. Phys. Lett.* 1994; **65**, 2136-2138.

[21]. Li Y., Liu H.Y., Davies H.A.,Jones H., *Mater. Sci. Eng. A-Struct. Mater. Prop. Microstruct. Process.* 1994; **179**, 628-631.

[22]. Inoue A., Shinohara Y.,Gook J.S., *Mater. Trans. JIM* 1995; **36**, 1427-1433.

[23]. Li Y., Liu H.Y.,Jones H., *J. Mater. Sci.* 1996; **31**, 1857-1863.

[24]. Inoue A.,Zhang T., *Mater. Sci. Eng. A-Struct. Mater. Prop. Microstruct. Process.* 1997; **226**, 393-396.

[25]. Zhang T.,Inoue A., *Mater. Trans. JIM* 1998; **39**, 1001-1006.

[26]. Wang X.M., Yoshii I., Inoue A., Kim Y.H.,Kim I.B., *Mater. Trans. JIM* 1999; **40**, 1130-1136.

[27]. Pang S.J., Zhang T., Asami K.,Inoue A., *Acta Mater.* 2002; **50**, 489-497.

[28]. Inoue A., Shen B.L., Koshiba H., Kato H.,Yavari A.R., *Nat. Mater.* 2003; **2**, 661-663.

[29]. Amiya K.,Inoue A., *Mater. Trans.* 2006; **47**, 1615-1618.

[30]. Inoue A.,Zhang T., *Mater. Trans. JIM* 1996; **37**, 185-187.

[31]. Xu D.H., Duan G., Johnson W.L.,Garland C., *Acta Mater.* 2004; **52**, 3493-3497.

[32]. Inoue A., Nishiyama N.,Kimura H., *Mater. Trans. JIM* 1997; **38**, 179-183.

[33]. Xu D.H., Duan G.,Johnson W.L., *Phys. Rev. Lett.* 2004; **92**, 4.

[34]. Ponnambalam V., Poon S.J.,Shiflet G.J., *J. Mater. Res.* 2004; **19**, 3046-3052.

[35]. Ma H., Shi L.L., Xu J., Li Y.,Ma E., *Appl. Phys. Lett.* 2005; **87**, 3.

[36]. Mu J. *et al., Adv. Eng. Mater.* 2009; **11**, 530-532.

[37]. Zhuo L.C., Pang S.J., Wang H.,Zhang T., *Chin. Phys. Lett.* 2009; **26**, 4.

[38]. Inoue A.,Zhang T., *Mater. Trans. JIM* 1995; **36**, 1184-1187.

[39]. Inoue A.,Nishiyama N., *MRS Bull.* 2007; **32**, 651-658.

[40]. Busch R., Kim Y.J.,Johnson W.L., *J. Appl. Phys.* 1995; **77**, 4039-4043.

[41]. Greer A.L., *Nature* 1993; **366**, 303-304.

[42]. Inoue A., *Mater. Trans. JIM* 1995; **36**, 866-875.

[43]. Busch R., Liu W.,Johnson W.L., *J. Appl. Phys.* 1998; **83**, 4134-4141.

[44]. Busch R., Schroers J.,Wang W.H., *MRS Bull.* 2007; **32**, 620-623.

[45]. Tsao S.S.,Spaepen F., *Acta Metallurgica* 1985; **33**, 881-889.

[46]. Volkert C.A.,Spaepen F., *Acta Metallurgica* 1989; **37**, 1355-1362.

[47]. Busch R., *JOM-J. Miner. Met. Mater. Soc.* 2000; **52**, 39-42.

[48]. Heilmaier M.,Eckert J., *JOM-J. Miner. Met. Mater. Soc.* 2000; **52**, 43-47.

[49]. Stillinger F.H., *Science* 1995; **267**, 1935-1939.

[50]. Angell C.A., *Science* 1995; **267**, 1924-1935.

[51]. Johnson W.L., *MRS Bull.* 1999; **24**, 42-56.

[52]. Shadowspeaker L.,Busch R., *Appl. Phys. Lett.* 2004; **85**, 2508-2510.

[53]. Mukherjee S., Schroers J., Johnson W.L.,Rhim W.K., *Phys. Rev. Lett.* 2005; **94**, 4.

[54]. Turnbull D., *Contemp. Phys.* 1969; **10**, 473.

[55]. Lu Z.P., Li Y.,Ng S.C., *J. Non-Cryst. Solids* 2000; **270**, 103-114.

[56]. Tan H., Zhang Y., Ma D., Feng Y.P.,Li Y., *Acta Mater.* 2003; **51**, 4551-4561.

[57]. Wang D. *et al., Appl. Phys. Lett.* 2004; **84**, 4029-4031.

[58]. Kim S.G., Inoue A.,Masumoto T., *Mater. Trans. JIM* 1990; **31**, 929-934.

[59]. Inoue A., Zhang T.,Masumoto T., *Mater. Trans. JIM* 1990; **31**, 177-183.

[60]. Inoue A., Nishiyama N.,Matsuda T., *Mater. Trans. JIM* 1996; **37**, 181-184.

[61]. Inoue A., Zhang T.,Takeuchi A., *Appl. Phys. Lett.* 1997; **71**, 464-466.

[62]. Inoue A., Zhang T.,Masumoto T., *J. Non-Cryst. Solids* 1993; **156**, 473-480.

[63]. Inoue A., *Sci. Rep. Res. Inst. Tohoku Univ. Ser. A-Phys. Chem. Metall.* 1996; **42**, 1-11.

[64]. Takeuchi A.,Inoue A., *Mater. Trans.* 2005; **46**, 2817-2829.

[65]. Ma D., Tan H., Wang D., Li Y.,Ma E., *Appl. Phys. Lett.* 2005; **86**, 3.

[66]. Zhang J., Tan H., Feng Y.P.,Li Y., *Scr. Mater.* 2005; **53**, 183-187.

[67]. Wang D., Tan H.,Li Y., *Acta Mater.* 2005; **53**, 2969-2979.

[68]. Wang Y.X., Yang H., Lim G.,Li Y., *Scr. Mater.* 2010; **62**, 682-685.

[69]. Telford M., *Materials Today* 2004; **7**, 36-43.

[70]. Zhang T., Inoue A.,Masumoto T., *Materials Science and Engineering: A* 1994; **181/182**, 1423-1426.

[71]. Zhang T., Inoue A.,Masumoto T., *Mater. Trans. JIM* 1991; **32**, 1005-1010.

[72]. Zhang Q.S., Zhang W.,Inoue A., *Scr. Mater.* 2006; **55**, 711-713.

[73]. Das J. *et al.*, *Phys. Rev. Lett.* 2005; **94**, 4.

[74]. Inoue A., Zhang W., Tsurui T., Yavari A.R.,Greer A.L., *Philos. Mag. Lett.* 2005; **85**, 221-229.

[75]. Zhu Z.W., Zhang H.F., Sun W.S., Ding B.Z.,Hu Z.Q., *Scr. Mater.* 2006; **54**, 1145-1149.

[76]. Atzmon M., Verhoeven J.D., Gibson E.D.,Johnson W.L., *Appl. Phys. Lett.* 1984; **45**, 1052-1053.

[77]. Xu D.H., Lohwongwatana B., Duan G., Johnson W.L.,Garland C., *Acta Mater.* 2004; **52**, 2621-2624.

[78]. Inoue A.,Zhang W., *Mater. Trans.* 2004; **45**, 584-587.

[79]. Tang M.B., Zhao D.Q., Pan M.X.,Wang W.H., *Chin. Phys. Lett.* 2004; **21**, 901-903.

[80]. Li Y., Guo Q., Kalb J.A.,Thompson C.V., *Science* 2008; **322**, 1816-1819.

[81]. Wu W.F.,Li Y., *Appl. Phys. Lett.* 2009; **95**, 3.

[82]. Schwarz R.B.,Johnson W.L., *Phys. Rev. Lett.* 1983; **51**, 415-418.

[83]. Johnson W.L., *Progress in Materials Science* 1986; **30**, 81-134.

[84]. Johnson W.L., *Materials Science and Engineering* 1988; **97**, 1-13.

[85]. Hellstern E.,Schultz L., *Philos. Mag. B-Phys. Condens. Matter Stat. Mech. Electron. Opt. Magn. Prop.* 1987; **56**, 443-448.

[86]. Ansara I., Pasturel A.,Buschow K.H.J., *Phys. Status Solidi A-Appl. Res.* 1982; **69**, 447-453.

[87]. Saunders N., *Calphad-Comput. Coupling Ph. Diagrams Thermochem.* 1985; **9**, 297-309.

[88]. Zeng K.J., Hamalainen M.,Lukas H.L., *Journal of Phase Equilibria* 1994; **15**, 577-586.

[89]. Kleppa O.J.,Watanabe S., *Metallurgical Transactions B-Process Metallurgy* 1982; **13**, 391-401.

[90]. Zhou S.H.,Napolitano R.E., *Acta Mater.* 2010; **58**, 2186-2196.

[91]. Saunders N.,Miodownik A.P., *Mater. Sci. Technol.* 1988; **4**, 768-777.

[92]. Altounian Z., Tu G.H.,Stromolsen J.O., *J. Appl. Phys.* 1982; **53**, 4755-4760.

[93]. Kneller E., Khan Y.,Gorres U., *Z. Metallk.* 1986; **77**, 152-163.

[94]. Buschow K.H.J., *J. Appl. Phys.* 1981; **52**, 3319-3323.

[95]. Buschow K.H.J., *Journal of Physics F-Metal Physics* 1984; **14**, 593-607.

[96]. Li C.R., Chen S.C., Du Z.M., Guo C.P.,Wang N., *Intermetallics* 2011; **19**, 1678-1682.

[97]. Lin X.H.,Johnson W.L., *J. Appl. Phys.* 1995; **78**, 6514-6519.

[98]. Massalski T.B., Woychik C.G.,Dutkiewicz J., *Metallurgical Transactions a-Physical Metallurgy and Materials Science* 1988; **19**, 1853-1860.

[99]. Woychik C.G.,Massalski T.B., *Z. Metallk.* 1988; **79**, 149-153.

[100]. Arroyave R., Eagar T.W.,Kaufman L., *J. Alloy. Compd.* 2003; **351**, 158-170.

[101]. Inoue A., Zhang W., Zhang T.,Kurosaka K., *Acta Mater.* 2001; **49**, 2645-2652.

[102]. Inoue A., Zhang W., Zhang T.,Kurosaka K., *Mater. Trans.* 2001; **42**, 1149-1151.

[103]. Dai C.L., Guo H., Li Y.,Xu J., *J. Non-Cryst. Solids* 2008; **354**, 3659-3665.

[104]. Greer A.L., *Science* 1995; **267**, 1947-1953.

[105]. Chen H.S., *Rep. Prog. Phys.* 1980; **43**, 353-432.

[106]. Schwarz R.B., Petrich R.R.,Saw C.K., *J. Non-Cryst. Solids* 1985; **76**, 281-302.

[107]. Koch C.C., Cavin O.B., McKamey C.G.,Scarbrough J.O., *Appl. Phys. Lett.* 1983; **43**, 1017-1019.

[108]. Yeh X.L., Samwer K.,Johnson W.L., *Appl. Phys. Lett.* 1983; **42**, 242-244.

[109]. Vitek J.M., Vandersande J.B.,Grant N.J., *Acta Metallurgica* 1975; **23**,

165-176.

[110]. Freed R.L.,Vandersande J.B., *J. Non-Cryst. Solids* 1978; **27**, 9-28.

[111]. Kerns A.J., Polk D.E., Ray R.,Giessen B.C., *Materials Science and Engineering* 1979; **38**, 49-53.

[112]. Glade S.C. *et al., J. Appl. Phys.* 2000; **87**, 7242-7248.

[113]. Palumbo M.,Battezzati L., *Calphad-Comput. Coupling Ph. Diagrams Thermochem.* 2008; **32**, 295-314.

[114]. Saunders. N.,Miodownik. A.P., *CALPHAD (calculation of phase diagrams) : a comprehensive guide* 1998, New York : Pergamon.

[115]. Wang N., Li C.R., Du Z.M., Wang F.M.,Zhang W.J., *Calphad-Comput. Coupling Ph. Diagrams Thermochem.* 2006; **30**, 461-469.

[116]. Baricco M.,Palumbo M., *Adv. Eng. Mater.* 2007; **9**, 454-467.

[117]. Shao G., *J. Appl. Phys.* 2000; **88**, 4443-4445.

[118]. Turchanin M.A., Agraval P.G.,Abdulov A.R., *Powder Metall. Met. Ceram.* 2008; **47**, 428-446.

[119]. Turchanin M.A., Velikanova T.Y., Agraval P.G., Abdulov A.R.,Dreval L.A., *Powder Metall. Met. Ceram.* 2008; **47**, 586-606.

[120]. Miedema A.R., Dechatel P.F.,Deboer F.R., *Physica B & C* 1980; **100**, 1-28.

[121]. Miedema A.R., *Journal of the Less-Common Metals* 1973; **32**, 117-136.

[122]. Miedema A.R., Boom R.,Deboer F.R., *Journal of the Less-Common Metals* 1975; **41**, 283-298.

[123]. Niessen A.K., Miedema A.R., Deboer F.R.,Boom R., *Physica B & C* 1988; **151**, 401-432.

[124]. Dinsdale A.T., *Calphad-Comput. Coupling Ph. Diagrams Thermochem.* 1991; **15**, 317-425.

[125]. Gierlotka W., Zhang K.C.,Chang Y.P., *J. Alloy. Compd.* 2011; **509**, 8313-8318.

[126]. Shao G., *Intermetallics* 2003; **11**, 313-324.

[127]. Zeng K.J., Hämäläinen M.,Lukas H.L., *Journal of Phase Equilibria and Diffusion* 1994; **15**, 577-586.

[128]. Abe T., Shimono M., Ode M.,Onodera H., *Acta Mater.* 2006; **54**, 909-915.

[129]. Xia L., Fang S.S., Wang Q., Dong Y.D.,Liu C.T., *Appl. Phys. Lett.* 2006; **88**, 3.

[130]. Uhlmann D.R., *J. Non-Cryst. Solids* 1972; **7**, 337-348.

[131]. Davies H.A., Aucote J.,Hull J.B., *Scripta Metallurgica* 1974; **8**, 1179-1189.

[132]. Davies H.A., *J. Non-Cryst. Solids* 1975; **17**, 266-272.

[133]. Davies H.A., *Phys. Chem. Glasses* 1976; **17**, 159-173.

[134]. Hng H.H., Li Y., Ng S.C.,Ong C.K., *J. Non-Cryst. Solids* 1996; **208**, 127-138.

[135]. Battezzati L.,Greer A.L., *Acta Metallurgica* 1989; **37**, 1791-1802.

[136]. Li Y., Ng S.C., Ong C.K., Hng H.H.,Jones H., *J. Mater. Sci. Lett.* 1995; **14**, 988-990.

[137]. Chen H.S., *J. Non-Cryst. Solids* 1978; **27**, 257-263.

[138]. Chen H.S., *Appl. Phys. Lett.* 1976; **29**, 12-14.

[139]. Chen H.S.,Turnbull D., *J. Chem. Phys.* 1968; **48**, 2560-2571.

[140]. Bernal J.D., *Nature* 1960; **185**, 68-70.

[141]. Miracle D.B., *Acta Mater.* 2006; **54**, 4317-4336.

[142]. Sheng H.W., Luo W.K., Alamgir F.M., Bai J.M.,Ma E., *Nature* 2006; **439**, 419-425.

[143]. Egami T.,Waseda Y., *J. Non-Cryst. Solids* 1984; **64**, 113-134.

[144]. Miracle D.B., *Nat. Mater.* 2004; **3**, 697-702.

[145]. Somoza J.A., Gallego L.J., Rey C., Fernandez H.M.,Alonso J.A., *Philos. Mag. B-Phys. Condens. Matter Stat. Mech. Electron. Opt. Magn. Prop.* 1992; **65**, 989-1000.

[146]. Kim D., Lee B.J.,Kim N.J., *Thermodynamic approach for predicting the glass forming ability of amorphous alloys*, in *Metastable, Mechanically Alloyed and Nanocrystalline Materials*, A Inoue, Editor. 2005, Trans Tech Publications Ltd: Stafa-Zurich. p. 475-478.

[147]. Concustell A. *et al.*, *J. Mater. Res.* 2004; **19**, 505-512.

[148]. Concustell A. *et al.*, *Intermetallics* 2004; **12**, 1063-1067.

[149]. Inoue A.,Takeuchi A., *Mater. Trans.* 2002; **43**, 1892-1906.

[150]. Glade S.C., Loffler J.F., Bossuyt S., Johnson W.L.,Miller M.K., *J. Appl. Phys.* 2001; **89**, 1573-1579.

[151]. Ge L. *et al.*, *Intermetallics* 2008; **16**, 27-33.

[152]. Choi-Yim H., Xu D.H.,Johnson W.L., *Appl. Phys. Lett.* 2003; **82**, 1030-1032.

[153]. Ma D. *et al.*, *Appl. Phys. Lett.* 2005; **87**, 3.

[154]. Liu C.T.,Lu Z.P., *Intermetallics* 2005; **13**, 415-418.

[155]. Xing D.W. *et al.*, *Trans. Nonferrous Met. Soc. China* 2003; **13**, 68-70.

[156]. Zhang B., Zhao D.Q., Pan M., Wang R.J.,Wang W.H., *Acta Mater.* 2006; **54**, 3025-3032.

[157]. Lu Z.P., Liu C.T.,Porter W.D., *Appl. Phys. Lett.* 2003; **83**, 2581-2583.

[158]. Zhang Y., Chen J., Chen G.L.,Liu X.J., *Appl. Phys. Lett.* 2006; **89**, 3.

[159]. Takeuchi A.,Inoue A., *Mater. Trans. JIM* 2000; **41**, 1372-1378.

[160]. Qin P.G., Wang H., Zhang L.G., Liu H.S.,Jin Z.P., *Mater. Sci. Eng. A-Struct. Mater. Prop. Microstruct. Process.* 2008; **476**, 83-88.

[161]. Klotz U.E., Liu C.L., Uggowitzer P.J.,Loffler J.F., *Intermetallics* 2007; **15**, 1666-1671.

[162]. F.R.deBoer., R.Boom., W.C.M.Mattens., A.R.Miedema.,A.K.Niessen., *Cohesion in Metalis, Transition Metals Alloys* 1988, North-Holland, Amsterdam.

[163]. Eshelby J.D., Frederick S.,David T., *The Continuum Theory of Lattice Defects*, in *Solid State Physics*. 1956, Academic Press. p. 79-144.

[164]. Simozar S.,Alonso J.A., *Phys. Status Solidi A-Appl. Res.* 1984; **81**, 55-61.

[165]. Gallego L.J., Somoza J.A.,Alonso J.A., *J. Phys.-Condes. Matter* 1990; **2**, 6245-6250.

[166]. Murty B.S., Ranganathan S.,Rao M.M., *Mater. Sci. Eng. A-Struct. Mater. Prop. Microstruct. Process.* 1992; **149**, 231-240.

[167]. Vanderkolk G.J., Miedema A.R.,Niessen A.K., *Journal of the Less-Common Metals* 1988; **145**, 1-17.

[168]. Weeber A.W., *Journal of Physics F-Metal Physics* 1987; **17**, 809-813.

[169]. Bakker. H., *Enthalpies in alloys: Miedema's Semi-Empirical Model* 1998, Trans Tech Publications, Netherlands.

[170]. Vincent S., Peshwe D.R., Murty B.S.,Bhatt J., *J. Non-Cryst. Solids* 2011; **357**, 3495-3499.

[171]. Wang Q. *et al., J. Non-Cryst. Solids* 2007; **353**, 3421-3424.

[172]. Buschow K.H.J., *Scripta Metallurgica* 1983; **17**, 1135-1139.

[173]. Buschow K.H.J., *Acta Metallurgica* 1983; **31**, 155-160.

[174]. Takeuchi A.,Inoue A., *Mater. Trans.* 2001; **42**, 1435-1444.